THz On-Chip Waveguides for Ultrafast Magnetic Measurements

Nicolas Aaron Peters

University of Leeds

School of Electronic and Electrical Engineering/School of Physics and Astronomy

Submitted in accordance with the requirements for the degree of

Doctor of Philosophy

November, 2018

Intellectual Property Statement

The candidate confirms that the work submitted is his own, except where work which has formed part of jointly authored publications has been included. The contribution of the candidate and the other authors to this work has been explicitly indicated below. The candidate confirms that appropriate credit has been given within the thesis where reference has been made to the work of others.

N. Peters, M. Rosamond, L. Li, E. H. Linfield, A. G. Davies, M. Ali, B. J. Hickey, and J. Cunningham, "Confinement of picosecond timescale current pulses by tapered coplanar waveguides", Appl. Phys. Lett. 112, 181103 (2018)

Paper discusses some fabrication methods discussed in Chapter 3, and forms the foundation for Chapter 5.

- **Work attributed to author:** Design, fabrication (excluding EBL), testing and analysis.
- **Work attributed to others:** M. Rosamond: EBL processing of devices. L. Li: Growth of LT-GaAs used for photoconductive switches. E. H. Linfield: Support and management for Nicolas Peters, A. G. Davies: Support and management for Nicolas Peters. M. Ali: Assistance with the sputtering of multilayer samples. B. J. Hickey: Support and management for Nicolas Peters. J. Cunningham: Support and management for Nicolas Peters.

N. Peters, M. Rosamond, C. D. Wood, E. H. Linfield, A. G. Davies, L. Li, B. J. Hickey, and J. Cunningham, "Focusing THz radiation in µm-scale waveguides", IRMMW-THz (2017)

Paper discusses initial results presented in Chapter 5.

- **Work attributed to author:** Design, fabrication (excluding EBL), testing and analysis.
- **Work attributed to others:** M. Rosamond: EBL processing of devices. C. D. Wood: Support and management for Nicolas Peters. E. H. Linfield: Support and management for Nicolas Peters, A. G. Davies: Support and management for Nicolas Peters. L. Li: Growth of LT-GaAs used for photoconductive switches. B. J. Hickey: Support and management for Nicolas Peters. J. Cunningham: Support and management for Nicolas Peters.

N. Peters, L. Li, C. D. Wood, E. H. Linfield, A. G. Davies, B. J. Hickey, and J. Cunningham, "GMR at THz frequencies in coplanar waveguides", IRMMW-THz (2017)

Paper discusses initial results presented in Chapter 4.

- **Work attributed to author:** Design, fabrication, testing and analysis.
- **Work attributed to others:** L. Li: Growth of LT-GaAs used for photoconductive switches. C. D. Wood: Support and management for Nicolas Peters. E. H. Linfield: Support and management for Nicolas Peters, A. G. Davies: Support and management for Nicolas Peters. B. J. Hickey: Design concept as well as support and management for Nicolas Peters. J. Cunningham: Support and management for Nicolas Peters.

Acknowledgements

This work would not have been finished without the help and support of many people, both in academic pursuits, and in the retention of sanity. Therefore, I would like to thank the following:

- Firstly, my supervisors, Prof. John Cunningham and Prof. Bryan Hickey for their help and support throughout the PhD work. Their willingness to let me explore and pursue various questions along the way have deepened both my understanding and also my appreciation for the complexities of research in general. It was rather exciting when I finally starting to understand enough about what I was doing to have proper discussions with them, and have greatly enjoyed the process of working through problems.
- Dr. Chris Russell and Dr. Joseph Batley, who patiently trained me at the beginning, and put up with numerous questions. You gave me an excellent start, and were free with advice throughout, which I am grateful for.
- Dr. Matthew Swithenbank for help with on-chip measurements, Dr. Mannan Ali for training with thin film growth, and Dr. Mark Rosamond for performing the Ebeam lithography and for generally being a gold mine of information.
- The electrical engineering group, for providing both a informal forum for discussion when needed, and also much needed breaks from thinking about the thesis.
- Those in Physics who welcomed me on my sporadic visits, and helped me on kit that I hadn't used for years since initial training.
- The cleanroom squad and fellow sufferers. You made the successes better, and reduced the sting of the failures.
- The Leeds and Irish frisbee teams I've played for. There were some mornings where training was the only reason I got out of bed.
- My grandparents and relatives who have kept me in prayer through the highs and lows.

- My parents, who instilled a love of knowledge, and provided academic, emotional, and prayer support.
- My wife, Holly, for her love and steadfast patience through the years of Skype and Ryanair. I can't imagine life without you.
- My heavenly father, who has comforted me and helped me to persevere. "Where does my help come from? My help comes from the Lord, the maker of heaven and earth." "Let perseverance continue its work, so you may be mature and complete".

Abstract

This thesis describes the development of on-chip terahertz (THz) waveguides for use in ultrafast magnetic measurements. An epitaxial transfer method is used to bond photoconductive switch material to quartz substrates. This, combined with optical lithography methods, allows on-chip generation and detection of THz pulses. Normally, the metal in a waveguide has a high conductivity (eg. gold or copper) in order to reduce ohmic loss. However, if this metal is instead a magnetic multilayer, then the THz pulse interaction with the metal can be used to measure ultrafast magnetic effects. This was performed using Cobalt/Copper multilayers, and a THz GMR was seen in a transmitted pulse. Additionally, an 'inverse' GMR was noted in input pulses and in the pulse tail of transmitted pulses. It is believed that this is the first time such behaviour has been documented.

Lateral spin valves offer the ability to separate charge and spin effects; however, the dimensions of these devices is in the hundreds of nanometers range. Coplanar waveguides were used to confine and concentrate THz pulses into this spatial regime. Curved waveguides were fabricated to prove confinement, and magnetoresistance properties were used to demonstrate field concentration.

Devices were then designed to allow picosecond current injection into a lateral spin valve geometry. Initial results are obscured due to interference from the excitation pulse, but improvements to the design and fabrication could pave the way for this technology in the future.

Contents

Abbreviations

MR	Magnetoresistance	GMR	Giant magnetoresistance
THz-TDS	THz time domain spectroscopy	LSV	Lateral spin valve
PC	Photoconductive	FWHM	Full width half maximum
DC	Direct current	CPW	Coplanar waveguide
PGL	Planar Goubau line	DoS	Density of states
FM	Ferromagnetic metal	NM	Non-magnetic metal
MOKE	magneto optical Kerr effect	AMR	Anisotropic magnetoresistance
FM1	First ferromagnetic switch	FM2	Second ferromagnetic switch
HFSS	High frequency structural simulator	DI	Deionised
EBL	Electron beam lithography	E-beam	Electron beam
UHV	Ultra-high vacuum	MBE	Molecular beam epitaxy
SNR	Signal-to-noise ratio	IPA	Isopropyl alcohol
LT-GaAs	Low temperature grown GaAs	HF	Hydrofluoric acid
TEM	Transmission electron microscope	DUT	Device under test
FEM	Finite element method	iGMR	Inverse GMR
iAMR	Inverse AMR	iR	Inverse response
PCB	Printed circuit board	SEM	Scanning electron microscope
CF	Catastrophic failure	LF	Local failure

Chapter 1

Introduction

1. INTRODUCTION

Spin electronics, or spintronics offers to unlock the potential of an electron's spin as well as its charge in devices. This field exploded in 1988 with the discovery of giant magnetoresistance (GMR) [1, 2], a relatively much larger effect than the anisotropic magnetoresistance (AMR) which derives from an electron's spin. This technology was quickly utilized for magnetic read heads in computers, and since then, has gotten smaller and faster, with efforts to understand and harness fundamental magnetic properties for industrial applications. Of particular interest are spin transport properties in non-magnetic metals. For any spintronic application, spin persistence is critical, and an in-depth understanding of spin-relaxation in non-magnetic metals could prove very useful for future advances in ultrafast GMR technology.

One of the simplest geometries that uses spin transport is that of a spin valve, that is, two ferromagnetic layers with a non-magnetic spacer. This is the geometry that first showed GMR, and the magnetoresistance can be strengthened by adding more layers to the structure. Spin relaxation processes in typical spacer metals occur on picosecond timescales with spin diffusion lengths of hundreds of nanometers, and therefore, measurement and fabrication methods should be found to allow these processes to be examined at the relevant length and time scales. Although one of the building blocks of modern spintronics, GMR measurements have only recently been brought into the picosecond regime [3]. Here, THz time-domain spectroscopy (THz-TDS) was used to probe a GMR multilayer as the magnetic field was swept back and forth. A THz GMR was measured, however, the experiment was set up in such a way to deliberately avoid any built-up of spin in the spacer metal (spin accumulation). However, an examination of spin accumulation in the picosecond regime could unlock direct access to spin relaxation processes and is therefore worth investigating.

The measurement of picosecond electrical pulses was made possible with the invention of the 'Auston' photoconductive switch [4]. Using these switches, picosecond electrical pulses, with a power spectrum in the THz regime, could be generated and detected. Using planar waveguides, these electrical pulses could be directed and confined to a region of interest. The objective then, of this work, was to use on-chip THz waveguides in the investigation of picosecond magnetic effects.

Chapter 2

Literature Review

2.1 Chapter Overview

This purpose of this chapter is to supply the reader with a foundation with which to read the rest of this thesis. It is loosely divided into three topics. The first topic (sections 2.2 to 2.4) introduces THz radiation and some of the concepts used in the rest of this work. Next (sections 2.5 to 2.9), the research area of ultrafast magnetic effects is summarised, with a selection of papers highlighted that have built and expanded on this interesting subject. Finally, in the last section, an overview of the research in this thesis is presented.

2.2 Terahertz radiation

Traditionally, terahertz radiation has been said to occupy the region of the electromagnetic spectrum from around 300 GHz to 10 THz [5]. This frequency range lies between that employed by "conventional" (ie. commercial) electronics (up to the 10's GHz range) and conventional optics (which extends down to the infra-red (IR)); it used to be called the "Terahertz gap" due to the difficulty of exciting and detecting frequencies in this range. However, this gap is rapidly disappearing as new technologies and applications emerge.

THz radiation is non-ionising and can penetrate many visually opaque materials, making it a suitable candidate for some forms of imaging [6, 7]. Additionally, the THz frequency range is shared by many low frequency molecular vibrations, meaning that it is also suitable for spectroscopic applications [8]. The picosecond timescale also corresponds to various interaction times in condensed matter, such as the exchange and spin-orbit interactions, meaning that THz radiation can in principle be used to explore fundamental physical effects within their own timescales [9].

2.3 Terahertz Generation and Detection

In this research the method employed for both excitation and detection of THz radiation utilises photoconductive (Auston) electrical switches, which are commonly employed in terahertz time-domain spectroscopy (THz-TDS) [10, 11].

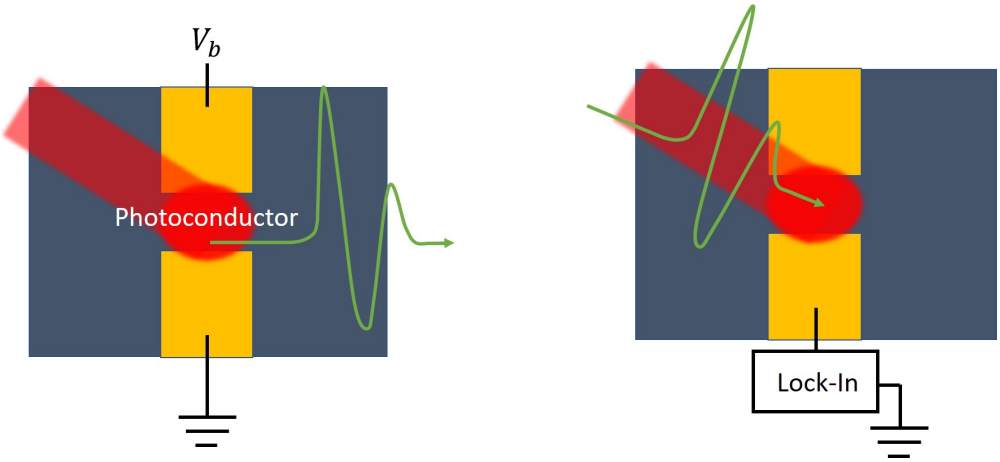

(a) (b)

Figure 2.1: a) If a DC bias is applied to one end of the wire, and the other end grounded, then if a femtosecond optical pulse illuminates the PC material in the gap, a picosecond current pulse is generated, in turn generating a terahertz wave. b) For the detection of a terahertz pulse, an lock-in amplifier is used to measure the current driven by the THz pulse when it arrives at the PC gap at the same time as an optical pulse.

The principle behind both photoconductive excitation and generation is very similar. When photons with sufficiently high energy illuminate a photoconductive (PC) material, electron-hole pairs are generated, and the photoconductor behaves like a conductor. If a wire is fabricated on top of this PC material, with a gap in the middle, a dc voltage on one end, and grounded on the other end, as shown in figure 2.1a, then light with energy in excess of the bandgap can be used to open and close the circuit. Since pulsed lasers can emit pulses with full widths at the half maximum (FWHM) <20 fs in the time domain, this type of electrical circuit could in theory be controlled with 20 fs time resolution. In practical devices, however, the electron-hole pair generation and recombination times of the PC material become the limiting factor, meaning that the electrical current pulses generally remain on the picosecond timescale [12]. Taking the Fourier transform of a pulse that is a picosecond in the time domain gives a frequency spectrum that extends to the terahertz frequency range.

To generate such a THz pulse then requires a PC material with electron-hole generation and recombination times in the hundreds of femtoseconds regime. As shown

in figure 2.1a, a DC bias is applied, and when a femtosecond optical pulse closes the circuit, a current pulse is generated. The rapid carrier generation and subsequent acceleration under the DC bias behaves like an antenna, and a THz pulse is emitted. This can be radiated into free space, or coupled directly into a connected waveguide. To measure the THz pulse, one uses the same principles. Instead of a DC bias, however, there is a lock-in amplifier or equivalent, and it is the THz pulse that provides the bias to drive a current. When the THz pulse is present at the gap at the same time that the gap is illuminated by the optical pulse, then a current will be driven, which will be measured by the lock-in amplifier when it is set to measure at the frequency of an optical chopper in the probe beam path (figure 2.1b). The set up for this type of measurement will be explained further in section 3.5.2.

2.4 Terahertz Waveguides

While the majority of THz-TDS systems use antennas to radiate THz radiation into free space, a portion of these systems instead couple the THz pulse into a waveguide. While sacrificing some of the flexibility that a free-space system provides, on-chip devices have a number of advantages. In the first place, the waveguide eliminates the necessity of aligning the THz radiation path, so providing an invariant beam path. Additionally, the pulse can be well or loosely confined to the waveguide, depending on the choice of waveguide geometry, and extra filters or resonators can be integrated into the circuit. Finally, on-chip devices offer unparalleled control and confinement of the THz radiation in the sub-wavelength regime; a characteristic that is very attractive for electrical testing of objects which are in the micrometer range, or below.

Since THz radiation occupies the gap between electronics and optics, it is possible to use both electrical metallic waveguides[13], and dielectric optical waveguides [14]. However, planar metallic waveguides lend themselves easily to on-chip THz generation and detection, while with dielectric waveguides it is necessary to couple THz radiation from free-space into the waveguide. Therefore, planar metallic waveguides were used throughout this thesis.

When considering planar metallic waveguides to use for on-chip THz waveguid-

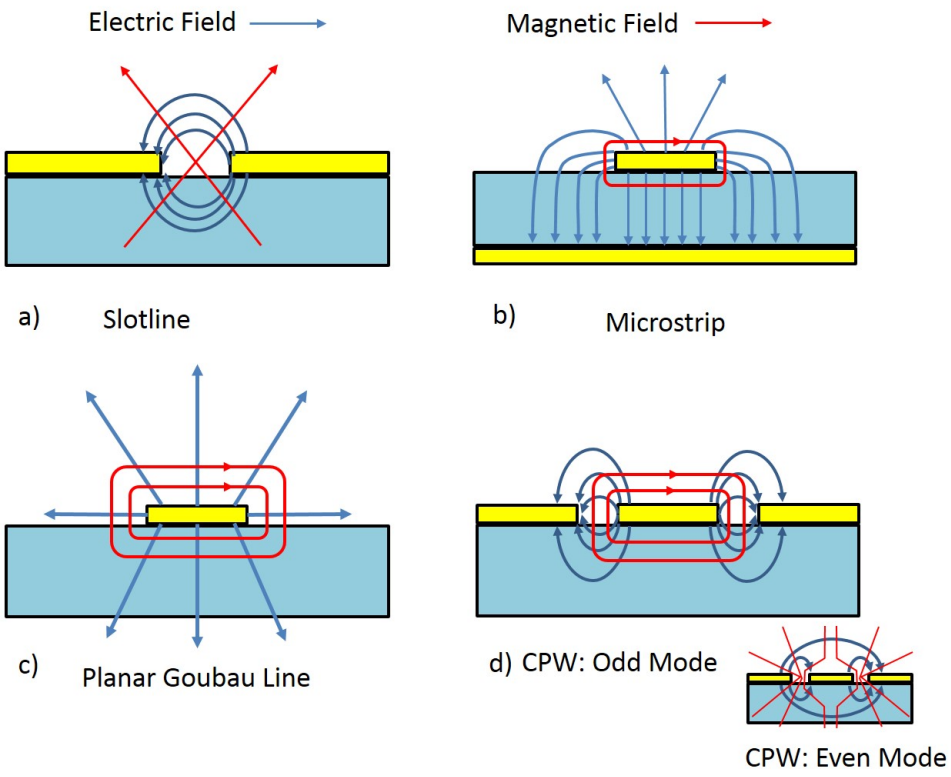

Figure 2.2: Four kinds of planar waveguide for THz transmission: a) Slotline, b) Microstrip, c) planar Goubau line, d) coplanar waveguide in odd mode (inset: even mode). The electric and magnetic field lines are indicated.

ing devices, a number of geometries have been transferred directly with success from microwave circuits. These geometries include the microstrip, slotline, and coplanar waveguide (CPW). It is also possible to use a single wire on a substrate, known as a planar Goubau line (PGL). A range of plasmonic waveguides also exist, where THz radiation is strongly confined to a metal surface through subwavelength metallic features [15].

For the research discussed in this thesis, two features were primarily desired of the on-chip waveguide. In the first instance, it was necessary that the THz radiation should be strongly confined (near the region of the metal) and localised (hundreds of nanometers regime). Secondly, a geometry that lent itself easily to microfabrication techniques was desired. To meet the second criterion, only planar waveguides were considered. As seen in figure 2.2, microstrips, slotlines, and CPWs all provide excellent field confinement, while PGLs have a large evanescent field, and are therefore unsuitable for strong field localisation. Plasmonic waveguides provide good confinement to the metal surface, but the field is not well localised. Of the three microwave designs mentioned, slotlines and CPWs provide the strongest field confinement at the surface of the device, while microstrips confine the field largely within the substrate. It is difficult to make use of the electric field when it is confined within the substrate, so slotlines or CPWs were the two primary options considered. CPWs offer more measurement and design possibilities due to the presence of a centre conductor wire, so this geometry was therefore chosen for the majority of on-chip devices fabricated in this work.

2.5 Electron Transport in Ferromagnets

The basis for much of spintronics derives from the fact that charge transport in ferromagnets is dependent on the spin of the charge carrier. In ferromagnets, charge transport is considered through a two-current model [16], first proposed by Mott. Here, it is assumed that up and down spin electrons are largely independent of each other, and have different conductive properties. This difference is due to an asymmetry in the density of states (DoS) at the Fermi level imposed by the exchange interaction. This is shown in figure 2.3 for Cobalt and Copper. From the Pauli exclusion principle,

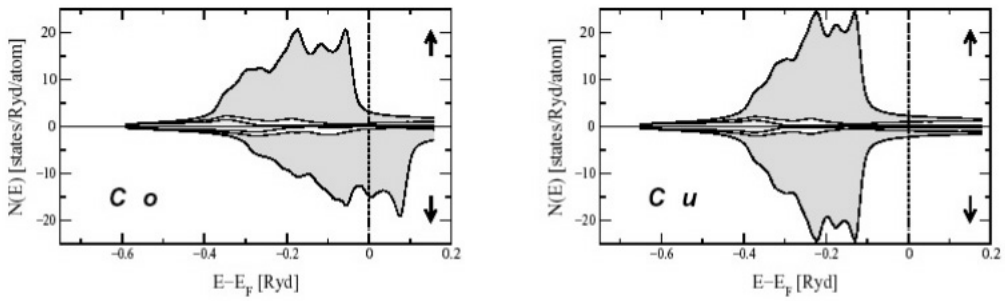

Figure 2.3: The DoS for Co and Cu. The DoS at the Fermi level is asymmetric for Co, giving rise to different carrier properties for spin up or down electrons. (Figure taken from [17])

scattered electrons can only occupy quantum states not already occupied. Scattering is an elastic process, so electrons can only occupy states in the immediate vicinity of the Fermi level.

Therefore, it can be seen that the scattering rate depends on the DoS at the Fermi level. In ferromagnets, the exchange interaction shifts the DoS such that spin up and down carriers have a different DoS at the Fermi level, causing different scattering rates between the carriers. Therefore, when discussing electron transport in ferromagnets, the spin of the carrier relative to the magnetisation is an important parameter, and carriers will have a different conductivity and mobility depending on their spin. As a result of this, when a current is passed through a ferromagnet it is then said to be spin polarised, since the current is carried primarily by either spin up or spin down electrons, depending on which orientation has the higher conductivity. This also means that when a current is passed from a ferromagnet (FM), which has a spin polarised current, to a non-magnetic metal (NM), then an excess of one type of spin builds up at the FM/NM interface. This is called spin accumulation.

2.6 Ultrafast Demagnetisation

The field of ultrafast magnetism began with the work by Beaurepaire et al. [18] when they discovered a sub-picosecond scale change in the magnetisation of a ferromagnetic nickel sample after intense optical excitation. This was the first time that a sub-

picosecond magnetic response had been measured, and it opened up the new field of ultrafast magnetism. In this early work, no mechanism was proposed, but rather a three temperature model was used to describe the results, in which energy was transferred between electrons, spins, and the lattice according to the relevant time constants. This was expressed through

$$\begin{aligned} C_e(T_e)\frac{\mathrm{d}T_e}{\mathrm{d}t} &= -G_{el}(T_e - T_l) - G_{es}(T_e - T_s) + P(t) \\ C_s(T_s)\frac{\mathrm{d}T_s}{\mathrm{d}t} &= -G_{es}(T_s - T_e) - G_{sl}(T_s - T_l) \\ C_l(T_l)\frac{\mathrm{d}T_l}{\mathrm{d}t} &= -Gel(T_l - T_e) - G_{sl}(T_l - T_s) \end{aligned} \tag{2.1}$$

where $P(t)$ represents the heat injected by the laser pulse, $C_{e,s,l}$ is the heat capacity for the electron, spin, and lattice systems, $T_{e,s,l}$ is the temperature of the electron, spin and lattice systems, and G_{xy} is a coupling parameter between systems. The phenomenological model described the experimental results well, but did not comment on the mechanism for the coupling between systems. Subsequent work confirmed and built on the original experiment, proposing various mechanisms that could explain these ultrafast magnetisation dynamics.

Carpene et al. [19] measured ultrafast demagnetisation in thin films of iron, and suggested an electron-magnon coupling mechanism. The optical laser pulse excited hot electrons which transfer energy to magnons, leading to the observed rapid demagnetisation. This energy was then transferred from spin angular momentum to orbital angular momentum, which was absorbed by the lattice. The observed magnetisation recovery took place with a time constant of 800 fs, supporting Elliot-Yafet's picture of spin-flip scattering. Krauss et al. [20] proposed a system where the demagnetisation occurred as a result of interband scattering between the optically excited electrons leading to a redistribution of electrons from majority to minority bands.

Battiato et al. [21] were the first to propose a demagnetisation route controlled entirely by the movement of charge carriers. They suggested that the laser excited electrons into higher energy sp bands, which have much higher velocities than the d bands. Scattering is a spin dependent process, meaning that one spin type can move away from the point of optical excitation easier, causing the observed change in

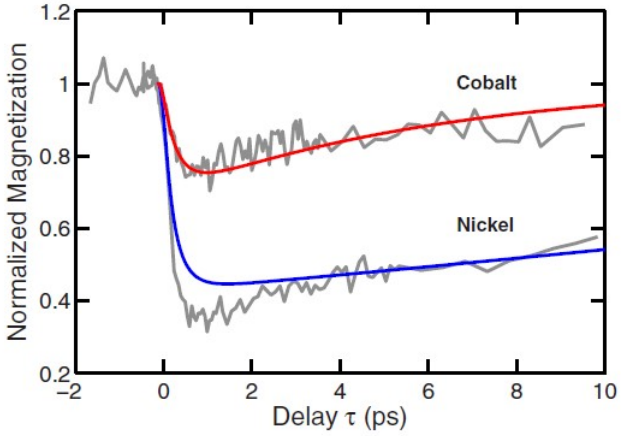

Figure 2.4: Ultrafast demagnetisation of thin films of Co and Ni after intense optical excitation ($4\,\mathrm{mJ\,cm^{-2}}$). The demagnetisation occurs in about 200 fs, and the remagnetisation occurs over tens of picoseconds.

magnetisation. This is more obvious when there are thin layers of magnetic material next to a non-magnetic material. Here, carriers that experience low scattering rates are transported out of the thin magnetic layer into the non-magnetic layer while carriers that experience high scattering are trapped in the magnetic layer, thus changing the balance of spin up and spin down carriers in the magnetic film, and demagnetising the sample at the point of excitation. This theory is supported by Eschelohr et al. [22] who showed that the laser pulse does not have to be directly impingent on the magnetic material in order to demagnetise it [8]. In their experiment, hot electrons were excited in a gold layer outside the magnetic layer, and they showed that the demagnetisation in this case was effectively the same as when the carriers were excited directly within the magnetic material. They argue that carriers of both spins are excited in the gold and are transported into the ferromagnet. Minority carriers are trapped in the ferromagnet, and majority carriers pass through the ferromagnetic layer resulting in demagnetisation. This experiment excited some controversy, since it was believed that the gold capping layer was not thick enough to entirely block the exciting optical pulse. However, it was repeated under more rigorous conditions [23], with essentially the same results. This mechanism is especially interesting, since the movement of carriers could in theory be accomplished with lower energy THz pulses as well as the higher energy optical pulses

used in the experiment.

More recently a study has been published that distinguished between transport and spin-flip processes in a Co/Cu multilayer sample [24]. They determined that transport effects are dominant in the first 100 fs, but that afterwards, spin-flip scattering were primarily responsible for the demagnetisation.

2.7 Magnetism and Terahertz Radiation

Some years after ultrafast demagnetisation was first reported, the mechanism by which it occurred was still an ongoing question. Moreover, there were some doubts about the detection methods used. In the majority of ultrafast experiments, an intense optical pulse has been used to excite the magnetic film, while a weaker optical pulse was used to detect subsequent changes in magnetisation through the magneto optical Kerr effect (MOKE). The MOKE mechanism describes how the polarisation of light reflected off the surface of a magnetic metal changes with magnetisation. By observing changes in reflected light polarisation then, it is possible to measure changes in magnetisation. However, in some experiments, it was thought that charge dynamics affected the reflected optical signal in the picosecond regime [25, 26], casting doubt on whether the ultrafast magnetisation dynamics were actually being measured.

As an alternative method of measuring magnetisation dynamics, it was shown that a picosecond demagnetisation should result in an emitted electromagnetic field [27]. This is derived using Maxwell's equations, arriving at the relation $E \propto \frac{\partial^2 M}{\partial t^2}$. It was shown that the THz radiation emitted from a thin Ni film corresponded well to what would be expected from the demagnetisation observed with MOKE methods (figure 2.5a). Later work [28] verified this with films of Co and GdFeCo. However, for a layer of NdFeCo, it was found that the THz radiation predicted faster dynamics that the MOKE method. This was attributed to the MOKE measurements being more sensitive to some elements than others [28]; the wider implication was that a THz pulse can uncover dynamics masked to MOKE measurements.

It was later shown that for bilayer samples the emitted THz pulse was not totally dependent on the demagnetisation. Rather, as described in section 2.6, an intense

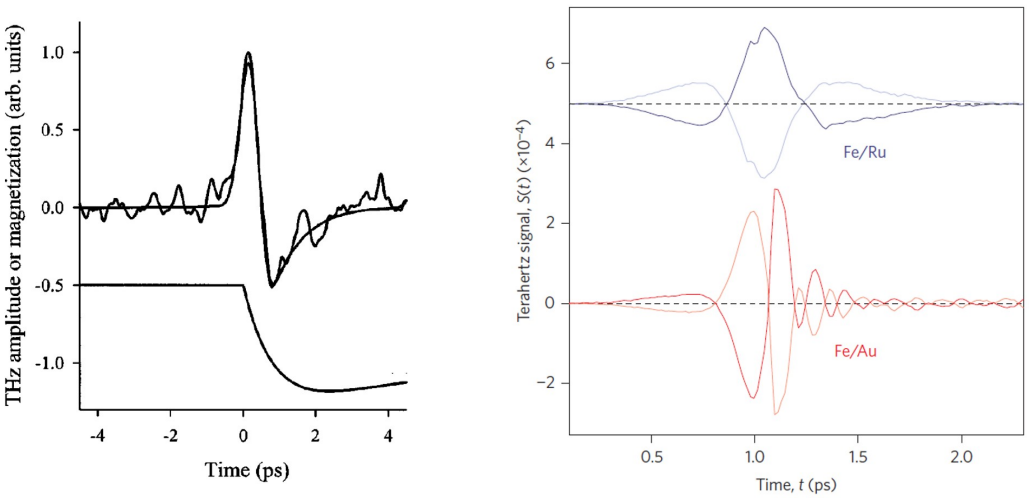

(a) (b)

Figure 2.5: a) After intense optical excitation, both a THz response (top), and MOKE response (bottom) was measured. A model based on the MOKE demagnetisation response matched the THz pulse well (smooth fit on top). b) The generated THz pulse was determined by the electron mobility in the non-magnetic capping layer, with a Au layer possessing much faster dynamics that Ru, and therefore producing a narrower THz pulse in the time domain. The signal inverts with the magnetisation is reversed. [figures taken from [27] and [29] respectively]

optical excitation could generate a spin polarised current away from the excitation area. This spin polarised current could pass into the capping layer, in turn generating a perpendicular charge current through the inverse spin Hall effect, which acts somewhat as an antenna, and contributes to the emitted THz pulse. Since electron motion in the capping layer is a contributing factor, it makes sense that the electron properties in the capping layer should affect the emitted pulse. This was shown in [29], where they capped a Fe film with an Au layer and a Ru layer, which have very different electron mobilities, with Au electrons being much faster than Ru electrons. The THz pulses measured from these samples are shown in figure 2.5b, where it is clear that the pulse from the Ru sample shows much slower dynamics than the Au sample. This experiment had the effect of strengthening the carrier motion theory of demagnetisation, while also limiting the usefulness of the THz pulse for magnetisation measurements. It also opened up a new area of research, where metal multilayers are tuned to emit broadband THz radiation when optically excited [30]. This technology is inconvenient for some applications because it requires high intensity optical powers. However it might be very useful for other applications, since it eliminates the need for applied voltages, and requires no physical contact with wires.

THz radiation has also been used to excite and control magnetic systems. This is advantageous for some experiments since THz radiation is inherently low-energy (approximately 4 meV at one Terahertz), and it therefore does not excite electrons to higher states. Rather, it is a method of applying ultra-short electric or magnetic fields to a system without significantly perturbing the carrier dynamics. This feature was used to good advantage in [20], where the magnetic field in a THz pulse was used to switch magnon (quantized spin excitation) resonance on and off in a layer of antiferromagnetic NiO in the picosecond timescale. In [31], the magnetisation of a Co film is found to follow the pulse shape of the exciting THz magnetic field, demonstrating non-resonant magnetisation control.

THz radiation has also been used to demagnetise a CoPt film in an on-chip configuration [32]. Here, similar to the work in this thesis, a THz pulse was excited using a photoconductive switch, and guided to the magnetic sample through a CPW. MOKE methods were used to measure the change in magnetisation. This work also repeated

the same measurement, but used optical excitation instead of THz excitation. They show that the demagnetisation is different when different excitation methods are used, and attributed the difference to non-thermal effects during optical excitation.

While the above methods either only measure the THz pulse, or only use a THz pulse to excite the magnetic system, there is only a very limited amount of work that has used THz-TDS for magnetic measurements. In this case, a THz pulse is used to excite the magnetic sample, and then that same THz pulse is measured. Any change in the measured pulse can then provide spectroscopic information. THz-TDS has been used to measure anisotropic magnetoresistance in a dense Co particle ensemble [33], and a similar experiment was performed to show the attenuation effects caused by spin accumulation [34]. Later, THz-TDS was also used to characterize a metallic multilayer sample that showed giant magnetoresistance [3].

2.8 Magnetoresistance

Magnetoresistance refers to the phenomenon whereby the resistance of a metal changes when an external magnetic field is applied. All metals exhibit such properties for extremely high fields, however, for this work, the focus will be on two types of magnetoresistance found in ferromagnetic metals or multilayers.

Anisotropic magnetoresistance (AMR) was first reported by Lord Kelvin [35] in 1856, and depends on the orientation of the magnetisation relative to the current [36]. In general, this shows itself as a reduction in resistance when the magnetisation is perpendicular to the current, and an increase in resistance when the magnetisation is parallel to the current. This was explained by Smit [37], who showed that s-d scattering was dependent on the angle (θ) between an electron's momentum and the magnetisation. A more complete phenomenological description can be provided through

$$\rho_{\parallel} = \rho_{\perp} + \Delta\rho cos^2(\theta) \tag{2.2}$$

where ρ is the resistivity when the current is parallel or perpendicular to the magnetisation, and $\Delta\rho$ is generally less than 5%.

The giant magnetoresistance (GMR) was so called in order to distinguish it from AMR. In order to produce a GMR, the most common configuration consists of three

metallic layers, with two ferromagnetic layers, and one non-magnetic spacer layer. This is illustrated in figure 2.6a. When considering a current passing through the trilayer, it is important to recall from section 2.5 that the scattering rate for electrons passing through the ferromagnetic layer depends on the orientation of the electron's spin relative to the magnetisation of that layer. As grown, the metallic trilayer is designed so that the magnetisation of the two ferromagnetic layers is antiparallel. Therefore, in this configuration, both up and down spin electrons experience one layer with low scattering and one layer with high scattering. This can be represented by considering resistors in parallel, as shown in figure 2.6a. When an external magnetic field is applied in plane, then the magnetisation of both magnetic layers can be forced to be parallel. In this configuration, the up spin electrons experience low scattering through both magnetic layers, while the down spin electrons experience high scattering in both layers. This can also be expressed in circuit diagram form, in which it is clear that this configuration has a smaller resistance. In figure 2.6b, the resistance of a GMR multilayer is measured as the magnetic field is swept back and forth. When the field is low, the multilayer is in its natural antiparallel state, and the resistance is high. As the external magnetic field increases in magnitude, the magnetisation of the FM layers is forced align, and the resistance decreases.

To observe GMR, it is required that electrons coming from one FM layer preserve their spin state during subsequent interactions in other FM layers. To meet this condition, the spacer NM layer must be thin enough that the spin has not flipped while passing through. For a current perpendicular to the plane (as in figure 2.6a), this condition is met if the thickness of the spacer is on the order of the spin diffusion length. If the current is parallel to the plane, this condition is met if the spacer thickness in on the order of the electron mean free path. Since spin preservation is necessary for this effect, and since spin relaxation times in paramagnets (eg. Cu) is on the order of picoseconds, it is of great interest to observe how GMR behaves on a picosecond timescale. The one paper that has investigated this [3], ensured that spin accumulation would not occur. However, a study of spin accumulation in the ultrafast timescale would also be highly interesting.

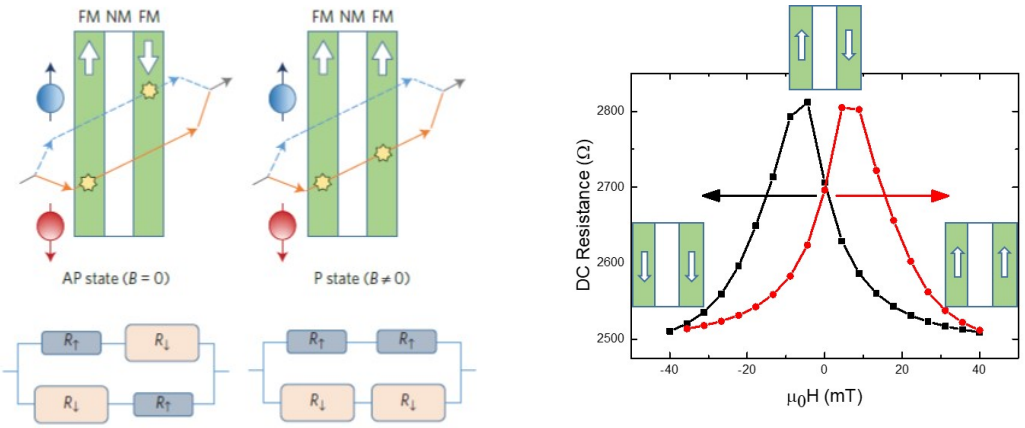

(a) (b)

Figure 2.6: a) A schematic illustrating the principle of GMR. When magnetisation of the ferromagnetic layers is antiparallel (left), there is no scattering free path for electrons to use (top), and therefore no low resistance channel (bottom). When an external magnetic field is applied and the magnetisation is forced to be parallel, then spin up electrons experience less scattering through the sample (top), and there is a low resistance channel (bottom). [figure taken from [3]] b) As a result, when the resistance of sample with GMR is measured as the magnetic field is swept back and forth, the resistance is a maximum close to zero field, and decreases as the field forces the ferromagnetic layers to align. Arrows indicate the sweep direction.

2.9 Lateral Spin Valves

While accessing the spin degree of freedom is of great interest, it is not always straightforward to isolate spin effects from charge effects. Lateral spin valves (LSVs) offered an effective solution to this problem. A LSV is essentially similar to the magnetic trilayer shown in figure 2.6a, however, it is spread out laterally as shown in figure 2.7a. It is composed of two ferromagnetic switches and a NM spacer wire. One of the FM switches is used for injection (FM1) and the other used for detection (FM2). A charge current is passed through FM1 into the NM wire. Since the current in FM1 is spin polarised, spin will accumulate at the FM1/NM interface and diffuse in both directions along the NM wire. On the right hand side, no charge current flows, but there is a spin current due to the diffusion of the accumulated spins.

The detection of the spin current is accomplished through FM2. For simplicity, consider the case shown in figure 2.7b. Here, we look at the interaction between NM and FM2. A spin current has been injected into NM and there are more spin up carriers at the NM/FM2 interface than spin down carriers. In this simplified case, we will assume that FM2 is entirely spin polarised. When FM2 has the same magnetisation as FM1 (parallel case), the fermi levels of the spin up carriers in NM and FM2 will align and a voltage can be measured in this configuration. When FM2 has the opposite magnetisation as FM1 (antiparallel case), then the spin down carriers will align, and a different voltage will be measured. The difference between these voltages indicates the magnitude of the spin current.

In order to induce the parallel and antiparallel cases in FM1 and FM2, these magnetic switches can be fabricated with different geometries. For example, in the work presented in this thesis, FM1 was relatively long and narrow so that its shape anisotropy would resist magnetisation changes. FM2 was made to be comparatively thicker, and also contained a nucleation pad where the magnetisation could change relatively easily. Therefore, when an external magnetic field was swept from positive to negative, FM2 would change magnetisation before FM1, giving an antiparallel state. As the external field continues to decrease, eventually FM1 would also switch, returning the system to the original parallel state. The measured voltage would be similar to that

shown in figure 2.7c. If the field was then swept from negative to positive, the mirror image would be measured.

LSVs are typically made in batches, with the separation between the FM switches systematically varied. The magnitude of the spin signal can then be measured for different switch separations, allowing direct measurement of the spin diffusion length, λ_s. Since $\lambda_s = \sqrt{D\tau_s}$ [38], this gives information about spin diffusion (D) and spin relaxation (τ_s). The spin relaxation time in particular is of interest, since spin preservation is necessary for any spintronics application. By isolating spin effects in the LSV structure it is possible to systematically adjust the interface and intermediate wire properties to understand the spin relaxation mechanism. Examples of experiments previously reported include variation of metal thickness [39] to determine the role of surface oxide in the spin relaxation time, comparison of ohmic and tunnel junction contacts to optimize spin current injection [38], variation of metal purity [40] to isolate contributions to the spin relaxation rate from impurities, phonons, and the kondo effect, and multiple ohmic contacts [41] to identify their role as a spin relaxation avenue. While much can be accomplished with DC measurements, it would be extremely interesting to conduct spin current measurements at the same timescale as the spin relaxation, which has not yet been accomplished for LSV geometries.

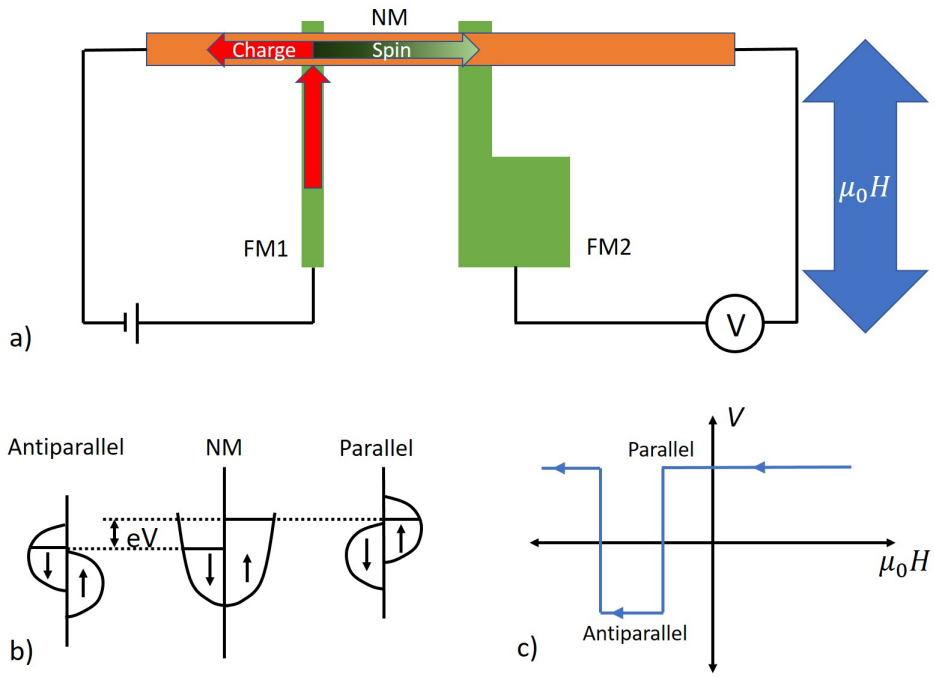

Figure 2.7: a) A schematic of a LSV device measurement setup. The left side of the device contains a closed circuit where the current flows from the first ferromagnetic switch (FM1) into the nonmagnetic metal (NM). No charge current flows on the right hand side of the device, but a spin current does flow, due to the spin accumulation at the FM1/NM interface. b) This can be detected by measuring the voltage between the second ferromagnetic switch (FM2) and NM. This voltage depends on the magnetisation of FM2 relative to FM1. c) FM1 and FM2 are designed to switch magnetisation at different field strengths, and as an external magnetic field is swept back and forth, the orientation of the two magnets will switch between parallel and antiparallel, with a corresponding change in the voltage measured.

2.10 The thesis in context

The long-term overarching goal of the research contained in this thesis, and extending beyond it, is to investigate spintronic effects on a picosecond timescale. The tool used for this purpose in my work was picosecond electrical pulses coupled into coplanar waveguides.

Chapter 3 describes the fabrication and measurement methods used throughout this thesis. In particular, the epitaxial transfer method that allows PC switch material to be transferred to a quartz substrate is described. Other cleanroom methods and equipment are also described, as well as THz on-chip measurement techniques and DC LSV measurements.

In Chapter 4, on-chip THz devices were fabricated out of both single layers of magnetic metal, and out of multilayers exhibiting giant magnetoresistance. Transmitted pulses successfully demonstrated the viability of picosecond electrical pulses to probe spin effects. However, confusion regarding the separation between charge and spin effects suggested that LSVs could provide additional information. Chapter 5 discusses how tapered waveguides were fabricated, modelled, and tested. Successful transmission and confinement were demonstrated in waveguides in the micrometer range, confirming their suitability for lateral spin valve excitation. Models made in HFSS (high frequency structural simulator) support the experimental results.

Finally, having demonstrated successful measurement of magnetic spin effects in GMR waveguides, and confirmed THz pulse transmission in extremely confined regions, Chapter 6 describes how THz lateral spin valves were designed and fabricated in an attempt to measure spin currents on the picosecond timescale. While this last portion of the work did not advance far enough to measure a picosecond spin current, the measurements obtained allow us to suggest improvements, so paving the way for future work in this area.

Chapter 3

Fabrication and experimental methods

3.1 Chapter Overview

All of the on-chip terahertz (THz) devices discussed in this thesis were fabricated in a class 100 cleanroom and used low temperature grown Gallium Arsenide (LT-GaAs) as their photoconductive switch material. This chapter discusses the tools and methods used in device fabrication as well as the growth, annealing, and epitaxial transfer of the LT-GaAs. Where relevant, optimisation of processing recipes is presented. Experimental techniques for the measurement of on-chip THz devices and DC lateral spin valves are then presented.

3.2 Optical and Electron Beam Lithography

3.2.1 General Principle of Lithography

Lithography is a powerful tool for the definition of micro or nanoscale features, and is widely used in both industry and academia. The principle depends on polymers called resists which are chemically altered on exposure to light or high energy electrons. The resist is generally kept in fluid form and a dropper is first used to cover the substrate with the resist. The sample is then spun at a user determined spin rate. This spin rate, as well as the viscosity of the resist, determines its final thickness on the substrate surface. The sample is then baked to remove the solvent, leaving a uniform layer of polymer.

The polymer layer is then selectively exposed, either with ultra-violet light through a mask for optical lithography, or by a high energy beam of electrons for electron beam lithography (EBL). Exposure to this radiation changes the chemical composition of the polymer, either increasing (positive resist) or decreasing (negative resist) its solubility to selected solvents (referred to as developers). By immersing the sample in such a solvent, the sections of the polymer that were exposed to radiation either wash off while the rest remains (for positive resists), or they remain while the rest of the resist washes off (for negative resists). Metal can then be deposited on the sample surface, only reaching the substrate where the resist pattern allows, as shown in figure 3.1. The remaining resist is then removed, along with the metal deposited on top of it, leaving

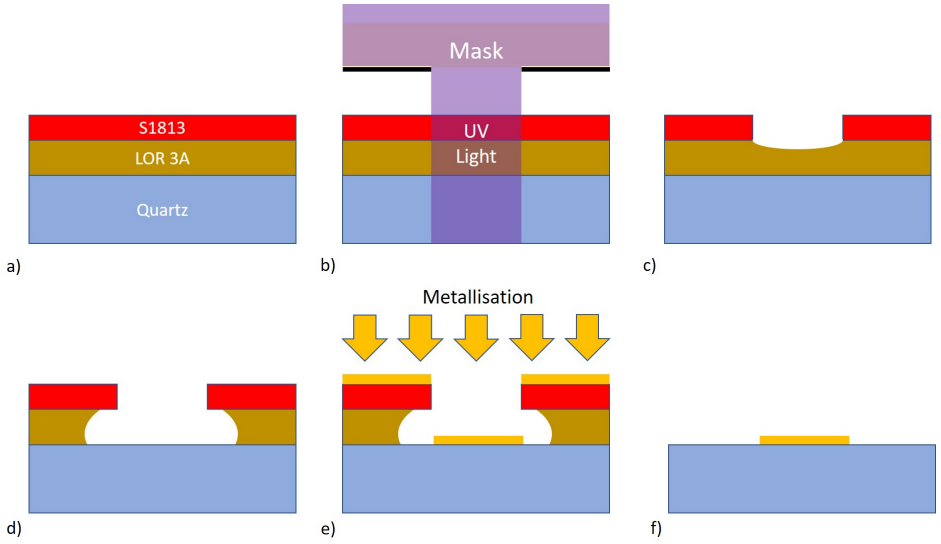

Figure 3.1: The concept of lithography is illustrated. a) In this case a LOR/S1813 bilayer is used. In b) the resist bilayer is exposed with UV light through a mask. It is developed in MF-319, c) washing away the exposed layer of S1813 and starting to dissolve the LOR underneath. The device is then baked at 200 °C, strengthening the S1813 layer. d) Further development in MF-319 completely removes the LOR down to the substrate and undercuts the S1813 layer. e) Metal is then deposited on the surface, and f) the resist is removed, leaving only the metal that was deposited onto the substrate.

only the metal that was deposited directly on the substrate surface.

Lithography in general is limited in resolution to about half the wavelength of the radiation used. For ultraviolet radiation (around 400 nm in this study) this corresponds to about 200 nm. However, in practical terms this limit is rarely achievable, and for features below one micrometre EBL was used in this work. Here the same limit applies, but the wavelength of the high energy electrons is much less than that of UV light. In general the wavelength of a particle can be expressed as $\lambda = \frac{h}{p}$ where h is the Planck constant and p is the particle's momentum. For electrons accelerated by voltages of hundreds of kilovolts, this gives a wavelength in the picometer range, far below the resolution limit of optical light. However, the resolution limit of E-beam lithography systems is typically in the nanometre range. This is due to an effective widening of the electron beam caused by scattering in the resist, and backscatter from the substrate.

3.2.2 Resist Combinations

The majority of devices fabricated in this work used optical lithography to define features. The resist coating used throughout was a LOR 3A/S1813 bilayer (manufactured by Microchem and Rohm and Haas respectively), with an HMDS (Hexamethyldisilazane) primer coating. This was chosen both for its good adhesion to the quartz substrates used and for the undercut this method provides. An undercut is necessary to break metal continuity over the resist edge, ensuring a clean lift-off after metallisation as illustrated in figure 3.1c. This resist bilayer provides the undercut necessary not only for thermal and E-beam evaporation, but also for sputtering methods, which are far less directional. This will be discussed further in subsequent sections.

This undercut is achieved largely because LOR 3A is not a photoresist. It is a polymer spacer layer that rapidly dissolves in MF-319, the developer for S1813. The S1813 layer, which is on the surface, is exposed by ultraviolet light through a mask. It is then developed in MF-319 (manufactured by Rohm and Haas), and the exposed sections of S1813 are washed away, exposing the LOR 3A layer. The S1813 is then baked at 180 °C for one minute, cross-linking the polymeric chains and toughening the S1813. The device can then be further developed, and the hardened S1813 now acts as a mask for the LOR 3A layer underneath, which rapidly dissolves where exposed and undercuts the top S1813 layer. This process in shown in figure 3.1.

The recipe used for the LOR 3A/S1813 bilayer would provide resist thicknesses of 400 nm/1.3 µm respectively, and is as follows.

- Clean substrate in acetone, IPA, and deionised water. If the sample is robust enough, also clean for 5 min with the plasma asher.
- Bake the substrate for 10 min at 200 °C to remove any water from the surface. This is unnecessary if the sample has been in the plasma asher.
- Spin on HDMS primer at 5000 rpm for 30 s.
- Bake for 1 min, rinse with IPA, and bake again for 1 min.
- Spin on LOR 3A at 2000 rpm for 30 s.

- Bake for 3 min at 200 °C.
- Spin on S1813 at 4000 rpm for 30 s.
- Bake for 4 min at 115 °C
- Expose under UV light.
- Rinse in MF-319 for approximately 1 min.
- Visually inspect to ensure complete S1813 removal. If clear, hard bake at 200 °C.
- Rinse in MF-319 for approximately 30 s to provide an undercut.

The two e-beam resists used were MMA and PMMA (both manufactured by Microchem). PMMA is less sensitive than MMA and therefore offers better resolution. The two were mostly used in conjunction as a MMA/PMMA bilayer. The MMA is more sensitive, and is therefore easier to expose than the PMMA layer. This is discussed in detail in [42], where the dose required to clear PMMA 950k A5 and MMA(8.5)MMA EL11 is systematically studied. This is shown in figure 3.2, where the contrast curves for these two resists are compared. It is clear that there is a small range above 100 $\mu C\,cm^{-2}$ where the MMA layer is fully cleared but the PMMA layer is largely unaffected.

As a result, the dose needed to expose the top PMMA layer exposes a larger area of MMA underneath, providing a good undercut. This resist combination also allows more complicated structures, using a technique called shadow evaporation. Because MMA is exposed at a lower dose than the top PMMA layer, it is possible to expose the MMA layer underneath the PMMA layer without fully exposing the top PMMA layer. This allows tunnels and caves to be developed in the resist bilayer. When combined with highly directional metallisation sources and ultra-high vacuum conditions, it thus is possible to fabricate complicated devices with two metals deposited without ever breaking vacuum, ensuring clean interfaces. This is illustrated in figure 3.3.

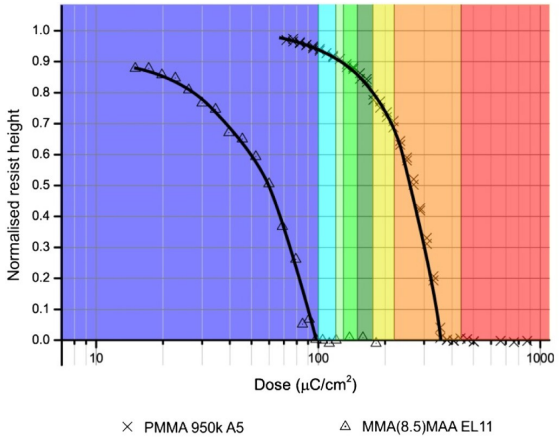

(a)

< 100 μC/cm²	MMA(8.5)MAA not cleared
100 - 120 μC/cm²	MMA(8.5)MAA just starting to clear
120 - 130 μC/cm²	MMA(8.5)MAA lower dose
130 - 150 μC/cm²	MMA(8.5)MAA clear
150 - 176 μC/cm²	MMA(8.5)MAA upper dose
176 - 200 μC/cm²	PMMA thinning
220 - 440 μC/cm²	PMMA significantly thinned
> 440 μC/cm²	PMMA cleared

(b)

Figure 3.2: a) Contrast curves for resist height after development vs electron beam energy for MMA and PMMA. b) Table showing resist characteristics against a range of doses. (figure taken from [42])

Figure 3.3: a) A device with an MMA/PMMA bilayer is exposed with two different doses of electron beam. The low dose only exposes the MMA layer, while the high dose exposes both layers. This produces an undercut area under a PMMA 'roof'. b) Metal can be evaporated both at an angle, depositing inside the tunnel area, and also c) normal to the sample surface, so that the 'roof' blocks the deposition.

3.3 Metallisation

3.3.1 Necessity of a good vacuum

In all the metallisation techniques discussed here, it was necessary to operate in an evacuated chamber. For devices made in this project, the pressure ranged from 2×10^{-6} mbar to ultra-high vacuum (UHV) pressures of 1×10^{-9} mbar. A good vacuum is necessary for multiple reasons. In the first place metal atoms risk chemically reacting with any gas molecules in the chamber, meaning that the metal deposited on the surface of the device may not be the one intended. Collisions with gas molecules can also change the direction that the metal is travelling. This is problematic since, for lithographic methods, it is generally important to ensure good directionality between the source and the sample to ensure clean lift-off, requiring a mean-free path larger than the critical dimensions of the evaporator (metal source to target device). At 10^{-6} Torr, the expected mean free path would be around 80 m. For devices where metal or interface purity is important, it is especially critical to secure a good vacuum, as gas atoms in the chamber will slowly adhere to the surface of the sample, thus potentially introducing defects and/or contamination to the metal layer. Finally, for thermal evaporation techniques, a good vacuum protects the filament from reacting with oxygen and nitrogen in the air, which would eventually destroy it.

3.3.2 E-beam and Thermal Evaporation

Both E-beam and thermal evaporation operate on similar principles. The metal of interest is heated past its boiling point so that it begins to evaporate. The samples to be metallised are placed face down over the heated source, and a portion of the evaporating metal condenses on the sample surface. For both methods, the chamber is kept under high vacuum, and the evaporated metal is thus highly directional (ie. an emitted atom has a large mean free path).

For thermal evaporation a filament, typically tungsten, is used to heat the deposition metal. The filament can either be wrapped around a ceramic container, or the filament itself can have a bowl shaped depression to hold the metal of interest. The disadvantage with this method is that the entire volume of metal needs to be heated to boiling point

before evaporation. Additionally, the container itself need to be heated to a high temperature, potentially outgassing in the process and reducing the integrity of the vacuum in the chamber.

E-beam evaporation uses high energy electrons to heat the surface of a metal source to boiling point. Electrons are generated from thermionic emission from a filament, before being accelerated by a high voltage source towards the metal target. A magnetic yoke is frequently used to direct the beam more precisely. The advantage of this method is that only the surface of the metal needs to be heated, so less heat radiation is emitted.

3.3.3 Sputtering

Sputtering deposits metal by bombarding a target with argon ions. The ions free atoms from the target surface, additionally imparting kinetic energy to them so they can travel to the sample of interest. This can be done at relatively low temperatures (50 °C), and is a good technique for depositing metals with high boiling points (eg iridium at around 4100 °C). Sputtering is commonly used for the deposition of metal multilayers, since it is possible to have multiple targets sputtering at the same time, each in a localised area, and with stable deposition rates. By mounting a sample on a wheel that is free to rotate over different targets, layered structures can easily be grown.

Sputtering is a technique frequently used to grow very thin layers down to the angstrom range. As a result, it is critical to maintain UHV conditions during growth, as any water or chemically reactive molecules in the air will degrade interface quality and react with deposited metals. However, during growth itself, an argon gas flow is introduced into the chamber. This is necessary since it is ionised argon ion bombardment that dislodges metal from the target surface. Since argon is inert, it does not degrade the purity of the deposition or interfaces. However, the argon gas does greatly reduce the mean free path of the sputtered atoms. This means that it is difficult to combine lithographic methods with sputtering, and to do so requires a good degree of undercut in the resist layer. A method frequently chosen to bypass this issue is to metallise a planar sample without features as the first step, and then to use lithographic methods to define an etch mask. Wet or dry etching can then remove any undesirable material. However, due to the necessity of integrating photoconductive LT-GaAs switches

into our fabricated devices, this etch method could not be used over the course of this research.

3.4 LT-GaAs

3.4.1 Molecular Beam Epitaxy

Molecular beam epitaxy (MBE) is a method used to grow epitaxial (thin) films of either metal or semiconductor material. It is notable because samples grown using this method can achieve atomic level precision in layer thickness. To do this, samples are grown on ultra-clean substrates under UHV conditions. The desired deposition materials are heated in chambers called effusion cells to evaporation temperatures, and beams of the emitted atoms are directed at the substrate. The rate of emission is generally low ($\text{Å}\,\text{s}^{-1}$), so that the time it takes to close the shutter on the effusion cell is less than the time it takes to grow an atomic layer on the substrate. The substrate is generally heated to a temperature sufficient to allow atoms to migrate to lattice positions (for GaAs around 500 °C). In this way perfect crystals can be grown with atomic layer accuracy. An MBE machine was used to grow the photoconductive switch material used throughout this project. Though the author did not perform MBE growth, he was involved in the subsequent characterization of the photoconductive material, as discussed later.

3.4.2 LT-GaAs Growth

The photoconductive switch material used throughout this project was low temperature grown Gallium Arsenide (LT-GaAs). Wafers were grown in-house using MBE methods. An 100 nm AlAs sacrificial layer was first grown on an semi-insulating GaAs substrate, and LT-GaAs was then grown on top at 205 °C in an arsenic-rich atmosphere. This low temperature allows excess arsenic atoms to be introduced into the GaAs lattice. These atoms can be considered to be point defects, which act as trapping regions for electron-hole pair recombination, so decreasing the carrier lifetime [12]. As grown, LT-GaAs wafers exhibit carrier lifetimes as short as 90 fs, but the concomitant dark resistivity is then low, which decreases the signal-to-noise ratio (SNR) in the PC switches.

In order to increase the dark resistivity, the LT-GaAs was annealed ex-situ between 500 °C and 600 °C for 10 min in a nitrogen atmosphere. The annealing process allows the excess arsenic to precipitate, forming buried Schottky barriers and increasing the resistivity. However, this reduces the number of point defects and increases the carrier lifetime. In figure 3.4, the influence of anneal temperature on carrier lifetime and dark resistance was explored. The dark resistance increases with temperature, changing by large amounts at 350 °C and 475 °C and showing little variation after these temperatures. The carrier lifetime shows similar properties, decreasing at 450 °C and 575 °C.

These annealing properties suggest two optimal anneal temperature regions, marked on figure 3.4 as zone I and II. In zone I, the dark resistance is not very large, but the carrier lifetime is also low. This anneal temperature would provide devices with very fast carrier dynamics and higher bandwidth, but lower signal to noise ratio. Zone II has a much larger dark resistance, but also a longer carrier lifetime, increasing the SNR, but decreasing bandwidth.

3.4.3 Anneal Tests

While it was possible to take previous work as a model for desired anneal temperatures [12] [43], as LT-GaAs wafers are optimized for better performance, the best anneal temperature could change between wafers grown in different MBE machines (with different growth rates and temperature calibrations). Therefore, a series of devices were fabricated to determine the optimum anneal temperature for the wafer used throughout this work. The devices fabricated were coplanar waveguides with two switch pairs each. The temperatures chosen were from 525 °C to 625 °C in steps of 25 °C

Three parameters were extracted from these devices: the dark resistance, the input pulse FWHM (as an indicator of carrier lifetime), and the signal-to-noise ratio (SNR). The dark resistance was calculated by taking I-V sweeps at a PC switch with no illumination. This gave a response that was partly capacitive in nature, and partly linear. The capacitive response depended on the geometry of the device, while the linear response depended on the dark resistance of the LT-GaAs switch. By taking a linear fit of the I-V, the capacitive element could be averaged out, and the linear element

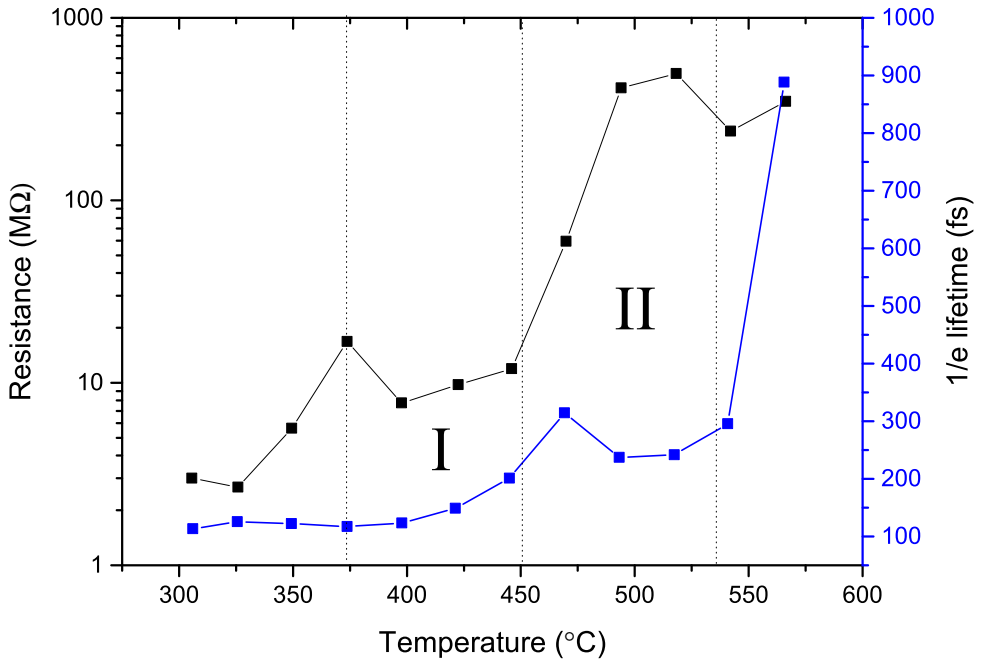

Figure 3.4: As the anneal temperature is increased, the dark resistivity (black) increases, but the carrier lifetime (blue) decreases. Zones I and II represent the two optimum anneal temperatures for different applications. Zone I (II) will have a higher (lower) bandwidth, but worse (better) signal to noise ratio. (figure taken from [12])

extracted, allowing the dark resistance to be calculated.

For FWHM and SNR measurements, one switch pair was used to excite and detect the pulse. A bias was applied to one switch arm and current measured in the other switch arm (input pulse). More information about on-chip measurement methods will be discussed later in section 3.5. An input pulse was measured in each device and the FWHM measured. To obtain the SNR, the amplitude of the noise before the THz pulse was compared with the amplitude of the THz pulse itself.

Results from these three tests are shown in figure 3.5. The error for these results is rather large due to considerable variation in pulse amplitude and noise between different switch configurations, and more devices would need to be fabricated to be confident in measured values. As a method of comparison for in-house fabrication, however, it

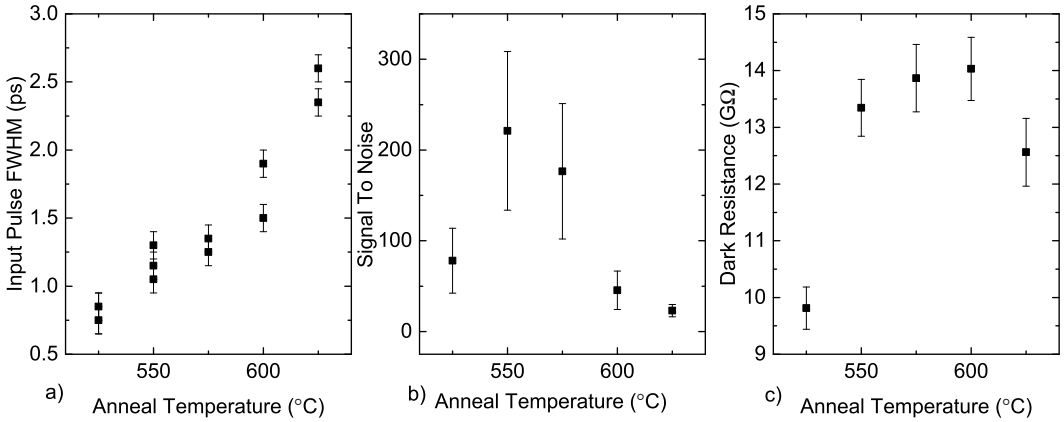

Figure 3.5: a) The FHWM of measured input pulses, b) the signal to noise ratio of the same input pulses, and c) the dark resistance of LT-GaAs switches.

was deemed sufficient to show that the best anneal temperature was either 550 °C or 575 °C, especially since the results are consistent with previous wafers which performed best after annealing at 575 °C. However, since 550 °C had a slightly better bandwidth, this temperature was settled on for all the devices studied in this thesis.

3.4.4 Initial Epitaxial Transfer Recipe

Chips of LT-GaAs on SI-GaAs were formed from scribing and cleaving the MBE-grown wafers to the desired size (generally 2 by 3 mm). They were then sonicated in acetone, isopropyl alcohol (IPA) and deionised (DI)-water at low power in a plastic beaker to avoid micro-cracking. After cleaning, they were annealed at 550 °C for 15 min in a nitrogen atmosphere. Apiezon Wax W (referred to henceforth as black wax) was then melted on the LT-GaAs surface as seen in figure 3.6. The wax acted both as a mask to resist acid, and also as structural support for the 350 nm thick piece of LT-GaAs after lift-off.

The black wax would generally melt to the edges of the chip, and it was necessary to clean the edges of the chip in order to ensure that the AlAs etch layer was fully exposed. An edge clean was performed with cotton buds dipped in Trichloroethylene, and the chips were then visually inspected under a microscope to ensure that there was no wax residue after the cleaning.

As an additional step to ensure that the AlAs etch layer was exposed, the chips were then cleaned for one minute in a non-selective sulphuric acid solution (H_2SO_4 : H_2O_2 : H_2O, 1:40:80). The etch rate for this solution was not known, however, from post-processed samples it was evident that this step was sufficient to etch through the entirety of the LT-GaAs layer. Each chip was then placed directly in a separate slow hydrofluoric acid (HF) etch solution (HF:H_2O, 1:9) and left there at 3 °C for 24 h (for 2×3 mm chips). This length of time was generally sufficient to completely remove the AlAs layer, and the LT-GaAs would then be fully separated from the substrate. The slow etch is necessary to preserve the LT-GaAs layer, since the chemical reaction between the HF and AlAs layer produces gas bubbles that will crack the LT-GaAs if the reaction rate is too rapid.

In order to remove the LT-GaAs from the HF solution, the HF solution was repeatedly diluted with DI-water and drained away from the LT-GaAs chip. After sufficient dilution, the LT-GaAs chip was trapped on the surface tension of the water in a beaker. It was then possible to pick up using a vacuum probe and to place it on the substrate of interest. It was ensured that a thin film of water was between the LT-GaAs and the substrate in this step, as the subsequent slow evaporation of water seemed to improve adhesion. Prior to this, the substrate (typically quartz) was prepared by sonicating in acetone, IPA, and DI-water at high power, and finally plasma ashed for 10 min to ensure the removal of any organic contaminants.

The LT-GaAs was then left on the substrate at room temperature for around one week to allow complete Van-der-Waals bonding between it and the substrate [43], before the black wax was removed in trichloroethylene. The substrate was then repeated dipped in DI-water to allow the surface tension of the water to remove any pieces of LT-GaAs that had not bonded properly, with blasts of nitrogen air from a cleanroom gun also used for the same reason. As a final step, the device was baked at 250 °C for 15 h under vacuum to ensure complete dehydration and to further improve adhesion.

3.4.5 Recipe Changes

Two main improvements were made to the above recipe over the course of this work, which involved altering the edge-clean process, and improving the HF etch. These

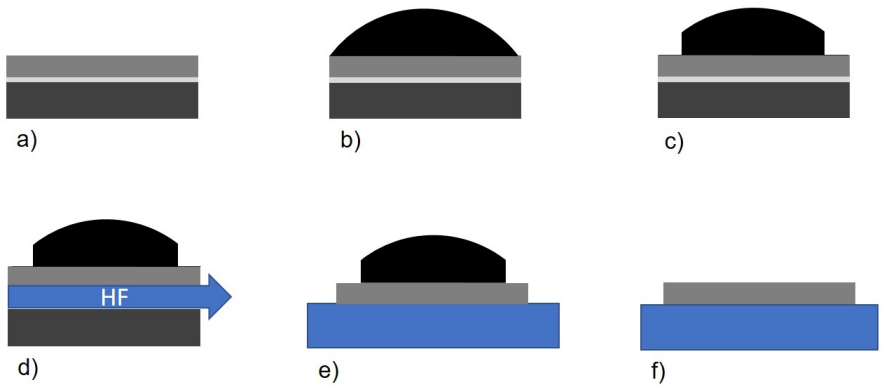

Figure 3.6: a) A chip of LT-GaAs is diced to size, cleaned and annealed, b) black wax is melted onto the surface, and c) the edges are cleaned with Trichloroethylene. d) The chip is cleaned in sulfuric acid, then placed in HF to etch through the AlAs sacrificial layer and allow the LT-GaAs to lift-off from the SI-GaAs substrate. e) The black wax gives sufficient structural stability to transfer the piece of LT-GaAs onto the substrate of choice, and f) after bonding, the black wax is removed in Trichloroethylene.

changes were made to reduce the complexity of the recipe and also to reduce contact with trichloroethylene and HF, both of which are hazardous to the user.

Instead of allowing the black wax to melt over the whole surface of the sample, less wax was used, and it was not allowed to melt to the edge of the sample. This ensured that the AlAs layer was not covered by the wax. As an extra precaution, the non-selective sulphuric acid etch time was increased to three minutes, so that the LT-GaAs and AlAs not covered by the wax would be completed etched away, thus exposing a fresh AlAs surface for the HF etch. This eliminated the tedious and potentially hazardous edge-clean step.

In the HF etch step, the original recipe called for each chip to be placed in a separate solution. This meant that when processing multiple chips, there was potential exposure to a large quantity of HF acid. This process was altered so that rather than using an individual bottle per chip, up to ten chips could be placed in the same solution. No obvious change in failure rate (typically 10-30 percent) was noted through the introduction of this 'batch processing'. The change, though simple, greatly reduced

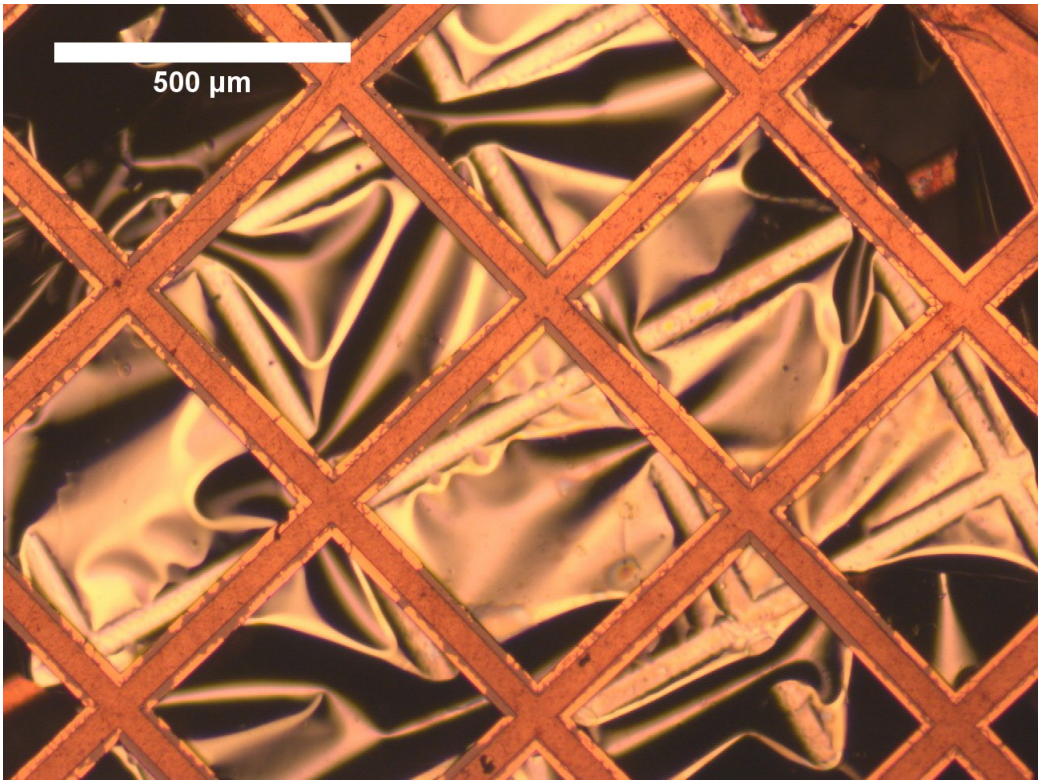

Figure 3.7: A 100 nm thick film of FeRh sandwiched between two TEM grids.

the processing time of this part of the recipe while also greatly reducing the volume of HF handled.

3.4.6 Epitaxial Transfer of Metals

While the epitaxial transfer recipe was principally used for LT-GaAs, it was also adapted to transfer metal films of iron rhodium (FeRh) in a collaborative work. I was responsible for the transfer process only, but a brief description of the experiment is included for context (contributed by Jamie Massey).

The films were used to measure the dynamic behaviour of the magnetic domains in FeRh using X-ray Correlated Photon Spectroscopy at various points in the metamagnetic transition. In order to do this it was necessary to access the scattering from magnetic domains in FeRh. The micrometer size of the magnetic domains in this material mean that the Bragg scattering angle expected from them is around 0.05 degrees.

Naturally, measuring such a scattering pattern is extremely difficult in the reflection geometry traditionally used in X-Ray scattering experiments. Therefore, in order to measure the dynamical behaviour of the magnetic domains, it is necessary to work in the transmission geometry in which the beam passes directly through the sample with the detector placed behind it. This gives access to very small scattering angles and so the resultant scattering pattern from the magnetic domains can be measured.

The use of the transmission geometry requires the sample to be X-Ray transparent, which limits the sample thickness to several hundred nanometres. As FeRh requires a specific ordering to demonstrate the metamagnetic transition, the samples must be grown on a lattice matched substrate and so cannot be grown on traditional X-ray membranes. So the lift off procedure is required to remove the film from the substrate in such a way that they preserve the metamagnetic transition in FeRh and can then be used in X-ray scattering experiments in the transmission geometry (end of contributed text).

FeRh was grown on a wafer with an AlAs sacrificial layer analog to the LT-GaAs wafer previously described. The epitaxial transfer recipe was followed up to right after the lift-off point. However, instead of transferring the metal film to a substrate, it was necessary to transfer it to a transmission electron microscope (TEM) grid instead, and the recipe was adapted to allow this.

A strip of cleanroom tissue was dipped in the beaker of water with the metal film, and lifted up so as to catch the metal film on its surface, with the metal stuck to the cleanroom tissue, and the black wax facing out. The strip of tissue was then laid in trichloroethylene to allow the black wax to dissolve. This removed the protective wax layer so that the metal film was supported only by the tissue. The tissue was then dipped into water, and the surface tension of the water removed the metal film from the tissue so that the metal floated on the water surface. A TEM grid was then used to scoop the metal from the surface of the water, and a second grid was used to sandwich the film in place. GE varnish was used to bind the two TEM grids together, and the end result was robust enough to handle (carefully) with tweezers, and thin enough to allow transmission measurements to work.

3.5 THz On-Chip Measurements

3.5.1 Pump-Probe Methods

Pump-probe methods were used to detect on-chip THz pulses throughout this work. The principle of operation is as follows. The device under test (DUT) is excited by a 'pump' signal, and a 'probe' signal is then used to determine the effect of excitation on the DUT. The relative time of arrival of these two signals is controlled to allow time-resolved measurements. In this work, a femtosecond pulsed laser source was used to provide the pump and probe signals.

3.5.2 On-Chip Measurements

Over the course of this research, a Ti-Sapphire laser and a fibre laser were used. They both had repetition rates of 80 MHz, each giving pulses with a FWHM of 100 fs, and with the centre wavelength at 800 nm. The photon energy was thus greater than the bandgap (1.4 eV) of the LT-GaAs photoconductive switches used for the on-chip THz devices measured. The spot size of the beam focused on the switch was around 30 µm.

A beam-splitter was used to split the output of the laser into two paths. Laser pulses in the pump path were used to excite a THz pulse, while laser pulses in the probe path were used to measure the THz pulse. As is normal with pump-probe measurements, the arrival time of the probe pulse relative to the pump pulse determines what part of the signal is being sampled. Therefore, a retroreflector was mounted on a motorised delay line and included in the probe beam path, allowing the relative arrival time of the two optical pulses to be controlled. A schematic of this setup is shown in figure 3.8.

For the sake of clarity, some terminology will now be introduced. When referring to the switches on on-chip THz devices, the name 'switch' will be used to label the actual LT-GaAs photoconductive material, 'switch arm' refers to a single metallic contact on the photoconductive switch, while 'switch pair' refers to the pair of metallic contacts on a photoconductive switch. These terms are illustrated in figure 3.9.

To excite a THz pulse in the coplanar "odd" mode, a positive and equal bias is applied to each switch arm in a switch pair, and the ends of the centre conductor are

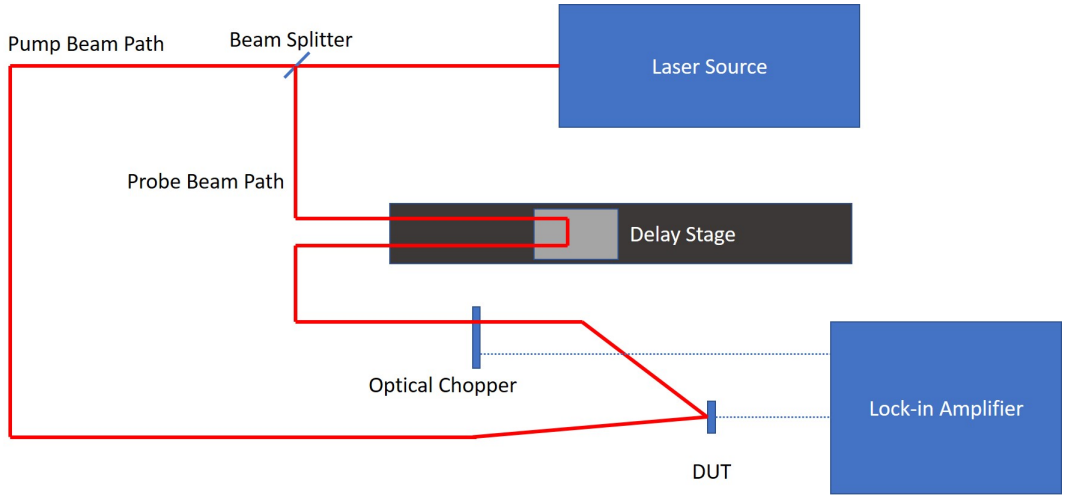

Figure 3.8: A simplified schematic of the optical bench setup for on-chip THz measurements.

grounded, along with the ground planes. When the optical probe pulse illuminates the switch, charge carriers are generated, and the bias applied through the switch arms drives a current pulse, in turn generating an electromagnetic wave, part of which couples into the waveguide.

In order to sense the propagating THz pulse, the optical probe pulse must be incident on a different switch at the same time as the transmitted THz pulse. In this case the situation is the opposite to excitation. It is the THz pulse that supplies the electric field to drive a current, which is detected by a lock-in amplifier which operates at the frequency of an mechanical chopper in the optical beam path. To map out a THz pulse, the motorised stage on the delay line is slowly moved, changing the arrival time of the probe pulse relative to the pump pulse, and therefore sensing a different portion of the propagating THz pulse. For reference, one meter difference in beam path would correspond to about three nanoseconds in time delay.

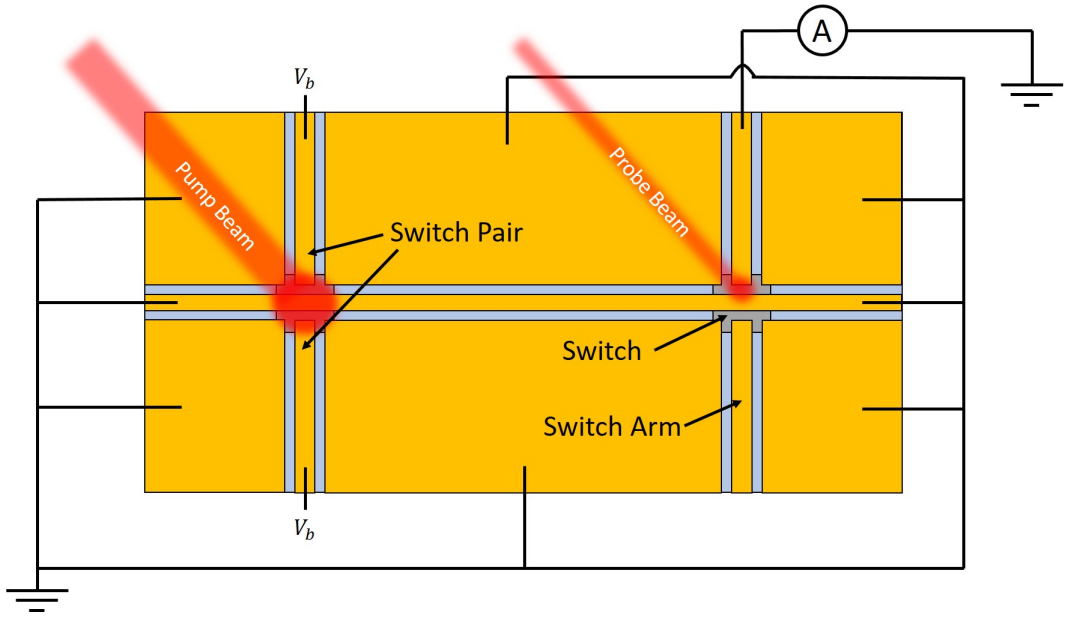

Figure 3.9: A schematic of a CPW device configured to measure a transmitted THz pulse. The Ammeter symbol would actually be a lock-in amplifier set up to measure current and synced with an optical chopper in the probe beam path.

3.6 DC Lateral Spin Valve Measurements

As described in Chapter 2, the advantage of LSVs is the capability of separating the charge and spin current contributions. A charge current is passed through FM1 into a NM spacer wire, inducing a spin accumulation at the FM1/NM interface which diffuses in both directions along the NM wire. Between FM1 and FM2, no charge current flows, but there is a spin current due to the diffusion of the accumulated spins. When the non-local voltage is measured between the NM and FM2, the voltage shift as the magnetisation changes from parallel to antiparallel reflects the magnitude of the spin accumulation.

To measure the spin current at DC, non-local IV sweeps are performed. Here, a current is passed through FM1 to the NM wire, and the voltage is measured between FM2 and the NM wire. This is referred to as a non-local measurement, since the voltage is measured separate from the current loop (illustrated in figure 2.7a). The IV curves measured include a quadratic and linear component, where the quadratic component is

generated by heating effects, and the linear component is derived from spin current. By extracting the linear component, the magnitude of the spin current can determined. This method was developed by previous researchers at the University of Leeds, and more information can be found in their work [40].

3.7 Chapter Summary

In this chapter, fabrication and experimental methods were discussed. The general principles of lithography and metallisation were outlined as they pertain to the devices fabricated in the course of this work, as well as the epitaxial transfer recipe for LT-GaAs. Improvements made to this recipe during the course of the thesis work were highlighted. Finally, experimental methods for both on-chip THz measurements and DC LSV measurements were explained.

Chapter 4

Magnetic waveguides

4.1 Chapter Overview

Waveguides were made out of magnetic metals to test the capability of on-chip devices for picosecond magnetic measurements. Initial devices were made from a combination of gold and a single layer of magnetic metal (Py), which demonstrated successful transmission, but did not originally reveal any magnetic field dependence. In order to see a THz magnetic field response, devices were then made from Co/Cu multilayers, designed to show giant magnetoresistance. This chapter outlines the fabrication, measurement, and analysis of these magnetic waveguides.

4.2 Magnetic waveguides version 1

The first magnetic waveguides fabricated in this work were gold/permalloy (Au/Py) hybrid devices, where the ground planes and switches were made of gold, and the centre conductor was made of Py (Ni[80%], Fe[20%]). These devices were made to demonstrate THz pulse injection into a magnetic metal, to potentially demonstrate THz AMR effects, and to highlight any potential fabrication problems associated with the deposition of magnetic metals.

For these devices LT-GaAs was transferred as previously described in Chapter 3. A slow sulphuric etch (H_2SO_4:H_2O_2:H_2O,1:8:950) was used to etch the LT-GaAs into 70 µm by 70 µm squares, and LOR 3A/S1813 bilayer lithography was used for both the Ti/Au layer and the subsequent Py layer. Thermal evaporation was used to deposit Ti/Au (10/150 nm) for the switches and ground planes, and Ebeam evaporation was used to deposit Py (100 nm). The final device would be similar to the schematic shown in figure 4.1.

The Ti/Au metallisation and lift-off worked as expected, but serious issues were encountered with the Py lift-off. The majority of the device looked good, however, the squares of LT-GaAs tended to be badly damaged, or entirely gone (shown in figure 4.2). This was attributed to differential cooling between GaAs and the Py layer after deposition (linear thermal expansion coefficients of approximately 6 and 13 $\times 10^6$ °C^{-1}, respectively). That is, the Py was hot (melting point of approximately 1400 °C) when evaporated onto the sample, and subsequently cooled, contracting and introducing

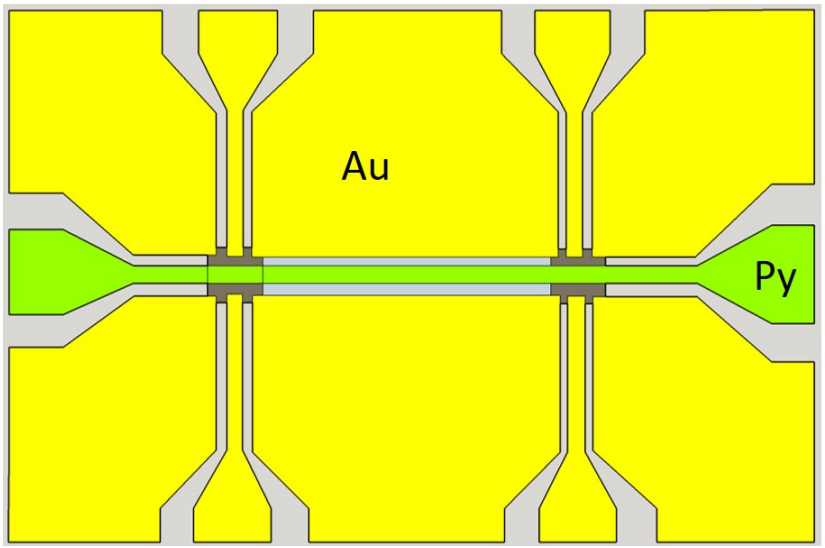

Figure 4.1: A simplified schematic of version 1 magnetic waveguides. The switch arms and ground planes were fabricated from Ti/Au, and the centre track was fabricated from Py. Figure not to scale.

tension in the metal layer. Since the LT-GaAs is not very strongly bonded to the quartz, the induced tension was sufficient to peel it off.

A series of devices were made to try and remove this effect, varying Py thickness while also adding a Ti adhesion layer. However, none of these changes worked sufficiently. It was determined that the Ebeam evaporation process was unlikely to work, and some other form of metallisation would have to be implemented.

Sputtering is one of the most common methods used for magnetic metal deposition. However, as mentioned previously, it is highly non-directional, with a low mean free path. As a result it was not originally considered as a viable option of metallisation for our devices. However, due to the incompatibility of the Ebeam evaporation of Py with LT-GaAs switches, it was necessary to attempt this method. It was found that the LOR/S1813 bilayer resist combination was capable of providing a sufficient undercut for a clean lift-off.

Sputtered Py did not exhibit the stressy properties observed in evaporated Py, and the LT-GaAs switches remained intact. As a result, sputtering was the method of choice for subsequent deposition of magnetic metals. THz pulse transmission was successfully

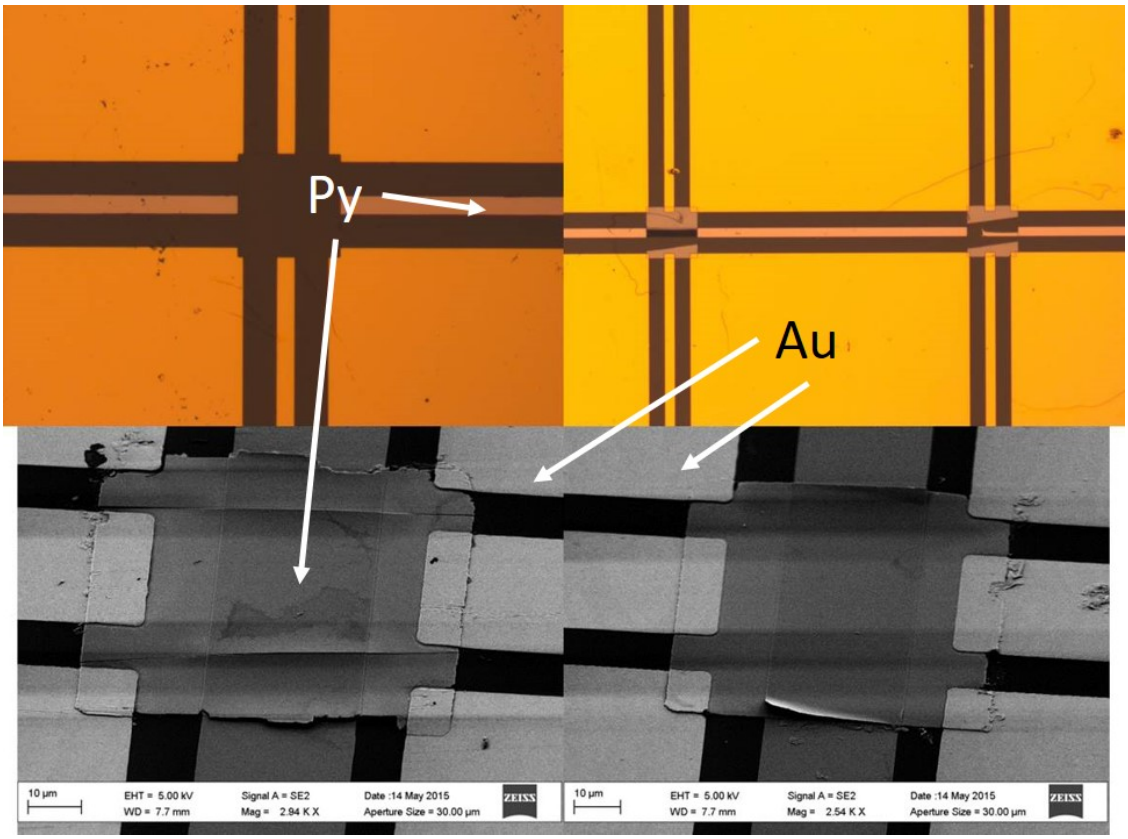

Figure 4.2: After Py evaporation, the LT-GaAs either came off (top left) or was badly damaged (top right). By changing Py thickness and adding a Ti adhesion layer, the result was improved (bottom SEM images), but devices were still too damaged to work.

demonstrated for these devices, but initially no magnetic field dependence was noted. Later, however, after improvements were made to the measurement sensitivity and averaging techniques adopted, a THz AMR was measured, as discussed in section 4.7.

4.3 GMR Calibration

In order to produce samples with a strong room temperature magnetic field dependence, it was decided to fabricate waveguides out of metallic multilayers that exhibited GMR properties. The materials chosen were cobalt and copper since high GMR values can be achieved using these two metals. In order to achieve a good GMR value, it was necessary to tune the thickness of the metal layers used.

Historically, it was experimentally observed [44] that the GMR value of a magnetic multilayer oscillated with the thickness of the non-magetic spacer layer. This was true for a number of metal combinations, including Co/Cu (see figure 4.3), Co/Ru, Co/Cr, Fe/Cr, Fe/Al, and Fe/Au [44–46]. Theoretically, this phenomena can be explained via the oscillatory exchange interaction. Practically, this meant that it was necessary to tune the thickness of our Cu layer to coincide with a maxima of the GMR oscillation.

4.3.1 Oscillatory Exchange Interaction

The oscillatory exchange interaction describes a mechanism by which the ferromagnetic layers in a multilayer interact with each other via the conduction electrons in a non-magnetic spacer layer. While a full review and mathematical framework is beyond the scope of this thesis, a brief description will be provided to aid understanding. For a full analysis, the reader is directed to Bruno's paper on the subject [47].

Consider a metallic 'sandwich' with two FM layers and a NM spacer layer. If a conduction electron is represented by a Bloch wave of momentum k_i, then, as it passes from the NM layer into a FM layer, it experiences a different potential at the interface, and part of the wave with momentum k_r is reflected back into the NM layer. The incoming and reflected wave interfere to form a standing wave with a periodicity determined by the scattering vector $q = k_r - k_i$. Assuming a perfect multilayer system, q will be perpendicular to the FM/NM interface. Because the potential step at the

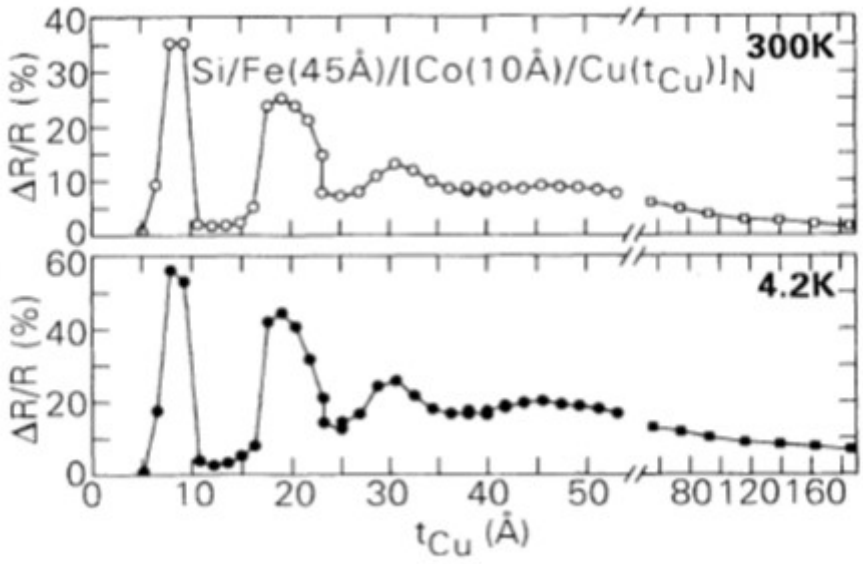

Figure 4.3: Data from Parkin's systematic study [44] investigating GMR response as the Cu spacer thickness is systematically changed in a Co/Cu multilayer. Data shown at 300K (top) and 4.2K (bottom)

interface depends on the electron's spin relative to the FM layer magnetisation, the reflection amplitude will also be spin dependent. This means that the standing wave is asymmetric in spin, and the spin polarisation will oscillate in the NM layer. The net polarisation is the result of contributions from all electrons with different scattering vectors, so it is expected to reduce as the distance from the interface increases.

The reflected component will then itself be reflected when it encounters the second FM layer, with multiple reflections occurring at each interface. The energy generated by the corresponding interferences represents the coupling interaction between the two FM layers. This energy oscillates as a function of the NM gap size with a period of $2\pi/q$. Contributions from electrons at the fermi level are the only ones that are not mostly cancelled, and so the period becomes $2\pi/k_F$. From this treatment, it becomes apparent that this exchange interaction is strongly dependent on the fermi surface of the metals involved, and also on the strength of the spin dependent reflection.

4.3.2 Thickness Calibration

Since the spin polarisation in the spacer layer oscillates with thickness, it is necessary to tune the thickness so that the FM layers are antiferromagnetically aligned if there is no external field. If an external field is then applied to these samples, the magnetic layers can be forced into the ferromagnetic (FM) alignment. As explained in Chapter 2, the resistance of GMR multilayer changes when the layers are aligned or antialigned (parallel or antiparallel), and therefore, the resistance of the GMR multilayer can be controlled via an external magnetic field.

In order to ensure that the magnetic layers were grown in an antiferromagnetic orientation, a number of samples were grown, and the thickness of the Cu spacer layer systematically changed. From figure 4.3, it is known that the first antiferrmagnetic peak occurs when the Cu thickness is around 10 Å, so this was the target thickness for the samples grown.

Sputter rates were assumed (from prior work on the deposition system) to be $2\,\text{Å}\,\text{s}^{-1}$ for both Co and Cu given a Argon pressure of 2.4 mTorr and powers of 36 W and 9 W respectively. Assuming these rates, samples were grown with a constant Co thickness of 20 Å and Cu thicknesses ranging from 4 Å to 16 Å in steps of 2 Å for a first calibration batch, and then from 12 Å to 17 Å in steps of 1 Å in a second calibration batch.

The total multilayer thickness was measured using X-ray diffraction, and, since the Co thickness was constant across all samples, while only the Cu thickness was altered, the real sputtering rates could then be determined. It was thus found that the sputtering rate for Cu was $1.5\,\text{Å}\,\text{s}^{-1}$, and the rate for Co was $3.4\,\text{Å}\,\text{s}^{-1}$. These rates were used to determine the actual thickness of the Cu and Co layers.

Four point measurements were performed on the planar multilayer samples while an external magnetic field was applied in order to determine the GMR. An example of a "good" GMR response is shown in figure 4.4a, and the magnitude of the GMR response with changing Cu thickness is shown in figure 4.4b. The largest GMR values are found for a Cu thickness of 11 Å, corresponding well with the first antiferromagnetic peak in the previously published results [44].

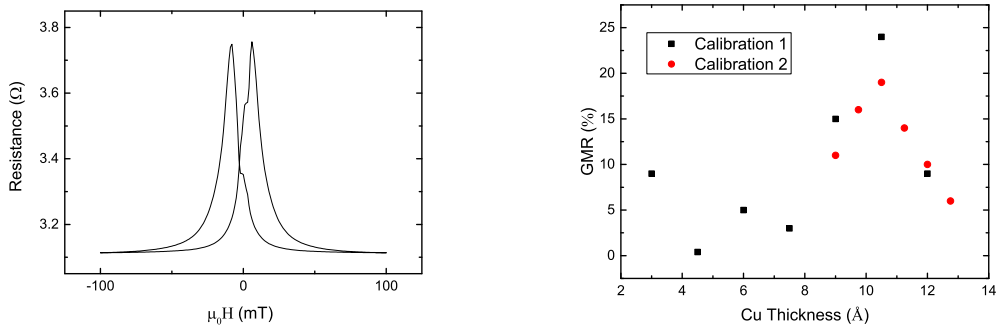

(a) (b)

Figure 4.4: a) A good GMR response for a multilayer sample at room temperature. b) The GMR response as the Cu thickness is changed. The antiferromagnetic peak is seen at 11 Å. More devices would need to be grown to determine the fabrication uncertainty.

4.4 Goubau Lines

The first geometry used to test THz transmission in GMR waveguides was a planar Gobau line in reflection mode. This was effectively just a single wire on a quartz substrate with a single switch pair (schematic shown in figure 4.5a). On one side of the switch, there was a relatively short length of wire (generally less than a millimeter) and on the other side was a long length of wire designed to eliminate reflections. One switch arm in the switch pair would generate the THz pulse, while the other switch arm would detect the pulse, analogous to detection of an input pulse. The THz pulse would couple to the waveguide and be reflected off of the short end of the waveguide. This meant that an 'input' scan measured both the input pulse, and a transmitted pulse after reflection (seen in figure 4.5b). Since the same switch arm was used for both measurements, direct comparison of the pulse amplitudes was possible. Also, since both the input pulse and the transmitted pulse were included in the same scan, it was then easy to calibrate for small fluctuations in laser power between different scans by scaling each scan by the input pulse amplitude.

However, no clear change in pulse amplitude was noted as the external magnetic field was changed. It was surmised, and later confirmed with HFSS simulations, that this was because the electric field is only loosely bound to the metal in the Gobau line

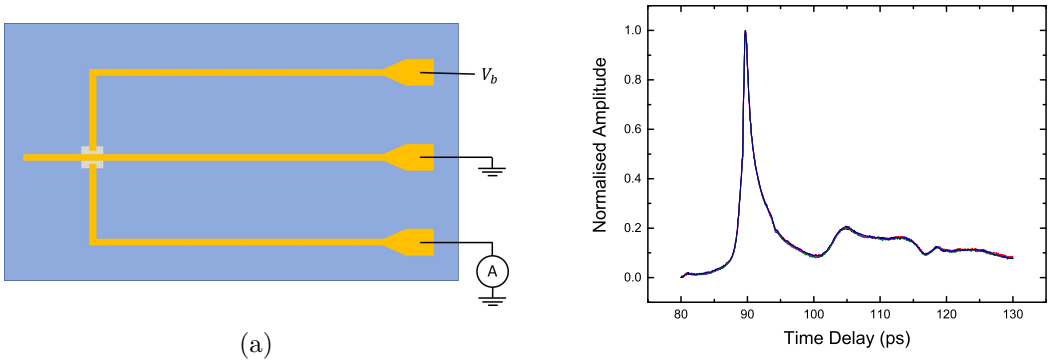

(a)

(b)

Figure 4.5: a) A schematic of a Goubau line. A bias is applied at one switch arm, and the THz pulse is detected at the other switch arm. b) Pulses from a Gobau line in reflection geometry. The first pulse at 91 ps is the input pulse, and the transmitted pulse is seen at 104 ps. Multiple scans are shown here, taken at different external magnetic field strengths and scaled according to the input pulse amplitude. No clear change with external field is noted.

geometry. This means that there is relatively little interaction between the electric field and the metal being studied. Therefore, it was decided to return to a coplanar waveguide geometry, in which the field is more confined.

4.5 CPWs

CPWs were made fabricated, where the width of the centre conductor was 30 µm and the gap between the centre conductor and the ground planes was 10 µm. Transmission measurements were made as previously described in section 3.5.2, and the increased confinement in the CPW geometry made the THz GMR response measurable. Transmission measurements in the slotline (even) mode were made, and it was shown that the magnetoresistance response decreased for this less confined mode. This is shown in figure 4.6. Field sweeps were also performed before and after the THz pulse in both the transmission and input measurement setup to investigate if the magnetic field response of the THz trace was consistent throughout.

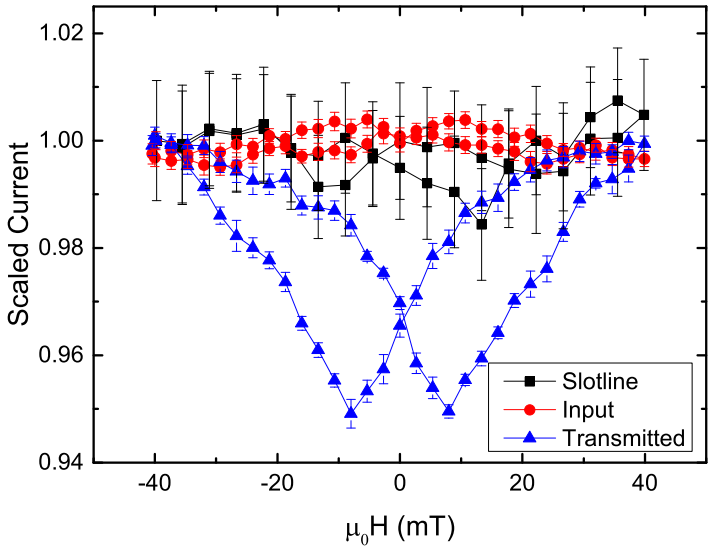

Figure 4.6: A comparison of the THz GMR response for different measurement configurations in a CPW. Lines are included as a guide for the eye. The slotline data is much noisier, since the signal strength was smaller relative to data taken in the coplanar mode.

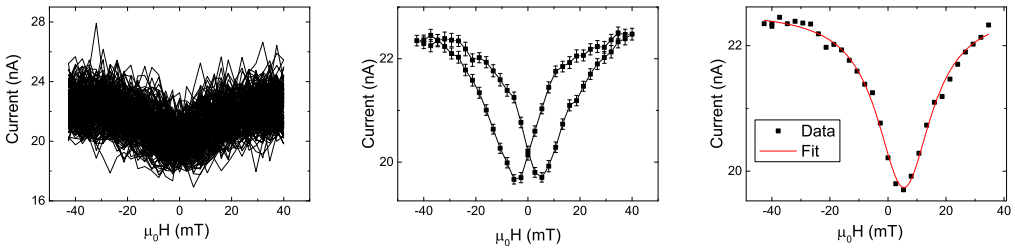

(a) (b) (c)

Figure 4.7: a) Raw data from 100 field sweeps is shown. b) Python code was used to obtain the mean value and standard error for each data point, and c) this data was then fitted with a Lorentzian function.

4.5.1 Measurement Automation

To better perform magnetic field sweeps for different positions along the THz trace, LabVIEW code was written to automate the process of data acquisition. Code was written so that the user could control the parameters relating to the magnetic field sweeps (start and end magnetic field strengths, step size, and wait time per step) as well as the parameters controlling the time delay (ie. the moveable stage) for which measurements were performed (start and end time delay, step size, option to zero at an offset point). The LabVIEW code then returned all current values measured for each field sweep (figure 4.7a). Python code was written to average all the data, and the mean value was returned, as well as the standard error value (figure 4.7b). This data was then fitted with a Lorentzian function (figure 4.7c), and four parameters were returned, namely amplitude, full width half maximum (FWHM), baseline, and peak position.

4.5.2 Field sweeps along the THz trace

THz pulses were first measured for different external magnetic fields, corresponding to different DC resistances. Example pulses for both the high and low conductivity resistance are shown in figure 4.8a. Here the ohmic behaviour of the peak is obvious. Zooming in on the pulse tail, however, shows what appears to be non-ohmic behaviour, with a higher current measured in the low conductivity configuration. To clarify this

behaviour, magnetic field sweeps were performed at different time delays along the THz trace and the current response to the external magnetic field was measured (referred to later as magnetic response). Transmission data was similar to that shown in figure 4.8b for multiple devices. The response can be split into two zones, with a transition zone in between. In zone I, the response is as would be expected from Ohm's law (Fig. 4.8c). When the DC resistance of the waveguide is high (low), a lower (higher) current is recorded. However, in zone II the opposite response is recorded; that is a high (low) current is recorded in the high (low) resistance configuration (Fig. 4.8d). This will be called an inverse response or inverse GMR (iGMR) for our purposes.

In both zones, the magnetoresistance scales with the THz pulse, and therefore, while changing the applied voltage or laser power will affect the magnitude of the response, it does not significantly affect the percentage change. This can also be phrased in terms of the fit parameters for the magnetic response; the fit amplitude changes with voltage, but the fit amplitude divided by the fit baseline does not significantly change. Measurements were also carried out at 10 K in a microstat. Here the percentage change increased slightly, but the results were otherwise similar.

It is also worth mentioning the signal behaviour in the transition zone. Here, there is very little magnetic response with external field as the signal changes from normal Ohmic behaviour to iGMR behaviour. However, in a number of samples, there appeared to be an interference like effect, as if the normal GMR and iGMR were being added together (shown in figure 4.8e). This is unusual, since it suggests that two separate effects are at play.

The FWHM of the magnetic response tended to decrease in the initial picoseconds of zone I. It generally started at around 35 mT and dropped to around 20 mT as the Ohmic part of the magnetic response started to disappear. This is shown in figure 4.8f. What is interesting here, is that the FWHM measured at DC was 21 mT, and the FWHM of the initial THz response is quite a bit larger, then tends to the DC value in the following picoseconds as seen in figure 4.8f.

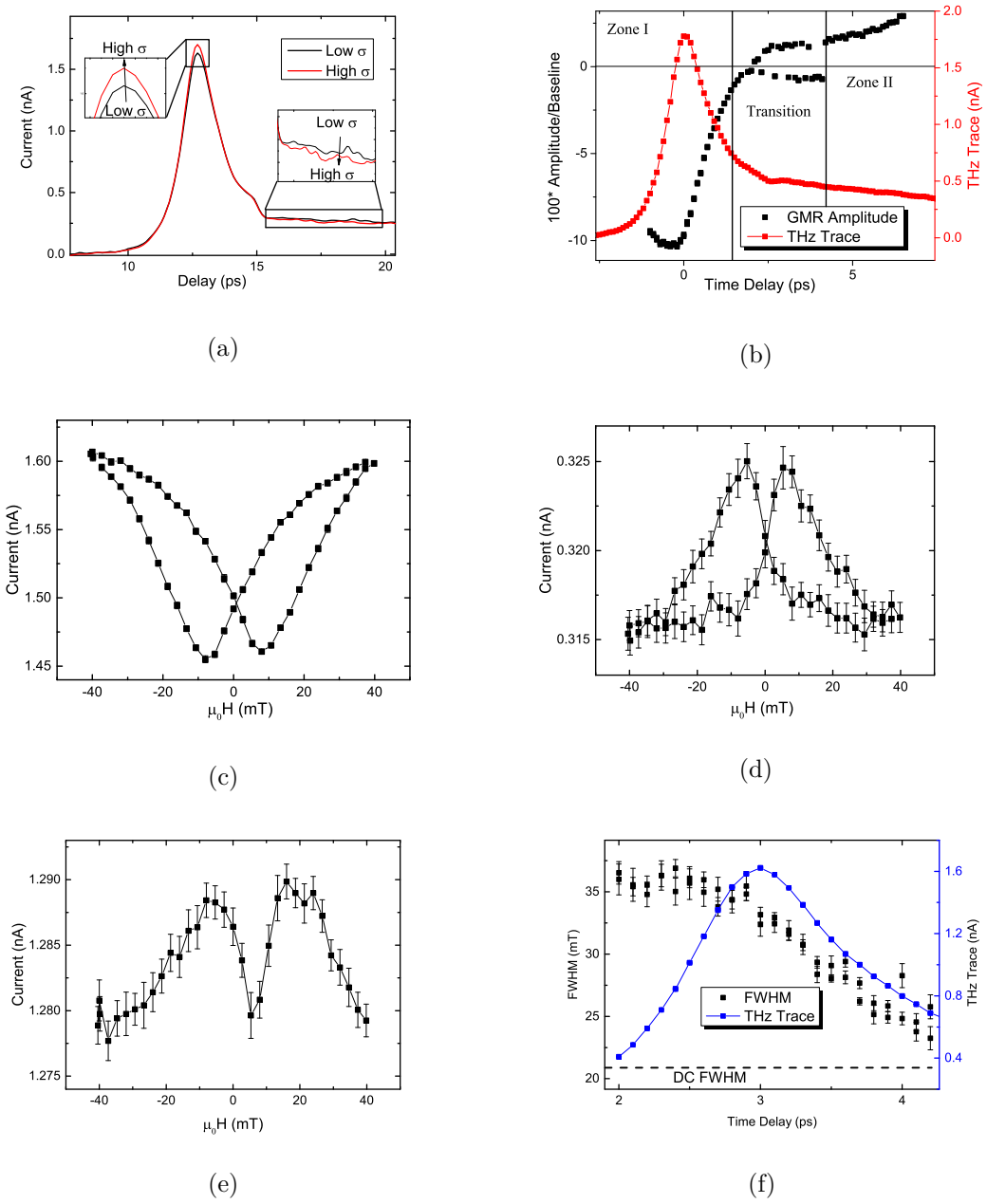

Figure 4.8: a) THz scans for external magnetic fields that provide a low and high conductivity. The pulse peak position shows Ohmic behaviour, but the pulse tail appears to show the inverse behaviour. b) This behaviour is clarified by measuring the magnetic response along the THz pulse. The data can be spit into two zones, Zone I, where c) the data matches what is expected from Ohm's law, and Zone II, where d) the data is the inverse of what is expected from Ohm's law. e) In the transition region, sometimes there appears to be an interference effect, where the field dependence shows elements of both normal and inverse GMR. f) Over about one picosecond the FWHM of the THz magnetic response drops from 35 mT to 23 mT. The FWHM of a DC response is shown at the dashed line.

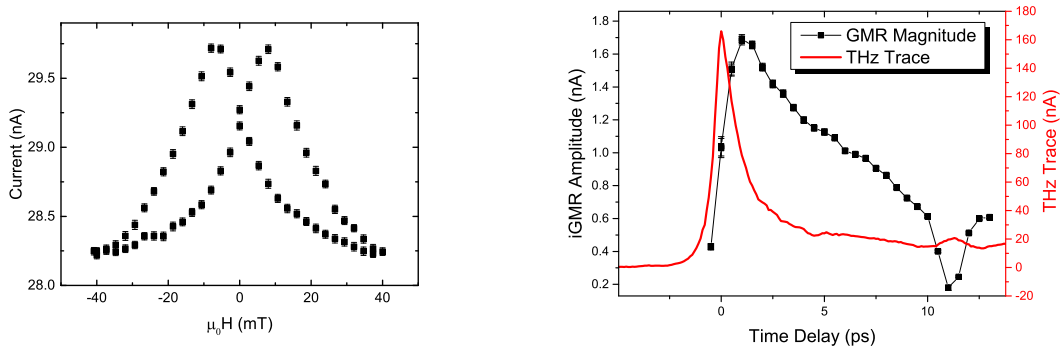

(a) (b)

Figure 4.9: a) The current response with external field for an input pulse two picoseconds after the THz pulse peak b) The current response for each time delay is fitted with a lorentzian, and the amplitude and baseline of the response are plotted as a function of the time delay. The baseline shows the THz pulse, and the amplitude shows the magnitude of the magnetic response. The dip in the magnetic response at 11 ps corresponds to a reflection from the neighbouring switch.

4.5.3 Input pulse measurements

Input pulse measurements were also performed, where one switch arm in a switch pair was used for excitation and the other switch arm was used for detection. In this configuration only zone II type behaviour was measured (Fig. 4.9a), with almost no magnetic response at the THz pulse peak position, and with the largest response found about 1 ps after the peak position. A typical input response is shown in figure 4.9b. It is worth noting that the iGMR signal is reduced at the same point as the reflection from the neighbouring switch.

Similar to the magnetic response from transmission measurements, the magnetic response for the input pulse scales with the THz pulse. That is, the percentage change (fit amplitude/fit baseline) remains largely constant as laser power and voltage are changed.

4.6 iGMR Discussion

From the data shown, it appears that the GMR CPWs exhibit both normal and inverse GMR properties. Inverse GMR has been measured before [48–50], but only in specially prepared samples that were deliberately engineered to generate that response. This requires a minimum of three metals as the interface or bulk qualities of the multilayer are adjusted. In the samples measured here only Cobalt and Copper were used, and the measured DC magnetoresistance is what would be expected.

These leaves a number of options to explain these results. The simplest is that the effect is an artefact of measurement and does not actually exist. This will be discussed first. Other possibilities include demagnetisation or spin accumulation effects, which are discussed later.

4.6.1 Artefact?

When first measured, it was suspected that the unusual THz GMR results were not real. In order to ensure that they were not an artefact caused by the measurement setup, a number of tests were performed. First, ordinary non-magnetic devices were tested at different time delays. No magnetic response was measured, eliminating the LT-GaAs switches as a possible source of the magnetic response. Next, more devices were made to see if they behaved in the same way. The THz GMR effects were measured in more than six devices, and consistent behaviour was observed in terms of there begin two regimes of device operation as above. Over the range of devices it was also noted that the devices with the largest DC GMR also showed the largest THz GMR effects, which makes intuitive sense.

To ensure that the THz GMR was not a result of the optical light from the laser, the polarisation of the probe pulse was changed with a half-waveplate; this had no effect on the magnetic response. Changing the polarisation to circularly polarised with a quarter-waveplate also had no effect.

Most of the devices made were entirely made of Co/Cu multilayers, including switch arms and ground planes. To ensure that the response was not due to GMR effects in the switch arms, a device was made in which the switch arms and ground planes

were made from Ti/Au (10/150 nm) and only the centre conductor was a magnetic multilayer. This device showed similar results to before, though the magnetic response was stronger, possibly due to the reduced resistance in the switch arms.

This range of tests eliminated the most likely sources of artefacts, and gave confidence that the THz GMR effects (both normal and inverse) measured are real.

4.6.2 Demagnetisation?

As discussed in Chapter 2, ultrafast demagnetisation of magnetic metals has been demonstrated at both THz and optical frequencies. Examining the transmission results seen in figure 4.8b, the first three picoseconds look like a demagnetisation effect as the magnetic response gradually decreases to zero. However, the iGMR that appears after five picoseconds, as well as the input pulse response, is not easily explained. This does not exclude demagnetisation as a mechanism for the reduction in magnetic response, but does mean the explanation cannot finish there.

To test whether this was a demagnetisation effect, a three optical pulse setup was used to generate two THz pulses (referred to as pulse 1 and pulse 2 henceforth). Here all three switches were used, with two being used to excite the two THz pulses, and the last used for detection as shown in figure 4.10. The optical probe pulse path and pulse 2 were fixed in position so that the peak of pulse 2 was continuously measured. If the external magnetic field was then swept back and forth, a magnetic response was measured for pulse 2 consistent with a transmitted THz pulse.

The optical beam path for pulse 1 was dependent on a mechanical delay stage, allowing the arrival time of pulse 1 relative to pulse 2 to be controlled. Pulse 1 initially started by arriving after pulse 2, but was then swept through pulse 2, with the magnetic response of pulse 2 measured for each position. If demagnetisation was occurring, then when pulse 1 led pulse 2, the magnetic response of pulse 2 should disappear, since the CPW would have been demagnetised by the leading pulse. However, no change in the magnetic response (as a percentage) was noted as pulse 1 was swept through pulse 2. This indicates that demagnetisation is not responsible for the observed results.

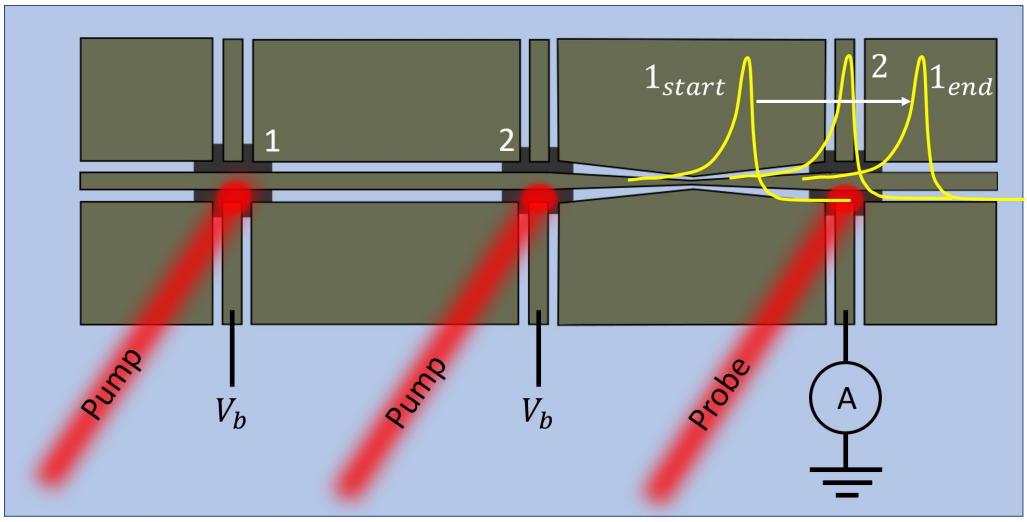

Figure 4.10: The setup used to test whether demagnetisation was occurring in the waveguide as a result of a transmitted THz pulse. The two switches on the left (labelled 1 and 2) were used to excite THz pulses. The switch on the right was used for detection, and the optical path lengths were adjusted so that the detection switch would continuously measure the peak of the THz pulse generated by switch 2. The pump beam length focused on switch 1 was set up with a mechanical delay line so that the THz pulse generated by switch 1 could arrive before or after the THz pulse from switch 2. The figure is not to scale.

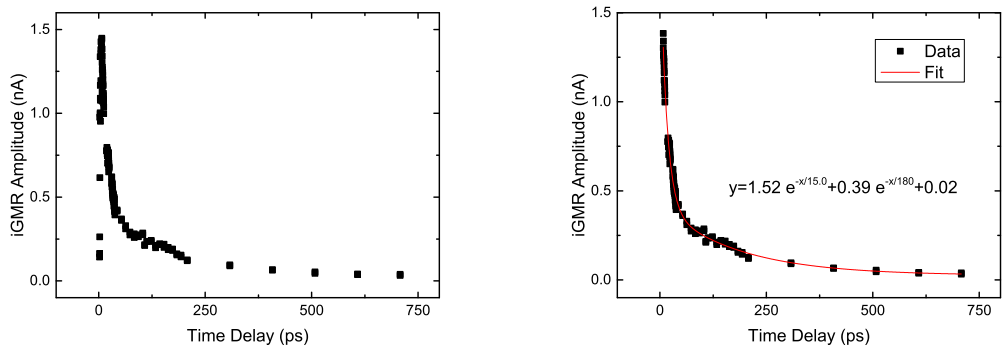

(a) (b)

Figure 4.11: a) The iGMR response of an input THz pulse over a long time delay window, where the data corresponding to reflection points has been removed. b) Isolating the iGMR pulse tail after excitation allows the data to be fitted with a decaying exponential function .

4.6.3 Spin Accumulation?

Measurements were also performed over a long time delay (approximately 700 ps) after the input THz pulse peak to investigate the duration of the iGMR signal. The iGMR effect persisted for the entire range of the delay stage used, though it did decrease in magnitude. Data for a long scan is shown in figure 4.11a , and the tail of this iGMR 'pulse' could be fitted with double exponential decay function shown in figure 4.11b. The fit function took the form of $y = 1.52e^{-x/15.0} + 0.39e^{-x/180} + 0.02$. Here, what is most notable is the timescale of the first exponential decay parameter, which is (15.0 ± 0.7) ps, corresponding well to a previously measured spin relaxation time in four nines copper [40], which at room temperature, was found to be (16 ± 4) ps.

Spin relaxation is a parameter that defines how quickly spin accumulation 'relaxes' back to equilibrium conditions. Since the decay of the iGMR pulse matches this known parameter, there is a possibility that the iGMR effect is caused by spin accumulation in the copper.

As introduced in Chapter 2, spin accumulation occurs when a current is driven from a ferromagnetic metal (FM) into a non-magnetic metal (NM). The current in the ferromagnet is spin polarised, so there is an over-abundance of one type of spin carrier

that accumulates at the FM/NM interface. In CPW devices, the majority of the current flow is in-plane, and therefore parallel to the orientation of the multilayer structure. In general, this would not be expected to produce spin accumulation. However, the electric field does penetrate into the metal according to the skin depth, and therefore there is an electric field perpendicular to the multilayer structure. Additionally, the oscillatory exchange interaction requires there to be some degree of spin effects occurring in NM spacer layers.

Therefore, it will be assumed that the THz pulse does drive a spin current into the copper spacer layer and that spin does accumulate in that layer. Given that starting point, the question that then needs to be asked is: 'can spin accumulation explain the iGMR effect?'. To answer that question, we will first consider short timescale paramagnetism. Figure 4.12 illustrates the density of states of a paramagnet when an external magnetic field is instantaneously applied and then removed after giving enough time for a quasi-equilibrium to be reached. In a paramagnet, there is no spin splitting, and the up and down spin bands are equally filled, sharing a common fermi level. When a magnetic field (H) is applied, spins opposed to the field gain an energy of $\mu_0\mu_B H$, and spins parallel to the field lose an energy of $\mu_0\mu_B H$, where μ_B is the Bohr magneton. This is an out of equilibrium condition, and normally it is assumed that a transfer of spins from high to low energy states occurs instantaneously, so that up and down spins share a common fermi level, and a small net magnetisation is induced by the uneven spin populations. However, this transfer of spins is not instant, but rather occurs on the timescale of the spin relaxation time, ie. picoseconds. Additionally, conservation of energy demands that as a spin flips from a high energy antiparallel state to a low energy parallel state, that this energy ($2\mu_0\mu_B H$) is released in some form. This is a similar mechanism to that of electron-hole pair recombination in semiconductors, and the energy could be released via emission of phonons or photons.

Once a quasi-equilibrium has been reached, if the field is then removed, the same energy difference will appear, but in the inverse direction. Electrons that were parallel to the field now have a higher energy to those that were antiparallel. The density of states now looks very similar to that induced by spin accumulation. With no more external influence, high energy spins will relax to lower energy states, reaching equi-

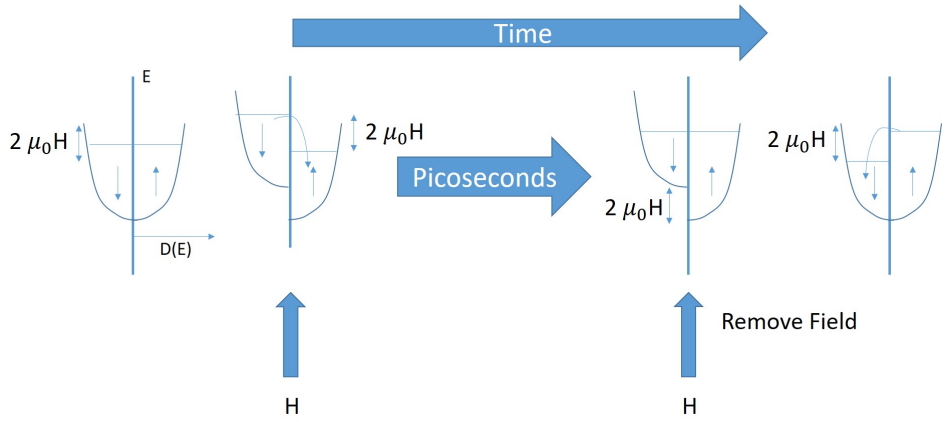

Figure 4.12: Here a paramagnetic is considered as a magnetic field is applied, and then removed. The density of states is similar to that shown on the left. If an instantaneous magnetic field is applied, then spins parallel to the field have a lower energy than spins antiparallel to the field, with the energy difference being $\mu_0\mu_B H$. This will cause a flow of high energy spins into lower energy spin states, with the timescale being determined by the spin relaxation time. Eventually, a quasi equilibrium is reached, and the spin dependent fermi levels are the same. If the field is then removed, the resulting density of states is the same as that caused by spin accumulation. Again, there will be spin relaxation from high to low energy states until equilibrium is reached.

librium in the picosecond timescale. Therefore, a mechanism is found by which spin accumulation can result in photon emission in the picosecond timescale.

Next it must be considered how spin accumulation could result in the iGMR effect. To do this, a Co/Cu multilayer structure in both the ferromagnetic (FM) and antiferromagnetic orientation will be considered. Figure 4.13 shows the spin accumulation in the antiparallel and parallel configurations [51]. In the antiparallel configuration, the spin accumulation changes sign in the FM layer, but remains constant in the NM layer. In the parallel configuration, spin only accumulates at interfaces, and the sign changes in every layer. This means that there is more spin accumulation in the antiparallel configuration than in the parallel configuration. As discussed previously, conservation of energy demands that photons or phonons are generated as spins relax from high to low energy states. Therefore, it is possible that the increased spin accumulation in the antiparallel state is responsible for the iGMR response.

Since the timescale of the experimental data matches spin relaxation times in cop-

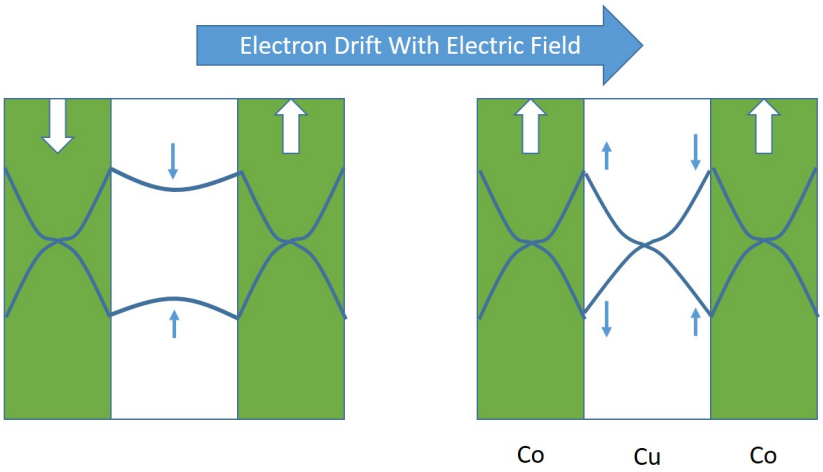

Figure 4.13: Spin accumulation in both the parallel (right) and antiparallel (left) states. In the antiparallel state, spin accumulation collects in the whole paramagnetic layer, while in the parallel state, the spin accumulation collects only at interfaces, and tends to zero in the middle of the paramagnet.

per, this idea provides quite a good qualitative argument. However, the energy difference needed to produce photons in the THz regime would be about 2 meV. However, in LSVs, typical energy differences measured would be in the order of 1 µeV [52]. Even allowing for very small switch separations of 10 nm, as is the case with the multilayer structures examined here, the energy difference observed in DC experiments is about three orders of magnitude too small if the same current flow is assumed. This gap has been reduced in some work [52], where voltages of 220 µV have been measured with efficient junctions and with large current densities. It is certainly possible that the current density induced by a THz pulse represents a larger current density than that used in LSVs, but more evidence would be needed before accepting this mechanism.

4.6.4 Scattering

As outlined in Chapter 2, it is spin dependent scattering that is responsible for GMR. Increased scattering in the high resistance state is responsible for the ordinary THz GMR by increasing the ohmic loss that affects the transmitted pulse. This energy is generally lost through phonon excitation (ie. heat). However, if some portion of this

energy could reflect back down the CPW, this would explain the iGMR nicely, since the larger scattering rate of the high resistance state would then result in a larger quantity of 'reflected' signal.

There is a variety of data that supports this premise, which will now be explored.

Different Input Pulses

An input pulse is generated when a single switch pair is used to measure a THz pulse. That is, one switch arm is used to excite a pulse, and the other switch arm is used to detect the pulse. The gap between the two switch arms is 50 µm, so the pulse is detected quasi-instantly, and before it has been transmitted down the waveguide. Given this measurement method, it would not be unreasonable to suppose that every input pulse from a given LT-GaAs wafer, and for a specific waveguide geometry, would be identical.

However, this is not the case, with extremely different input pulses measured as the metallisation of the waveguide is changed. This is shown in figure 4.14a for one CPW with 130 nm of copper and one with twenty layers of Co/Cu [3.4 nm/1.1 nm]. What is interesting here is that the rising edge of the two pulses is nearly identical, while the falling edge is extremely different. The falling edge is generally associated with the recombination time of electron-hole pairs in the PC switch. However, in this case, since the same LT-GaAs wafer was used for both devices, it is evident that there are additional effects at work.

This data makes sense if scattering can reflect a portion of the THz pulse. In the Cu waveguide, there is only one metal layer, which is highly conductive, with little loss, and the falling edge of the THz pulse rapidly tends to zero. In this case it is possible that the recombination time of the LT-GaAs switch is the dominant parameter. However, in the GMR waveguide, a large part of the metal is Co, which has a higher resistance than Cu (and hence more scattering) and also has multiple interfaces, all of which would contribute to a higher resistance. In this case, the falling edge does not tend to zero, and there is a sizeable current measured tens of picoseconds away from the main THz peak, enough to partially mask the reflection from the neighbouring switch pair.

If it is approximated that the Cu waveguide represents the zero scattering case

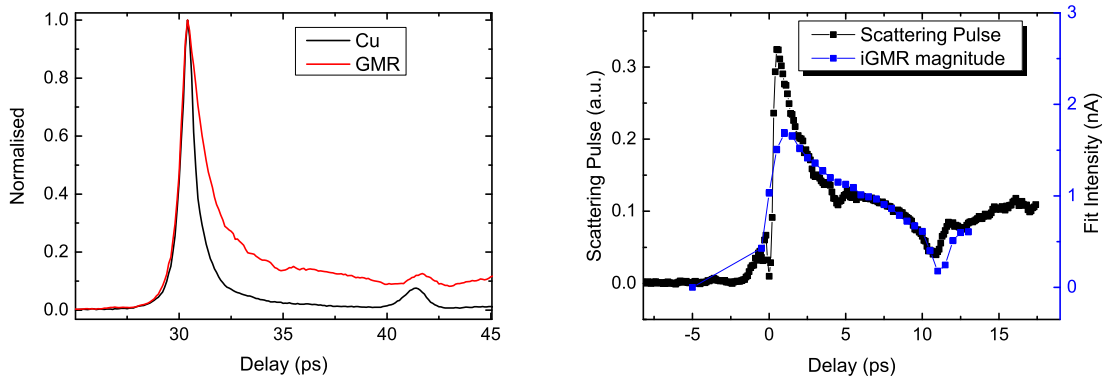

(a) (b)

Figure 4.14: a) Input pulses for two different CPWs with identical geometry, but different metallisation. (Black: Cu 130 nm, Red:Co/Cu multilayer ×20). b) The scattering pulse compared with the magnitude of the iGMR response for the input pulse of a GMR CPW. An extra point has been added for the iGMR response at −5 ps for easier comparison of the two traces.

(perfect conductor), then the scattering contribution to the THz pulse in the GMR waveguide can be isolated. This can be represented simply by using 'pulse arithmetic': $P_{GMR} - P_{Cu} = P_{scattering}$, where P_{GMR}, P_{Cu}, and $P_{scattering}$ represent the input pulse for the GMR CPW, Cu CPW, and a new term called scattering pulse, respectively. The scattering pulse represents the part of the THz pulse that is generated from the metallic properties of the waveguide. This will be shown and discussed further in the following section.

iGMR and the scattering pulse

Having started with the premise that scattering can induce THz reflections, it has then been shown that this can help to explain differences in input pulse shapes for different CPW metallisations. The question that then needs to be asked is, how does the reflection pulse compare with the iGMR effect? If the original premise is correct, then these two quantities are derived from the same mechanism. The iGMR magnitude for a GMR CPW input pulse is compared to the reflection pulse for that CPW in figure 4.14b. The similarity of the two traces is obvious, with the identical rise times being

especially notable. The two traces were derived using totally different methods, with the scattering pulse being calculated using 'pulse arithmetic' with the Cu and GMR input pulses, and the iGMR response being measured directly using magnetic field sweeps. The fact that they are so similar reinforces the proposed premise, that scattering can induce THz reflections.

Tapered Waveguides

As will be discussed more fully in Chapter 5, CPWs were made with three switch pairs, and a section of CPW that tapered to a centre conductor width of 5 µm, as well as a section of CPW that remained straight. The taper in the waveguide resulted in field concentration, and increased the measured GMR of a transmitted pulse (discussed in Chapter 5) due to increased ohmic loss. What will be discussed here is the effect of the tapered region on an input pulse. Four input pulses are shown in figure 4.15a, two from the Cu CPW previously mentioned, and two from a GMR waveguide with twenty Co/Cu layers. For each CPW, an input pulse next to a straight waveguide is shown and an input pulse next to a tapered waveguide is also shown. For both CPWs the input pulse measured next to the tapered section shows an extra hump off of the main pulse. The natural conclusion is that the tapered section of the track induces a reflection due to an impedance mismatch.

However, there are two points that suggest that this conclusion is incorrect. In the first place, the tapered region retains the same centre track to gap ratio along its length, and smoothly tapers without any abrupt changes. There is no obvious location along the tapered region where an impedance mismatch would occur.

The second reason comes from the magnetic response of the 'hump' region. As pointed out in figure 4.9b, where the magnetic response of the input pulse for a straight CPW is examined, the reflection from the neighbouring switch pair shows a normal GMR response. However, the 'hump' region shows an inverse GMR response, suggesting that its causual mechanism is different. This is shown in figure 4.15b, where the iGMR is very similar for the input and tapered region for the first 5 ps, despite very different input pulses. The difference after 11 ps is likely due to the tapered region highly attenuating reflections from the neighbouring switch pair.

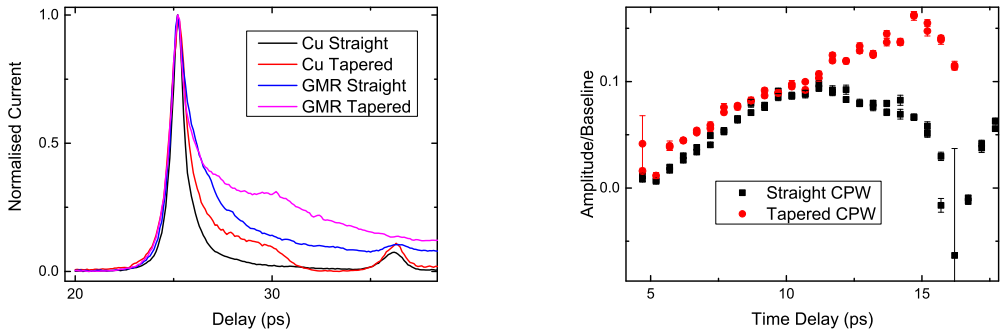

(a) (b)

Figure 4.15: a) The input pulse for a Cu and GMR waveguide next to both a straight and tapered section of CPW. The input pulses next to a tapered waveguide exhibit a 'hump' on the main pulse. b) The magnetic response of the GMR waveguide for both a straight and tapered region is very similar for the first five picoseconds, despite the different pulse shapes. The large error at 16 ps derives from the lack of clear signal for the python code to fit a Lorentzian to.

The fact that the tapered region induces a reflection that does not appear to derive from an impedance mismatch supports the theory that the pulse tail is due to reflections from the metallic properties of the waveguide. However, since the dimensions of the tapered region are still much larger than the mean free path of electrons in copper, the scattering occurrence remains constant in the tapered region, while it is the net drift velocity of the electrons that will change with field. Since the scattering does not change, but the taper still induces a reflection, it is then necessary to find a different, or more complete source of the 'scattering' pulse.

Some additional insight can be gained by an examination of the 'hump', since it is an obvious feature that appears to link with the iGMR data. Voltage sweeps were performed for an input pulse, and the current of the pulse peak is plotted against the amplitude of the 'hump' shoulder. This is shown in figure 4.16a. While there is certainly a non-linear component at higher current amplitudes, for low current amplitudes, the relationship can be well approximated as linear. Since ohmic loss is proportional to current squared, it is then clear that the reflected pulse does not derive directly from the ohmic loss.

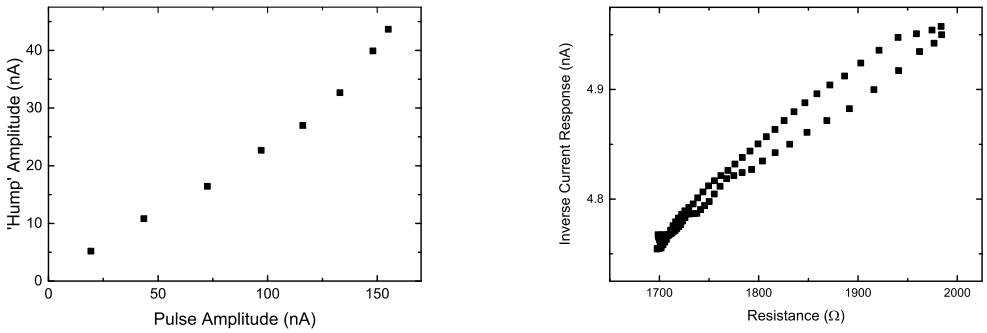

(a) (b)

Figure 4.16: a) The hump amplitude plotted against the THz peak pulse amplitude, and b) the current measured in the input pulse tail plotted against the DC resistance.

The iGMR current response can also be compared to the DC magnetoresistance curve. In figure 4.16b, the current from an input pulse tail is compared to the DC resistance. Again, the result is imperfect, and contains hysteretic effects, but the result is still close to linear. Given these two results, that the iGMR current can be approximated as proportional to the current and the resistance, we can use Ohm's law, $E = \rho J$, to say that the reflected pulse is proportional to the electric field.

THz Emitters?

As mentioned in Chapter 2 [30], the right combination of magnetic multilayers can result in the emission of THz radiation when illuminated by an optical pulse. In short, the optical pulse excites hot electrons, resulting in an spin polarised current that passes into the neighbouring NM metal. Here the inverse spin Hall effect results in a charge current pulse which emits at THz frequencies. This mechanism needs to be considered as a possible mechanism for the iGMR results. In figure 4.17, the GMR multilayer is shown in an antiparallel configuration. For a trilayer, the opposite magnetisation of the two ferromagnetic regions would result in a net charge current in the NM layer. However, for a multilayer with two or more NM regions, each neighbouring NM layer will have an opposing charge current, and therefore and THz emission from this source is likely to cancel out.

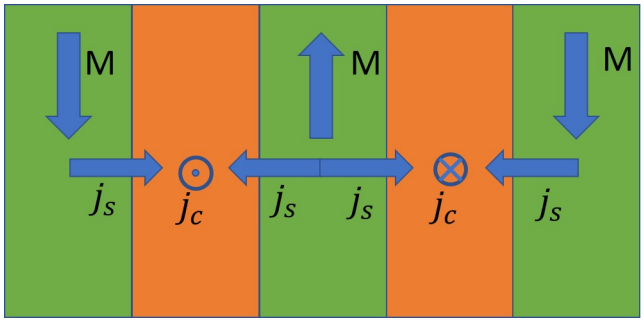

Figure 4.17: A GMR multilayer in an antiparallel configuration. If hot electrons are excited by an optical or THz pulse, a spin polarised current will flow from the FM regions into the NM regions, resulting in a charge current due to the inverse spin Hall effect. However, for two or more NM layers, the charge current contributions will cancel.

Scattering summary

This reflection from scattering idea provides the best explanation for experimental results. However, the mechanism by which this would occur is not clear. However, some general statements can be made. First, it has been determined that the shape of an input pulse tail is affected by the metal of the waveguide. A higher resistance metal will give a large pulse tail, and the change in scattering parameters induced by a change in external magnetic field will change the measured current in the input pulse of a GMR CPW. Tapering the waveguide will concentrate the electric field, and this too will increase the reflection amplitude. A firmer theoretical inquiry will be needed to pursue this topic further.

4.7 AMR Waveguides

CPWs with the same three switch pair geometry as the GMR CPWs were then made out of a single 100 nm thick layer of Co (used instead of Py since growth calibrations well known from GMR study). Transmission and input pulses were measured in the tapered region, and as in section 4.2, it was attempted to distinguish a THz AMR response. Thanks to LabVIEW automation, and possibly also to the increased confinement in the 5 µm tapered region, a magnetic response could be measured. This was difficult to do, since small errors in laser alignment would eliminate the signal, and even when

aligned, 1000 field sweeps were necessary to reduce noise to a sufficient level.

Magnetic responses for a transmission pulse and an input pulse are shown in figure 4.18. The data from the transmitted pulse (figure 4.18a) was taken from the peak position, and the data from the input pulse (figure 4.18b) was taken 4 ps after the THz peak position. Both measurements were taken with the external magnetic field perpendicular to the current direction, and in-plane with the sample.

Measurements were also performed after the THz pulse peak in transmission mode, and at the THz pulse peak for an input pulse. The device was also rotated so that the external magnetic field was parallel to the current direction. For all of these measurements, no magnetic response was measured. However, it is not certain whether this is because it does not exist, because alignment was not perfect, or if it is because the signal is too small to resolve. Therefore, no statements will be made about the absence of a signal, but the focus will stay on the measurable response.

Due to the difficulty of measurement, it was not possible to consistently track the AMR response for different time delays, but measurements at single positions could be taken. As with THz GMR measurements, an 'inverse' response (iAMR) is seen for the input pulse. The mechanism for this iAMR is not necessarily the same as for the GMR CPWs, but if it is, then the spin accumulation theory must be discarded, since this would not be possible in a single layer of Co.

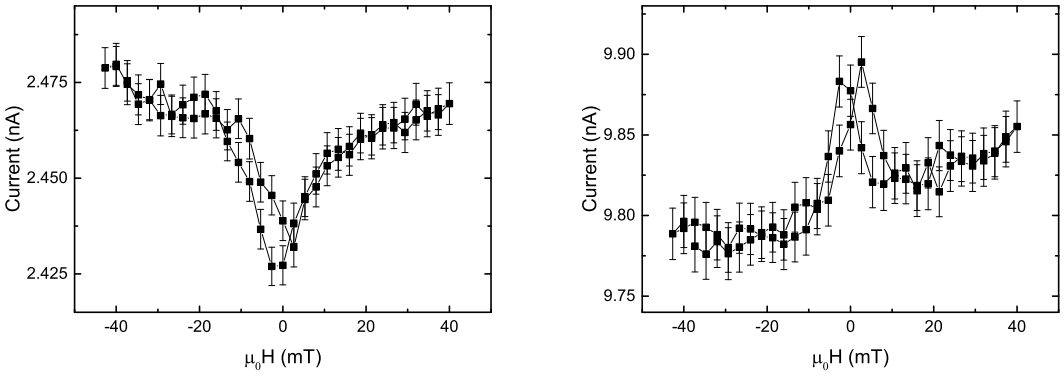

(a) (b)

Figure 4.18: a) The AMR response of a transmitted THz pulse, and b) and 'inverse' AMR response measured after the peak position of an input pulse.

4.8 General Discussion

THz GMR and AMR responses have been measured in metallic waveguides. In both cases, measurements made at the peak of a transmitted THz pulse have shown Ohmic behaviour, while measurements made after an input pulse have shown an inverse behaviour. In general terms, a number of statements can be made.

First, the leading part of a transmitted pulse behaves as expected from Ohm's law. This makes sense given that momentum scattering times are generally 10 to 100 fs [53]. This timescale is shorter than the resolution of our experiment, so normal resistive effects should occur quasi-instantly.

Second, the pulse tail for both transmitted and input pulses show an inverse response (iR). This iR is reduced at points where an ordinary reflection occurs, and interference effects are seen in transition regions. This suggests that the iR competes with the Ohmic response, and that they are not the same effect, as would be the case if demagnetisation was the mechanism.

Third, looking at input pulses in GMR CPWs shows that the peak magnetic response scales with, and occurs about 2 ps after, the THz pulse peak. From this it would appear that the iGMR is derived from the THz pulse. Stated another way, the THz pulse excites the iGMR response.

The iGMR 'pulse tail', shown in figure 4.11b has a time constant that matches spin relaxation times in Cu. This points to a spin accumulation mechanism. However an examination of the energies required to emit THz photons as well as the iAMR data reduces this possibility. It is also possible that both a spin accumulation and scattering mechanism are at play. However, with the current device geometry, it would be difficult to uncouple the two.

Of all the explanations for the iR mentioned, the scattering idea explains the experimental results best. However, the mechanism by which this would occur is speculative, and would need a firmer theoretical basis before adoption.

4.8.1 Future Work

Further experiments might be performed to gain a better understanding of the physics at play. The most advantageous would be to add the functionality of time resolved magneto optic Kerr effect (TR-MOKE) measurements. This would require excellent linear polarisers and photodetectors, but it might be possible to use the existing reflected probe laser pulse for this purpose. Adding TR-MOKE capability would give access to a more direct measurement of the CPW's magnetisation, supplying a greater insight into the effect of the THz pulse.

It would also be useful to gain more THz AMR data, similar to what was measured in GMR CPWs. To allow this, the THz measurement set up would have to be optimised for small signals. This might be done by using two lock in amplifiers; one synced with the optical chopper, and the other with the external electromagnet. Better electrical shielding might also enable these measurements, though this would likely require elaborate wire bonding arrangements.

4.9 Chapter Summary

Using waveguides made from magnetic metals, a THz magnetic response has been measured. Transmitted pulses behave as expected from Ohm's law, but the pulse tail shows an unexpected inverse behaviour. This has been examined in some detail, but the mechanism has not been determined. From these measurements, the potential of CPWs

for the investigation of high frequency magnetic effects has been shown. However, it is difficult to differentiate between the charge and spin responses in this geometry. Therefore, it was decided to combine on-chip THz waveguides with the LSV geometry.

Chapter 5

Tapered coplanar waveguides

5.1 Introduction

A necessary step on the road to THz lateral spin valves (THz LSVs) is the fabrication of THz waveguides with similar dimensions to DC LSVs. Most CPWs historically fabricated in-house have had centre conductor widths of 30 µm and the gap between the centre conductor and the neighbouring ground plane has been 10 µm. On the other hand, the critical dimensions of LSVs must be on the order of the spin diffusion length of the non-magnetic metal investigated, which in Cu is around one micrometer. This chapter describes the modelling and fabrication of CPWs which taper to these dimensions.

HFSS models successfully demonstrate transmission through CPWs with a centre conductor width of one micrometer and a gap size of 330 nm, additionally showing high field confinement and electric field concentration in the tapered region. This chapter describes devices that were fabricated using electron beam lithography (EBL) to define the narrow taper region and optical lithography to define the majority of the waveguide. THz pulse transmission has been demonstrated in these devices. Pulse confinement in the tapered waveguide was experimentally confirmed by fabricating a CPW with an U-bend. THz pulses were shown to propagate through the U-bend rather than straight across in a substrate or surface mode. Finally, tapered devices were made out of metal multilayers that demonstrated Giant Magnetoresistance. It was shown that the THz pulse response to change in conductivity was larger in tapered waveguides compared to straight CPWs. A mathematical framework is then developed to understand this confinement effect.

5.2 HFSS Modelling

Ansoft's HFSS [54] is a 'High Frequency Structural Simulator' that can be used to simulate the response of electronic systems at high frequencies. It uses the finite element method (FEM) to solve Maxwell's equations. Adaptive meshing is employed for this, in which the user's input geometry is discretised into a tessellating set of tetrahedral elements, with Maxwell's equations then solved for each element. The user creates a model of a device on the HFSS interface, defining input and output ports, excitation

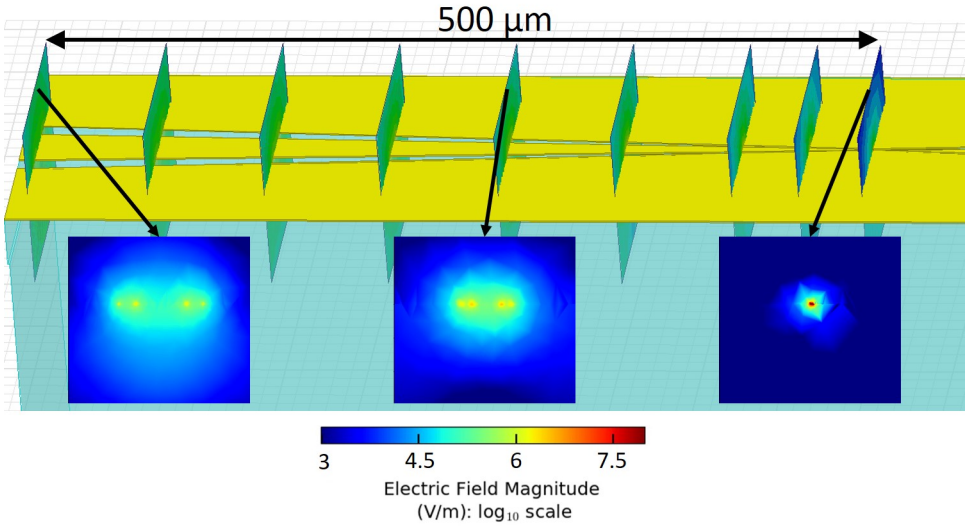

Figure 5.1: The HFSS model used for extracting field profiles. Figure taken from [55]

modes, the model boundary, as well as the range of frequencies to be tested. The simulation automatically inputs 1W of power at the input port. A range of results can then be obtained, including S parameters and field strengths. When running the simulation, HFSS starts with a tetrahedral mesh based on the geometry of the model, the mesh size typically being one quarter the maximum wavelength chosen. The model then calculates S parameters based on this geometry. Areas in the mesh that show large gradients in electric field are then sub-divided and the S parameters are recalculated. If the difference in results is less than a user specified value, the simulation finishes, otherwise, the mesh is further sub-divided and new results returned.

In order to understand field profiles for highly confined waveguides and to aid device design, HFSS was used to conduct simulations for a tapered coplanar waveguide structure. The centre track of the waveguide started at 30 µm, and linearly tapered down to a width of 1 µm (necessary size for LSVs) over a distance of $500\mu m$ (seen in figure (5.1)). The centre track to gap ratio was maintained at 3:1. Cross sections of the electric field were plotted at various points along the tapered CPW as shown in figure 5.1, and the electric field intensity profiles extracted.

Python code was used to analyse the profiles. The tetrahedral mesh of field values was linearly interpolated and converted to a 'picture' with a user defined number of

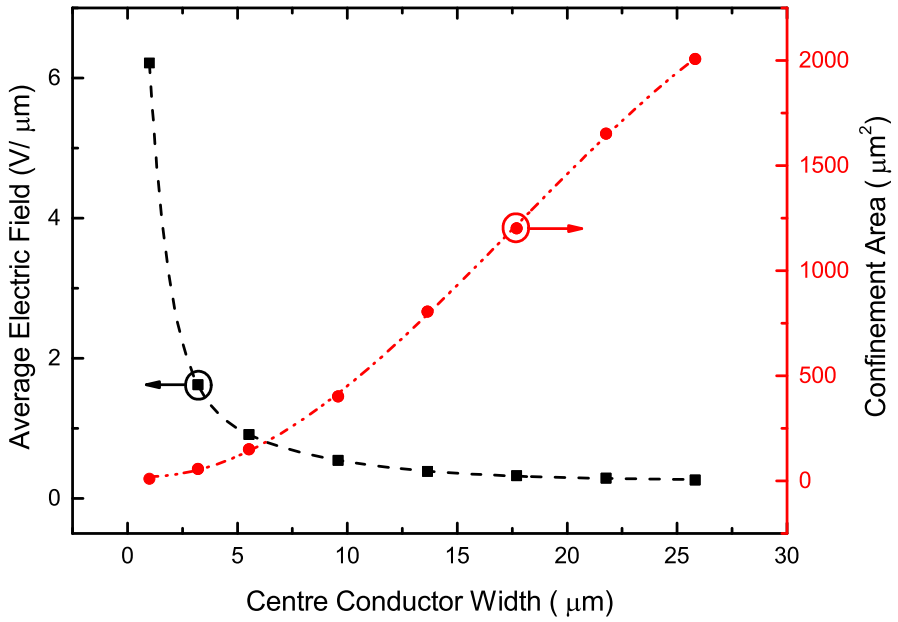

Figure 5.2: The confinement area and average field strength in that confinement area of each of the field distributions produced by HFSS are shown. It is clear that as the CPW width decreases, both the field confinement and the magnitude of the field confined increases. Dashed lines are included as guides to the eye. (figure taken from [55])

pixels representing field strengths. Pixels were roughly 40 by 40 nm, which was smaller than necessary for the majority of the waveguide, but needed for the extreme tapered region. The pixel with the maximum field strength was found, and the confinement area was defined as the number of pixels with a field strengths within an order of magnitude of that value. From this, both the confinement area and the average field strength within the confinement area was found.

The field profiles for different CPW widths were analysed and the confinement area and average field found. These are plotted against the centre conductor width in figure 5.2. It is clear that as the waveguide tapers, the confinement area is reduced, and the field intensity correspondingly increases.

The choice of substrate thickness in the HFSS model was not straightforward. Ini-

tially, 500 µm was used, as this is the thickness of the quartz wafers typically available commercially for device fabrication. However, substrate modes were excited in the model, masking the effects of the coplanar modes. While it is possible that these substrate modes are excited in real devices, they are not observable in experiment, and therefore it is desirable to remove them from the model results. Additionally, an examination of the waveport field profile suggests that the substrate modes were being excited at the waveport in 500 µm depth simulations, instead of the desired coplanar modes. This problem was overcome by reducing the substrate thickness to 40 µm in the simulation so that it could no longer support the substrate mode. This isolated the coplanar modes of interest. However, it also eliminated some degree of loss into the substrate, casting doubt on the accuracy of the field profiles obtained.

The best solution found to this problem was to reduce the substrate thickness at the waveport, but then increase the thickness to 500 µm ten micrometres away from the port. This meant that the model was forced to excite and detect the desired coplanar modes, but that the majority of the model reflected realistic experimental substrate thicknesses.

5.3 Ti/Au Device Fabrication

All devices used LT-GaAs as the photoconductive switch material. Using techniques outlined in Chapter 3 this was transferred to a quartz substrate prior to subsequent processing.

An entire piece of LT-GaAs (approximately 2 mm × 2 mm square) was typically left intact after transfer. EBL was then used to define a narrow taper region, and subsequent optical lithography then used to define the rest of the waveguide. In both cases Ti/Au was evaporated, with thicknesses of 5 nm and 100 nm for the EBL step, and 5 nm and 150 nm for the optical lithography step. Here, the difference in thickness was necessary to ensure a good overlap between the two layers. An example device is shown in figure 5.3 where the transition from optical lithography to EBL can be clearly seen. The dimensions of the waveguide were designed to be as close as possible to the theoretical model. However, the necessity of transitioning from an optical lithography

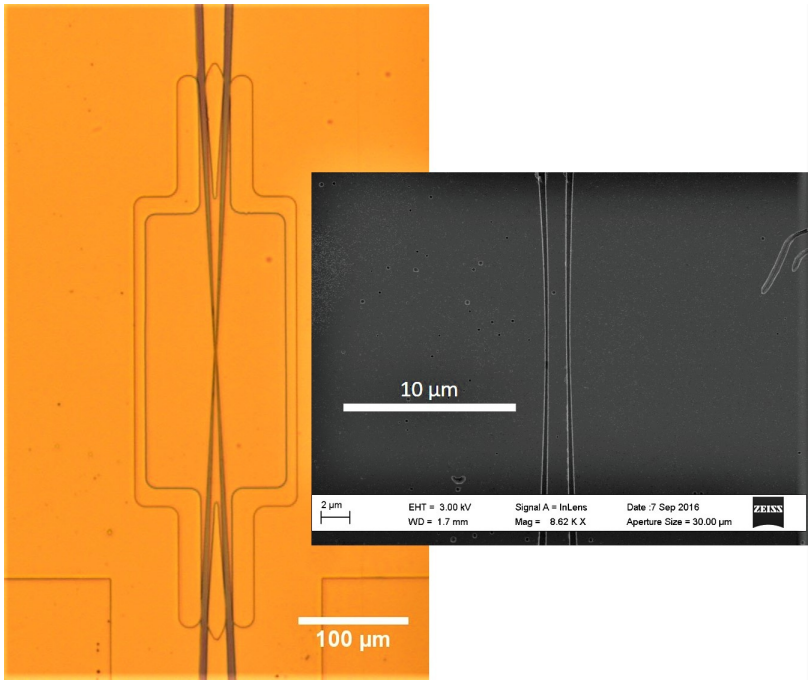

Figure 5.3: A optical and SEM image of a tapered CPW. The narrow region in the middle is defined with EBL, while the bulk of the device is defined with optical lithography methods.

layer to an EBL layer means that the overlap region will have two layers of Ti/Au, and any misalignment will result in deviations from the model design. Two devices with this geometry were made and tested.

5.4 Ti/Au Device Experiment

Since the entire piece of LT-GaAs was left intact, it was possible to track the pulse and subsequent reflections through the tapered region. This was achieved by generating a THz pulse between a biased pair of switches (position A in figure 5.4), and using the ground plane as the detection switch (position B in figure 5.4). In this setup, it was possible to measure the transmitted THz pulse at any point along the ground plane, with the exact position being determined by the location of the optical probe pulse.

Figure 5.5 shows how the transmitted pulse shape alters during propagation through the tapered region. Since any abrupt changes in the impedance of the CPW result in reflections from that point, this 'sliding switch' method highlights any imperfections in

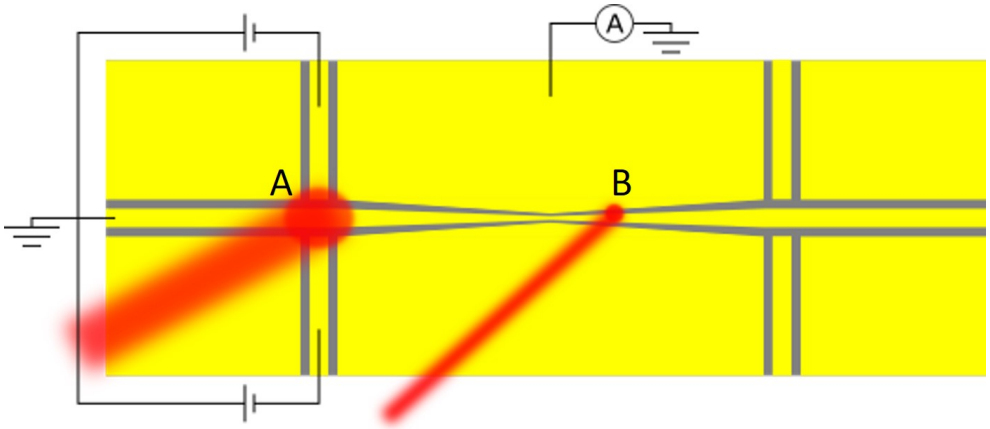

Figure 5.4: A schematic of the sliding switch method. A THz pulse with a coplanar mode is excited at a pair of switches (point A), and the current generated by the THz pulse is measured through a ground plane (point B).

the CPW that have an effect on the transmission of the THz pulse. Any impedance mismatches in the tapered region result in reflections that move towards the main pulse as it is transmitted along the CPW. Reflections that move in the same direction as the pulse are caused by impedance mismatches outside the tapered region of the waveguide. In this case there are two noticeable reflections that move in the same direction as the main pulse, one 7.2 ps in front of the main pulse, and another 18.3 ps in front of the main pulse. The first corresponds to the termination of the LT-GaAs sheet, while the second corresponds to the bond pad at the end of the waveguide track.

From figure 5.5 it can be concluded that the overlapping metallic regions between the optical and EBL layers are not responsible for any significant impedance mismatches; if they were, there would be two clear reflection points that would merge with the main pulse. As it is, there is only one major reflection that moves towards the main pulse. This corresponds to the position of the second switch pair.

When comparing the two devices fabricated, they both showed successful transmission through the tapered region. However, they gave quantitatively different amplitude results. In order to compare results between devices and with the HFSS model, the S21 parameter was calculated. This parameter measures the transmitted power between an input, reference amplitude, and the amplitude after transmission. To do this, a fast

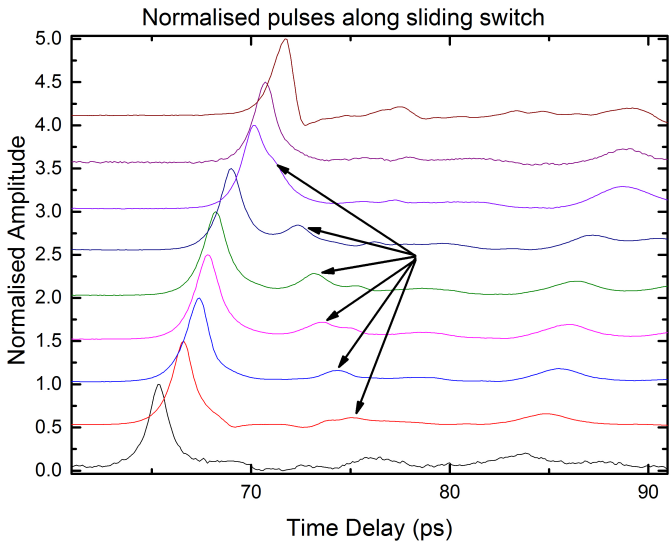

Figure 5.5: The normalised tranmission pulse shape on passing through the tapered region is shown. Reflection points in the tapered region can be clearly seen due to their movement relative to the main pulse. Arrows indicate the reflection from the neighbouring switch pair that merges with the main pulse.

fourier transform was used on each of the pulses measured and the frequency spectrum obtained. Amplitudes at 1 THz were used for calculations, and the first pulse measured along the CPW was taken as the input pulse. The S21 parameter was then calculated using

$$S21 = 20 \log \frac{A(x)}{A_{input}} \tag{5.1}$$

where $A(x)$ is the current amplitude at one terahertz at any given point along the waveguide, and A_{input} is the amplitude of the input pulse. This method was used to calculate transmitted power for both devices measured, the results of which are shown in figure 5.6 (a and b). In the first device, the functional form is very similar to that predicted by HFSS, but the amplitude finishes significantly lower. In the second device, the data corresponds to that predicted by HFSS in sections of the waveguide, but there are also sections where the amplitude is significantly smaller than expected. IV sweeps were also performed alongside the THz scans, and these were used to calculate the resistance at the measurement position. In the same locations that measured smaller amplitude THz pulses, larger resistances were also measured. These data points are indicated by shaded regions in figure 5.6 (b and c). The combination of small amplitude THz scans and high resistance values suggests that the behaviour of the LT-GaAs is not uniform along the device.

Due to these results, as well as previous observations in other devices, it was decided to discount absolute amplitude values. While this means that amplitude values could not be safely compared to the HFSS model, these results still clearly show that THz pulses can be transmitted through waveguides at the same scale as lateral spin valves. Additionally, the lack of major reflections suggests that the tapering process and the necessary metallic overlap between optical and e-beam defined layers does not attenuate the main pulse by a prohibitive amount.

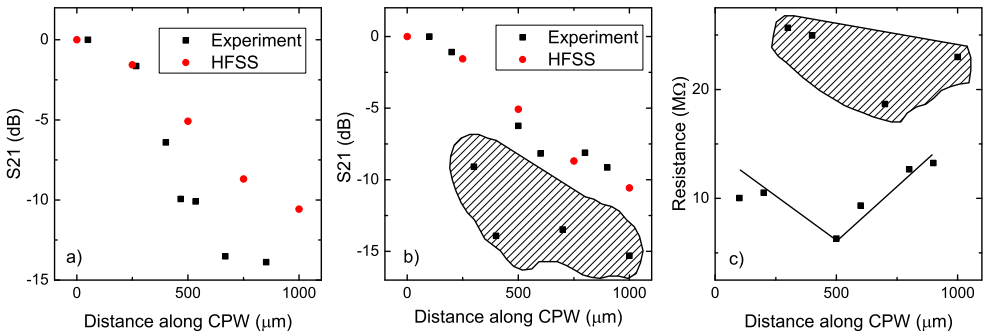

Figure 5.6: a) Transmitted power for the first device measured, where the functional form matches the HFSS model well, but the amplitude is significantly lower, and b) transmitted power for the second device measured, where the data matches well in certain areas, but not in the shaded region. c) IV scans were used to measure the resistance of each of the measurement regions. The regions that showed inconsistent THz pulse measurements correspond to regions of high resistance. The resistance trend expected from geometrical considerations is drawn onto the graph.

5.5 Curved Waveguides

As confirmation that the THz pulse is concentrated in the area of the waveguide and not just loosely coupled in a surface wave or substrate mode, a waveguide with an extra U-bend was fabricated (figure 5.7a). The U-bend was large enough to delay the THz pulse by approximately 700 fs assuming similar pulse velocities to those previously measured, and the LT-GaAs under the waveguide was left intact so that the pulse's progress could be tracked through the waveguide.

The device was mounted on a micrometer controlled variable height stage, and this was used to measure the THz pulse at one hundred micrometer increments as it progressed along the waveguide. To do this, the device was set up so that both the pump and the probe optical beams were aligned on the same switch pair. The stage was then moved by 100 µm, and the pump and probe beams realigned. When aligning the probe beam, only the horizontal degree of freedom on the aligning mirror was used, meaning that vertical distance between the excitation switch pair and the measurement position was controlled only by the distance that the stage had been moved.

The peak position of the transmitted THz pulse was measured as a function of

stage height as shown in figure 5.7b, and there is a clear jump in peak position around the middle of the waveguide where the U-bend is situated. This corresponds to what would be expected if the transmitted pulse was forced through the U-bend, confirming good pulse confinement in the CPW. This conclusion was supported by HFSS models sharing the same geometry.

For a constant pulse velocity in the extra loop, the largest discontinuity in peak position that could be expected was approximately 700 fs. However, the change in the time delay was found to be (1.0 ± 0.1) ps. This is due to a change in effective permittivity as the dimensions of the waveguide are reduced. With a CPW gap size of 10 µm, the 350 nm of LT-GaAs has little influence on the effective permittivity. However, as the gap is reduced to 330 nm, the effective permittivity changes from that of quartz to that of the LT-GaAs sheet. This was tested in HFSS, by modelling a CPW with a centre width of 30 µm and a CPW with a centre width of 1 µm. It was found that the effective permittivity increased from 2.6 (30 µm) to 5.5 (1 µm). Given that velocity is inversely proportional to the square root of the permittivity, we get $\frac{v_{30}}{v_1} = \frac{\sqrt{\epsilon_1}}{\sqrt{\epsilon_{30}}}$. This is equal, within the uncertainty to the experimentally measured pulse delay from transmission through the U-bend, which was $1/0.7 = 1.4 \pm 0.1$. This is also an effective demonstration of pulse confinement, since the 350 nm thick layer of GaAs has such an influence on the propagation velocity.

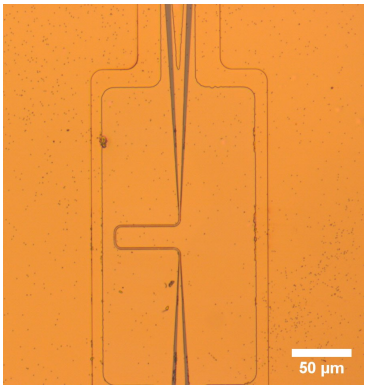

(a)

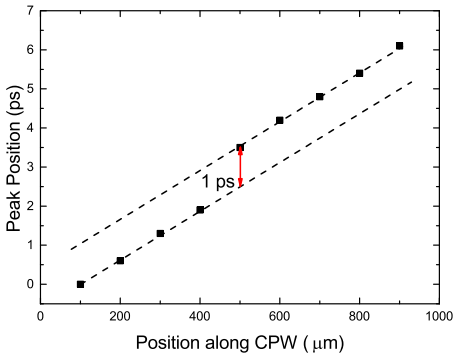

(b)

Figure 5.7: 5.7a) A tapered CPW with an U-bend. 5.7b) The THz peak position plotted against the laser probe pulse z position on the CPW. The change in peak position at the centre is clearly visible.(figure taken from [55])

5.6 GMR Waveguides

To test the field concentration effects of tapered CPWs, devices were made with GMR metallisation, and both tapered and straight section of waveguide. These devices had three switch pairs, with a straight section of CPW between two and a tapered section between the other two as shown in figure 5.8a. Three devices were fabricated in the same growth run and using the same metallisation recipe, but with different degrees of tapering (centre track widths of 20 µm, 10 µm, and 5 µm).

Changing the DC resistance of the metal will change the ohmic losses or power dissipation in the waveguide, which means the transmitted pulse energy will vary with external magnetic field. However, the power dissipation is also dependent on the strength of the electric field in the vicinity of the metal. Because the electric field is concentrated in the tapered waveguide, it is expected that the change in pulse amplitude with external magnetic field will be greater for pulses transmitted through the tapered waveguide than for pulses transmitted through the untapered waveguide. This will be considered more rigorously later.

5.6.1 Experimental THz Pulse GMR Response

To measure the THz GMR response, devices were set up for transmission measurements as described in Chapter 3. A split coil electromagnet was positioned around the device so that an external magnetic field could be applied in plane with the device and perpendicular to the transmission direction. Transmitted pulses were measured for both the straight section of CPW and the tapered section of CPW, and measurements were made for different external magnetic field strengths. For both tapered and straight sections, a change in measured pulse amplitude was noted with a change in external magnetic field, with no corresponding change in pulse arrival time. The mechanical delay line for the probe laser beam was then fixed in place to measure the transmitted pulse peak continuously while the external field was swept back and forth between plus and minus 40 mT for a minimum of 100 field sweeps. This was done for transmitted pulses through the tapered section of the waveguide and the straight section of the waveguide, using the same switch arm in the middle for detection. It was noted that the GMR current response of the 5 µm taper was 2.4 ± 0.2 times that of the straight region. This is shown in figure 5.8b, and results of 1.3 ± 0.1 and 0.97 ± 0.08 were also found for the CPWs with tapers of 10 and 20 µm respectively.

5.6.2 Mathematical Framework

To understand the increased GMR response of the tapered waveguides, consider the electric field of the THz pulse E(x) as it is transmitted through the waveguide. This can be expressed as $E(x) = E_0 e^{-\alpha x}$ where α is the attenuation constant and E_0 is the electric field strength of an input pulse before transmission. When an external magnetic field is applied, the attenuation constant will change by an amount $\Delta\alpha$ due to the change in metal conductivity giving $E(x) = E_0 e^{-\alpha x - \Delta\alpha x}$.

In the tapered region, field confinement must also be taken into account, and the equation becomes $E(x) = E_0 e^{-\alpha x - \Delta\alpha x - c(x)x}(1 + E_C(x))$. Here $E_C(x)$ represents the increase in electric field near the metal in the waveguide as the dimensions of the waveguide are reduced. It is defined as being zero for the waveguide dimensions at the start and end of the CPW, which are the same (centre conductor width of 30 µm). The term c(x) represents the extra ohmic attenuation induced in the waveguide as a result

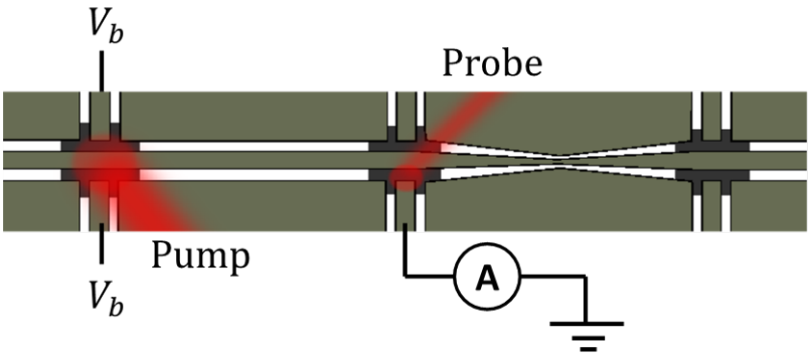

(a)

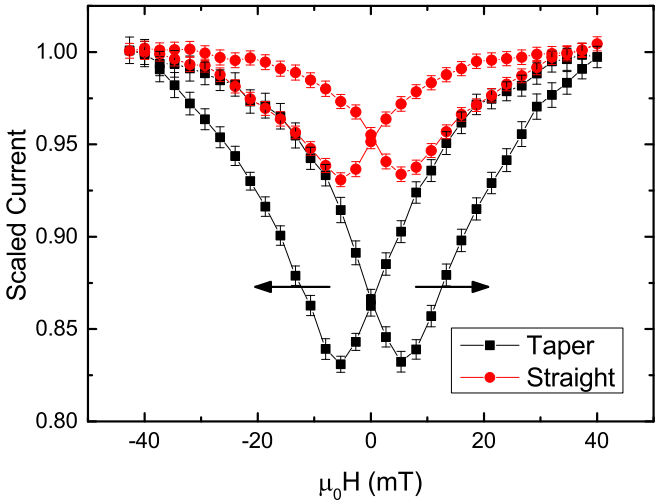

(b)

Figure 5.8: a) A schematic of a GMR CPW device. There are two sections of track, one straight and the other tapered, and three switch pairs that allow measurement of different transmission options. b) The scaled GMR current response in a transmitted pulse for both the straight section of CPW and the tapered section of CPW as the external field is changed. The magnetic field sweep direction is indicated with the arrows, and lines have been added as a guide to the eye.

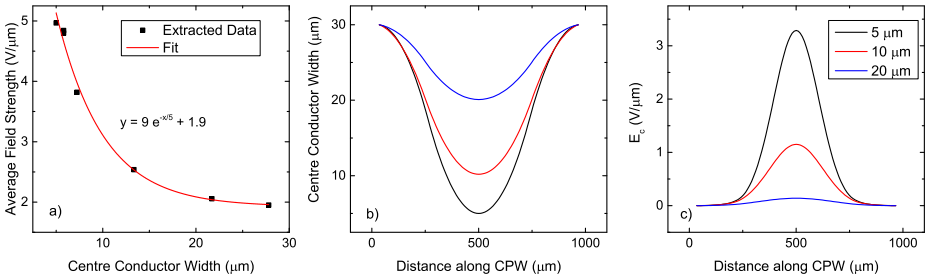

Figure 5.9: a) The new fit function relating field strength to centre conductor width. This is used with b) the extracted mask data about the centre conductor width along the CPW to calculate c) the expected field concentration E_C in the CPW.

of the tapering-induced field confinement. By adding these two terms to the equation, the field concentration in the tapered section of the waveguide is accounted for, and the only lasting effect of this concentration is the extra attenuation.

The term E_C can be found using HFSS. A new model was generated for this purpose. The geometry was the same as the 5 µm taper, but the metal was assumed to be a perfect conductor with no substrate. By using these (albeit unrealistic from an experimental perspective) conditions, it was possible to isolate concentration effects while eliminating ohmic and dielectric losses. The resulting field concentration dependence is shown in figure 5.9 (a). Using the field concentration dependence, as well as the geometry of the devices extracted from mask data (figure 5.9(b)), it was then possible to calculate $E_C(x)$ (figure 5.9(c)).

It is then necessary to consider the electric field interaction with the metal in the waveguide. When an electric field is incident on a metal, it penetrates by a distance in accordance with the skin depth of the metal which will be about 50 nm at one terahertz in copper. The electric field will drive a current in the metal, and this will induce a power dissipation per unit volume in keeping with $P = \frac{I^2 R}{AL}$, where A is cross-sectional area and L is length. This can be rewritten as $P = J^2/\sigma$ using the definition of current density $J = I/A$, and recalling the relationship between resistance and conductivity $R = L/(A\sigma)$. Using Ohm's law ($E = \sigma J$) this can then be written as $P = \sigma E^2$.

As the DC conductivity of the waveguide changes, the power dissipation will also change. For simplicity, only the maximum (σ_1) and minimum (σ_2) conductivities will

be considered. In the tapered waveguide, the maximum power dissipation is

$$P_{max} = \sigma_2(E_2 e^{-\alpha x - \Delta\alpha x - c(x)x}(1 + E_c(x)))^2 \tag{5.2}$$

and the minimum power dissipation is

$$P_{min} = \sigma_1(E_1 e^{-\alpha x - c(x)x}(1 + E_c(x)))^2. \tag{5.3}$$

The percentage change in power dissipation is $\%P = (P_{max} - P_{min})/P_{min}$. When the expanded versions of P_{max} and P_{min} are inserted into this equation, the majority of the terms cancel, giving

$$\%P = \frac{\sigma_2 E_2^2 e^{-2\Delta\alpha x} - \sigma_1 E_1^2}{\sigma_1 E_1^2}. \tag{5.4}$$

From experiments, it is known that the pulse amplitude of the input pulse changes very little with change in DC resistance (external magnetic field). Therefore, Ohm's law can be used to say $J_0 = \sigma_1 E_1 = \sigma_2 E_2$. The variables E_1 and E_2 can then be eliminated to give

$$\%P = \frac{\sigma_1 e^{-2\Delta\alpha x} - \sigma_2}{\sigma_2}. \tag{5.5}$$

So the percentage change in power dissipation is equal to the percentage change in conductivity, with a correction term that allows for the extra attenuation induced. The key thing to note is that although it was the tapered waveguide that was being considered here, neither of the two terms that describe the tapered waveguide ($E_c(x)$ and $c(x)$) are present.

Therefore we can describe the total change in power dissipation as $\%PP_{min}$ for both the tapered and untapered sections of waveguide. To calculate the total change it would be necessary to know many parameters including the conductivity, starting electric field, attenuation constant, and the two parameters describing the tapering effect. While some of these are easily measurable experimentally, others are hard or impossible with the limitations of this type of device. However, while it is not feasible to calculate the absolute change in power dissipation as the conductivity changes, it is possible to calculate the relative change in power dissipation between the tapered and straight waveguides, ie. $R_J = \Delta P_T/\Delta P_S$, where ΔP represents $\%PP_{min}$ and the T and S subscripts represent the tapered and straight waveguides respectively. As $\%P$

does not change with the waveguide geometry, it cancels out, and the ratio of power dissipation change, R_P, then simplifies to $P_{min,T}/P_{min,S}$.

The total power dissipation in the straight waveguide is then $\int_0^1 \sigma_1 E^2(x)dx = Avg(\sigma_1 E^2(x))$, where $Avg(E^2(x))$ is the mean value of the electric field squared. Using the mean value simplifies the problem, and the same method can be used for P_T. For the purposes of calculating power dissipation, the x dependence of $E_C(x)$ can be removed and be replaced with the mean value of $E_C(x)$ in the section of CPW. In this way we can obtain E_C and $E_{C,sq}^2$ where $E_C = \langle E_C(x)\rangle$ and $E_{C,sq}^2 = \langle E_C^2(x)\rangle$. Note here that $\sqrt{E_{C,sq}^2} \neq E_C$. Because power dissipation is responsible for the extra attenuation in the tapered region, it is also possible to express $c(x)$ as $k\sqrt{E_{C,sq}^2}$ where k is a term that represents the metal properties and thickness. For the experiment performed here, where three devices were grown from the same recipe, it can be considered a constant.

The ratio R_P then becomes

$$\frac{\langle e^{-2\alpha x} e^{k\sqrt{E_{C,sq}^2}}(1+E_C)^2\rangle}{\langle e^{-2\alpha x}\rangle}. \tag{5.6}$$

The term $e^{k\sqrt{E_{C,sq}^2}}$ is a constant and can be taken out of the average, and we approximate that the average of the products is the same as the product of the averages (ie. $\langle e^{-2\alpha x}(1+E_C)^2\rangle = \langle e^{-2\alpha x}\rangle\langle(1+E_C)^2\rangle$), allowing the ratio to become

$$R_P = \frac{e^{k\sqrt{E_{C,sq}^2}}\langle e^{-2\alpha x}\rangle\langle(1+E_C)^2\rangle}{\langle e^{-2\alpha x}\rangle} \tag{5.7}$$

where the attenuation term can now be cancelled out. Expanding the $(1+E_C)^2$ term then gives

$$R_P = e^{k\sqrt{E_{C,sq}^2}}(1+2E_C+E_{C,sq}^2) \tag{5.8}$$

where k is the only unknown variable. This represents the power dissipation ratio. However, experimentally, it is current that is being measured. Since $P \propto I^2$, the ratio of current change can be expressed by

$$R_J = \sqrt{R_P} = \sqrt{e^{k\sqrt{E_{C,sq}^2}}(1+2E_C+E_{C,sq}^2)}. \tag{5.9}$$

Solving numerically for a range of k values shows that for k=0.01, ratios of 2.2,1.4, and 1.06 for tapers of 5, 10 and 20 µm are calculated, comparing well with the experimental results of 2.4±0.2, 1.3±0.1, and 0.97±0.08.

5.7 Chapter Summary

THz pulse propagation has been theoretically modelled and experimentally demonstrated in waveguides on the scale of one micrometer. Pulse confinement to the waveguide has been confirmed, and HFSS simulations show field concentration in the confined regions. These results allow the possibility of THz excitation of LSVs. Additionally, the tapering of CPWs can be used as a tool to enhance field interactions with materials in close proximity to the waveguide. Finally, waveguides made from metal multilayers with GMR properties have been fabricated and tested. The current response with change in conductivity is higher in tapered waveguides than it is in straight waveguides due to the field concentration in the tapered region. A mathematical framework has been developed to describe this process. The results described in this chapter formed the basis for a journal paper [55] and were presented as a poster at IRMMW-THz 2017 [56].

Chapter 6

THz lateral spin valves

6.1 Chapter Overview

Having developed and tested CPWs that showed THz spin properties, it was attempted to fabricate LSVs capable of injecting and measuring spin accumulation at THz frequencies (THz-LSVs). This would allow a better isolation of spin and charge effects. To do this, two types of devices needed to be combined: on-chip THz waveguides, and DC LSVs. From a fabrication perspective, it was decided to use on-chip THz waveguides as the starting point, and adapt these until they could be merged with a LSV structure.

This chapter begins with a description of DC LSV design, fabrication procedure and measurement methods. It continues with some numerical modelling of expected results for picosecond spin injection, and HFSS modelling of potential THz-LSV designs. Finally, the recipe to fabricate THz-LSVs is described, and several debugging iterations outlined. Although this part of the project was ultimately not successful, progress was made, and potential methods to overcome the difficulties encountered are proposed.

6.2 DC LSV design and measurements

The fabrication recipe for DC LSVs was largely inherited from previous doctoral students. The author had no contribution to that work, and therefore, the recipe will only be briefly summarised. For a complete overview of DC LSV fabrication, the interested reader is directed to the PhD theses of Joseph Batley or Georgious Stephanou [40, 57].

The LSVs were grown on Si/SiO_2 (100 nm as purchased) substrates, and underwent rigorous chemical cleaning followed by oxygen plasma ashing. Three lithography and metallisation steps were then performed: normal EBL (figure 6.1(a)), optical (figure 6.1(b)), then 3D EBL (figure 6.1(c)). The normal EBL step defined the inner contacts, which were then metallised with Ebeam evaporation. This layer also included alignment markers for the two subsequent layers. Optical lithography and sputtering were used to define the outer contacts. The final step used the bilayer Ebeam resist and angled evaporation technique described in Chapter 3 to grow clean FM/NM junctions in one step without needing to break vacuum.

Devices were grown in three by three arrays, so nine devices were grown per chip, allowing small systematic changes to be made to the lithography pattern under the

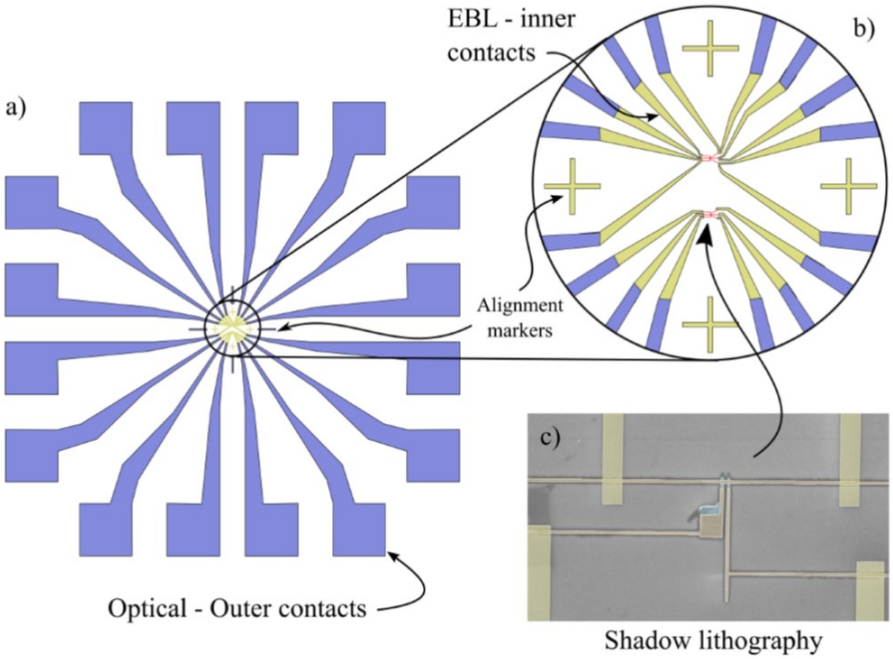

Figure 6.1: A schematic of the three lithography steps used in the fabrication of DC LSVs including a) outer contact, b) inner contacts, and c) the active device area. (figure taken from [40])

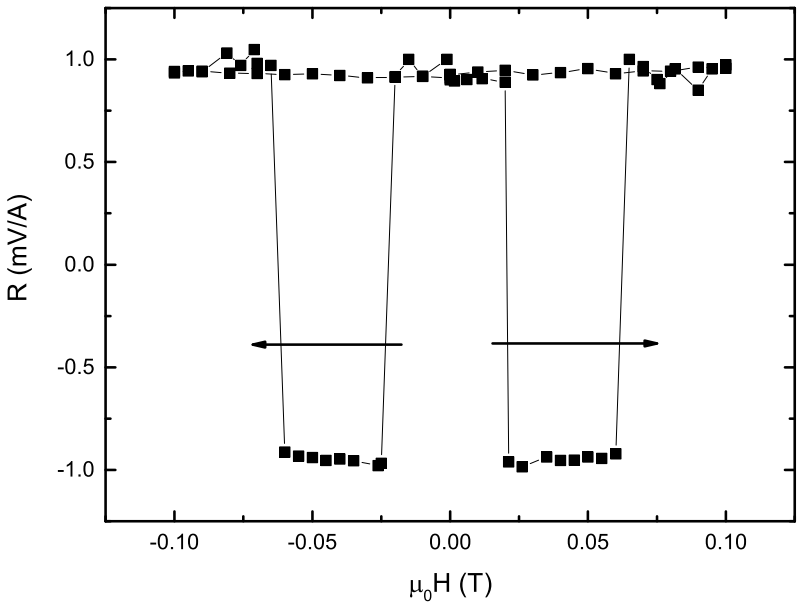

Figure 6.2: The non-local resistance of a DC LSV as an external magnetic field was swept back and forth. Lines are included as a guide to the eye, and arrows indicate the sweep direction.

same growth conditions. Typically, the distances between the ferromagnetic switches were altered, for example, as this allowed measurement of spin diffusion lengths.

Once fabricated, the chip was covered in PMMA resist as a protective coating, and then a wafer saw was used to divide the chip into the nine separate devices. The device to be tested was fixed to a sample holder with silver paint, ensuring that the direction of the FM switches was parallel to the direction that the magnetic field would be in. A wedge bonder was then used to connect the device to a PCB.

The sample holder was then attached to a sample stick, and inserted into a cryostat which allowed temperature control down to approximately 2 K. DC measurements shown in this section were then performed at 10 K.

Measurements were performed as described in Chapter 3, and some data is shown in figure 6.2. The magnitude of the resistance change as the ferromagnets switch from parallel to antiparallel is proportional to the spin accumulation at the interface [58]. By changing the temperature, the distance between ferromagnetic electrodes, and the

composition of the non-magnetic spacer wire a great deal of information about spin properties at interfaces and in a bulk paramagnet can be determined. It was hoped that by extending these measurements to the picosecond regime, that additional insight could be gained.

6.3 THz Spin Accumulation Modelling

In order to better understand the signal likely to be measured if spin was injected and detected in the picosecond regime, a one-dimensional model was created using Python code.

6.3.1 Mathematical Framework

In general, spin transport can be characterised by [38]

$$\vec{j}_\sigma = \sigma_\sigma \vec{E} - eD_\sigma \nabla \delta n_\sigma \tag{6.1}$$

where $\vec{j}_\sigma$ is the electric charge current density for spin channel σ ($\uparrow$ or $\downarrow$), $\vec{E}$ is the electric field, σ_σ is the spin dependent conductivity, e is electron charge, D_σ is the spin dependent diffusion constant, and δn_σ is the spin dependent carrier density deviation from equilibrium.

In a typical LSV setup, there is an electric field that drives a spin polarised current through the FM/NM interface, generating spin accumulation. However, there is no electric field in the section of NM metal between the two FM switches, which is the part of the device being investigated. Allowing $\vec{E} = 0$ then, and changing the definition of current from flow of charge to flow of electrons gives $\vec{j}_\sigma = D_\sigma \nabla \delta n_\sigma$. This is Fick's first law, and the problem is reduced to a diffusion problem.

Ordinarily, Fick's second law is then derived using the first law and conservation of mass, $\frac{\partial n}{\partial t} + \frac{\partial j}{\partial x} = 0$, where n is the quantity being diffused, and j is the current density of n. However, in the case being considered in a LSV, this form is incorrect, since the quantity being considered, δn_σ, is subject to spin relaxation, and is therefore not conserved, ie it is a transient response to the charge current. To overcome this issue, a limiting case is considered, where there is a uniform accumulation of spin over

the entire sample, ie. $\delta n_\sigma = constant$. In this example, $\frac{\partial \delta n_\sigma}{\partial x} = 0$ over the entire sample, and therefore $j = \frac{\partial j}{\partial x} = 0$. There is no net diffusion over the sample, and the spin accumulation is then reduced according to the spin relaxation time (τ_{sf}), that is, $\delta n_\sigma = \delta n_{(\sigma,0)} e^{-t/\tau_{sf}}$, where $\delta n_{(\sigma,0)}$ is the spin accumulation at $t = 0$. This means that the form for the conservation law can be calculated, $\frac{\partial \delta n_\sigma}{\partial t} + \frac{\partial j}{\partial x} = -\frac{\delta n_\sigma}{\tau_{sf}}$. Substituting in the definition of j_σ from Fick's first law gives

$$\frac{\partial \delta n_\sigma}{\partial t} + \frac{\partial^2 \delta n_\sigma}{\partial x^2} = -\frac{\delta n_\sigma}{\tau_{sf}}. \tag{6.2}$$

In order to model this, it must be discretised in space and time. A one dimensional line is considered for this purpose. On this line there are a number of discrete locations (m-1, m, m+1) separated by a distance Δx . Between each location there is a boundary (m-1/2, m+1/2). Values of δn_σ will be considered for integer values of m, and gradients will by considered at the boundary positions. The $\frac{\partial^2 \delta n_\sigma}{\partial x^2}$ term will be examined first. This can be expressed as

$$\frac{\frac{\partial \delta n_\sigma}{\partial x}|_{m+1/2} - \frac{\partial \delta n_\sigma}{\partial x}|_{m-1/2}}{\Delta x}, \tag{6.3}$$

and the differential terms can be expressed as

$$\frac{\partial \delta n_\sigma}{\partial x}|_{m+1/2} = \frac{\delta n_{(\sigma,m+1)} - \delta n_{(\sigma,m)}}{\Delta x} \tag{6.4}$$

and

$$\frac{\partial \delta n_\sigma}{\partial x}|_{m-1/2} = \frac{\delta n_{(\sigma,m)} - \delta n_{(\sigma,m-1)}}{\Delta x}. \tag{6.5}$$

Taking equations 6.4 and 6.5, and substituting them into 6.3 gives:

$$\frac{\delta n_{(\sigma,m+1)} + \delta n_{(\sigma,m-1)} - 2\delta n_{(\sigma,m)}}{(\Delta x)^2}. \tag{6.6}$$

A similar method can be used to treat the discretization of time. Here, it is assumed that $t = q\Delta t$ where t is the total time, q is an integer, and Δt is the time step. The term $\frac{\partial \delta n_\sigma}{\partial t}$ can then be expressed as $\frac{\delta n^{q+1}_{(\sigma,m)} - \delta n^q_{(\sigma,m)}}{\Delta t}$. If this, as well as equation 6.6 is substituted into equation 6.2, and the terms are rearranged, it is then possible to calculate the carrier density deviation from equilibrium for the 'next' time interval, ie. q+1,

$$\delta n^{q+1}_{(\sigma,m)} = F(\delta n^q_{m+1} + \delta n^q_{m-1}) + (1 - \frac{\Delta t}{\tau_{sf}} - 2F)\delta n^q_{(\sigma,m)}. \tag{6.7}$$

Here, F is a dimensionless parameter, $F = \frac{D\Delta t}{(\Delta x)^2}$, and the $\frac{\Delta t}{\tau sf}$ term accounts for the non-conservation of spin due to spin relaxation processes.

This model was written in the python language. The program creates a list with a user defined length which represents a one dimensional wire. This list holds values that correspond to the spin accumulation at the position defined by the list index. At time equals zero, the list is full of zeros. The first position in the list is the point of excitation, and the user can then define the excitation signal. This is simply how much 'spin accumulation' is added to the first position in the list for each time step, ie. how much that number increases. As a simple example, consider a step function, where at $t = 0$, the excitation is zero, and for $t > 0$, the excitation is 100. Looking at the first position in the list, at $t = 0$, the value in the list is zero. At $t = 1$ the value in the list is 100. At $t = 2$ the value in the list would be 200, if there were no diffusion or relaxation effects. However, at $t = 2$, some of the non-equilibrium electrons at position 1 will diffuse to position 2 in the list, and some of them will relax to equilibrium conditions. It is then necessary to use equation 6.7 to determine the spin accumulation at position 2. In general, at each time step, each value in the list is altered according to the list values in the previous time step.

At either end of the list, it is assumed that there is no net diffusion across the boundary (ie. that there are equal numbers of non-equilibrium electrons on the other side). This is not strictly correct for a real system, therefore, the size of the list, along with Δx should be chosen so that the spin relaxation dominates the result before the boundary is reached. In the case of a DC current (ie. a step function excitation), a sufficient number of time steps should be chosen to allow a quasi equilibrium to be reached.

To investigate the time dependence of the spin accumulation signal at a detection point. The spin accumulation value at a defined index in the list is recorded along with the time interval. Since Δx and Δt are known, the index and time interval can then be converted to absolute distance and time.

6.3.2 Model Results

The numerical model is designed to look at the diffusion of spin carrier density deviation from equilibrium in a NM metal. It assumes that there is no electric field, and that δn_σ is not conserved. Though a simplified model, it can nevertheless offer insight into spin accumulation dynamics on the picosecond timescale in a LSV. To simulate a spin valve, it is assumed that the first ferromagnetic switch, F1, is at position m. For each time $t = p\Delta t$, the value of δn_σ is increased at a position m according to a user defined function, ie. spin is injected. For a DC current, a step function is used (ie. 0 for $t \leq 0$ and a constant for $t > 0$), while for a picosecond current pulse, a Lorentzian function is used.

It is then necessary to choose appropriate values for Δx, Δt, D, and τ. The diffusion constant was taken from prior measurements by the group [40] for copper at room temperature, and had a value of $7700\,\mathrm{nm^2\,ps^{-1}}$, with a corresponding spin relaxation time of 16 ps. Δt was chosen to be 10 fs and Δx to be 50 nm.

Since equilibrium DC results for a Cu track are known, a DC input was tested first. The detector response is shown in figure 6.3a for a number of switch separations, as well as the quasi-equilibrium spacial values of δn_σ. This spatial distribution can be fitted with a decaying exponential, and the decay constant is known as the spin diffusion length λ_s. As expected from Takahashi [38], the value of λ_s extracted from the quasi-equilibrium state in the model corresponds to $\sqrt{D\tau_{sf}}$.

The input is then changed from a step function to a Lorentzian function, with a FWHM of 2 ps and an amplitude the same as the amplitude of the step function (in this case corresponding to 3000 electrons per picosecond given a fully polarised spin current). The comparison is shown in figure 6.3b.

This model is incomplete for a number of reasons, the most important being that it entirely ignores the FM/NM interfaces. However, it can still offer some important insight into this system. In the first case, if a THz-LSV is excited by a 2 ps electrical pulse, the model shows that the FWHM of the corresponding 'pulse' of spin accumulation is likely to have a FWHM of 18 ps, and the peak of this pulse is measured approximately 6 ps after the peak of the input pulse. In terms of expected amplitudes, if the same LSV is used for both DC and THz measurements, then the relative amplitudes can be

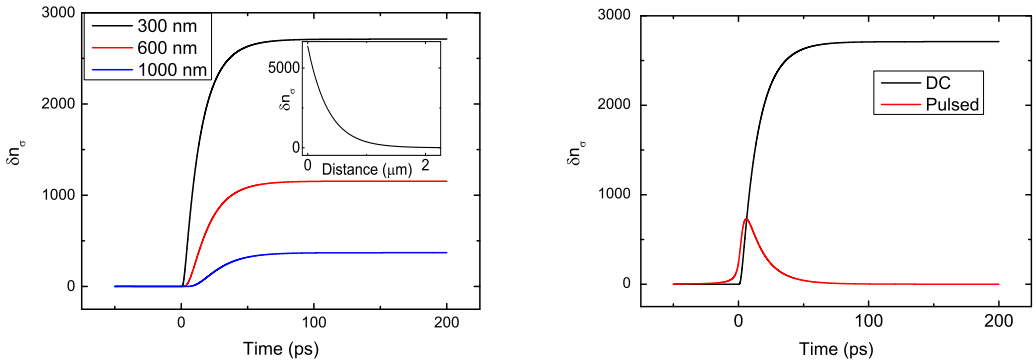

(a) (b)

Figure 6.3: a) The spin accumulation (numbers of non-equilibrium spin-polarised electrons) for different switch separations given a step function input signal. The quasi-equilibrium condition is shown in the inset. b) A comparison of the likely spin accumulation for a DC and pulsed input.

compared. For this case, it would be expected that the amplitude of the spin signal would be four times smaller for the THz measurement. This gives some indication of what might be expected from a THz-LSV, in terms of both signal shape and relative strength.

6.4 THz LSV design and fabrication

To create a LSV device capable of the generation and detection of spin currents in the picosecond regime, the key features of on-chip THz devices devices and LSVs need to be combined. For THz generation and detection, photoconductive (PC) switches are needed, and a DC voltage should be applied across the PC gap. On the LSV side, two ferromagnetic switches will need to be in contact with a non-magnetic strip of metal where the dimensions will need to be reduced to the hundreds of nanometre scale. The THz pulse will need to be excited, and then guided to the LSV. One of these FM switches will be excited by the THz pulse, while the other will not be. Ideally, the THz pulse will be fully reflected after exciting the FM switch, so that it does not couple into the detection part of the circuit, and mask the spin signal.

It was decided to start with a THz on-chip device, and then taper down the waveguide to focus the THz radiation to the relevant dimensions. The method of incorporating the LSV into the CPW then becomes the dominant issue, and HFSS simulations were performed to aid in the design of this part of the device.

6.4.1 HFSS Modelling

In designing the geometry of a THz LSV, two main features were required. The first was the scale of the non-magnetic metal strip between the two ferromagnetic switches. This needed to be below 1 µm and ideally would be even smaller, since the spin accumulation signal decays exponentially as the length increases. The second consideration is how the geometry shapes the electric field around the LSV. In DC measurements, it is generally easy to trace out the path the current takes. For these picosecond measurements, a wave is being confined, and oscillations in charge density will occur wherever the electric field is incident on the metal in the waveguide. The task, then, of preferentially exciting one FM switch over the other, when they are separated by less than 1 µm becomes extremely challenging, especially when considering that these dimensions are deep in the sub-wavelength regime.

To provide insight into this problem, HFSS models were generated, and the resulting field distribution examined. In these cases, the excitation end of the model remained constant, being a coplanar waveguide with centre conductor width of 30 µm and gap size of 10 µm, consistent with previous devices made. The waveguide then tapered down to the micrometer regime, and was 'capped' with various possible LSV geometries (including shorted lines, symmetric and asymmetric tapers). After simulation, the electric field magnitude was plotted. It was then possible to compare the relative predicted field strengths at F1 relative to F2.

The eventual device chosen is shown in figure 6.4. An asymmetric taper is used to concentrate the electric field on one side of the centre conductor, and excite F1. On the other side, the ground plane fans out, effectively dispersing the electric field, and ensuring that F2 is not excited (at least to the same degree).

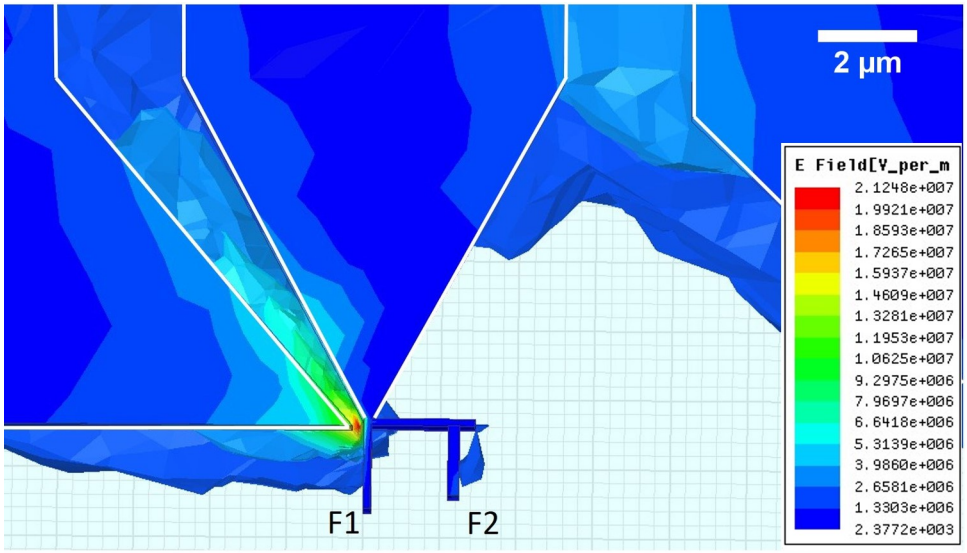

Figure 6.4: The HFSS model showing the selected geometry. Tapering on one side concentrates the field near F1, while fanning out on the other side ensured that the field near F2 is much smaller in magnitude.

6.4.2 Fabrication

A number of steps were required to fabricate these devices. First, the epitaxial transfer process was carried out as described in Chapter 3. Switches with dimensions of 70×70 µm were defined with optical lithography, and an acid etch used to remove unwanted PC material. Optical lithography was then used to define alignment markers, ensuring that subsequent layers were positioned correctly relative to the PC switches. The next layer defined the inner contacts with Ebeam lithography as well local alignment markers for the LSV area. Next, optical lithography was used to define the bulk of the device. For each of these layers, Ebeam evaporation was used to deposit Ti/Au. The titanium adhesion layer thickness was kept at ≈5 nm and the gold thickness was originally 50, 75, and 150 nm for the alignment markers, inner contacts, and outer contacts respectively. A schematic of the entire device is shown in figure 6.5.

For the active LSV area, a 3-D resist structure was defined with Ebeam lithography as described in chapter 3. This was combined with angled evaporation to deposit the LSV structure under UHV conditions, allowing clean interfaces between the ferromag-

netic switches and the copper wire.

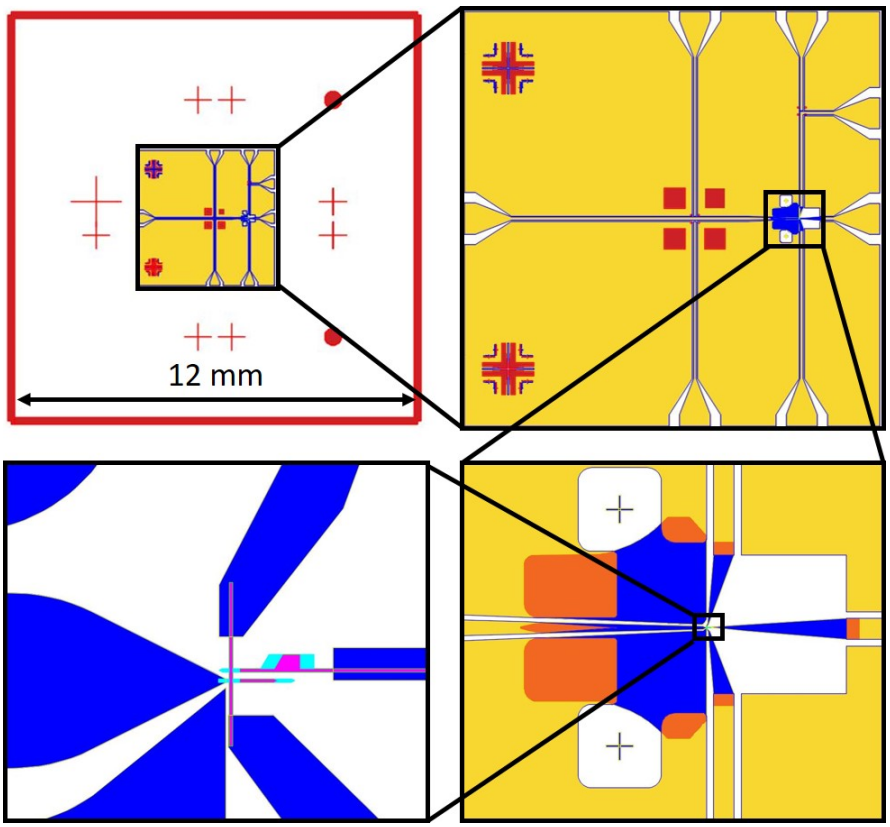

Figure 6.5: The original design for THz LSVs. Starting in the top left and rotating clockwise to zoom in, the alignment markers and visual aids can be seen in red. The majority of the device is shown in yellow, and this overlaps with the inner contacts (overlap region orange) shown in blue. The inner contacts taper to meet the active LSV area. For the final step, a 3-D lithography pattern is used. The purple colour represents areas where the resist is fully removed, and cyan represents undercut areas.

6.5 Packaging

To go from fabrication to measurement required a number of intermediate steps. Directly after lift-off, the device was imaged under a SEM to make sure that the devices fit all the necessary criteria for measurement. After imaging, MMA resist was spun on, but not baked. This provided an element of protection for the device, but was easily removed in acetone if further imaging was required. The device was made on a 15×15 mm substrate, which was too large to fit into sample heads for DC measurements. Therefore, a wafer saw was used to cut off the excess substrate and reduce device size to 4×4 mm. Either GE varnish or silver paint was then used to attach the device to a PCB, and a wedge bonder was used to bond the device to the PCB. For DC measurements, the PCB was part of a sample head, which could then be attached to a sample stick with break out (B/O) box connections. For THz measurements, the PCB was soldered to connections from a microstat, which then also had B/O box connections.

6.6 Debugging

Unlike the DC LSVs, which had an array of 9 devices per chip, the necessity of having PC switches and long enough sections of CPW to avoid reflections meant that each device had only one LSV structure. As a result, devices were made in batches of four, to increase the chances of one surviving the fabrication process.

Early batches looked promising, with the key features needed to measure spin current at both DC and THz frequencies. However, after the shadow evaporation step, they were found to be very fragile, and normally did not survive subsequent packaging steps. For the first batch, this was most likely user error in not using correct anti-static boxes and tweezers. However, later batches were similarly fragile, despite mitigating this problem. To try and pinpoint the source of the fault, each part of the packaging process was performed, then undone, and the device was imaged under the SEM to see if it had survived that particular packaging step. The wafer saw and wedge bonder both proved responsible for faults, but not on a repeatable basis. It was surmised that this was due to the piezoelectric nature of the quartz substrate, which could generate

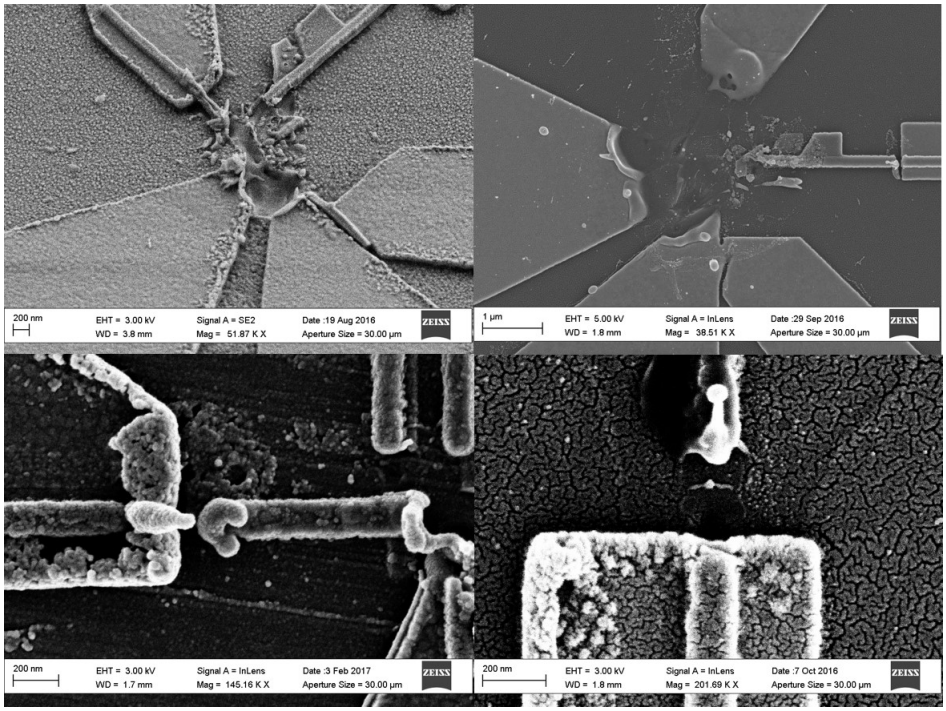

Figure 6.6: Instances of 'catastrophic failure' (top) and 'local failure' (bottom). A thin layer of gold was sputtered over the devices to aid imaging.

small voltages from mechanical vibration (from the saw, or from the ultrasonic pulse). However, while both processing steps would occasionally produce faults, they were not consistent, and a step that was harmless for one device could destroy the next. This made it very difficult to determine the cause of failure.

A protocol was established to limit the possibility of damage during wire bonding. Before bonding the device to the PCB, all the lines on the PCB were shorted together. This meant that any voltage difference would have a low resistance path to equilibrium. The wedge bonder was used to attached the device, and then the PCB was soldered to the THz setup. Grounding caps were then attached to the B/O box before the short on the PCB was removed. In this way, there would always be an alternative current path available in the circumstance of electrostatic discharge.

To reduce failure rates during the wafer saw process, the possibility of depositing metal over the entire surface was also considered. This would short the device and protect from any static incurred during the sawing process. However, the additional fabrication steps this would necessitate were judged to be more risky than the wafer sawing itself, and therefore, after one failed trial, this option was abandoned.

Devices were imaged with the SEM after each negative test, and after the failure of a number of devices, two types of post-fail image presented themselves. The first type will be called catastrophic failure (CF), and can be identified by the relatively large region of damage that affects most of the active area (figure 6.6(top)). The second type will be called local failure (LF), where the damage occurred in a specific location. Examples of both types are shown in figure 6.6. The source of both types of failure was presumed to be electrostatic discharge, however, the damaged area is sufficiently small for LFs, that it was suspected that the failure was due to a weak point in the device, that melted for relatively small induced currents. Since LFs occurred only at overlap regions between the inner contacts and the active area, some of the fabrication steps were altered to try and rectify this.

The first alteration was a reduction in the thickness of the inner contacts from 75 nm to 50 nm. This, however, was not effective. From this batch, though, it was noted that many of the interfaces that failed showed similar crowning behaviour at the metal's edge. Figure 6.7 shows a good example of this. When viewed from the top, it

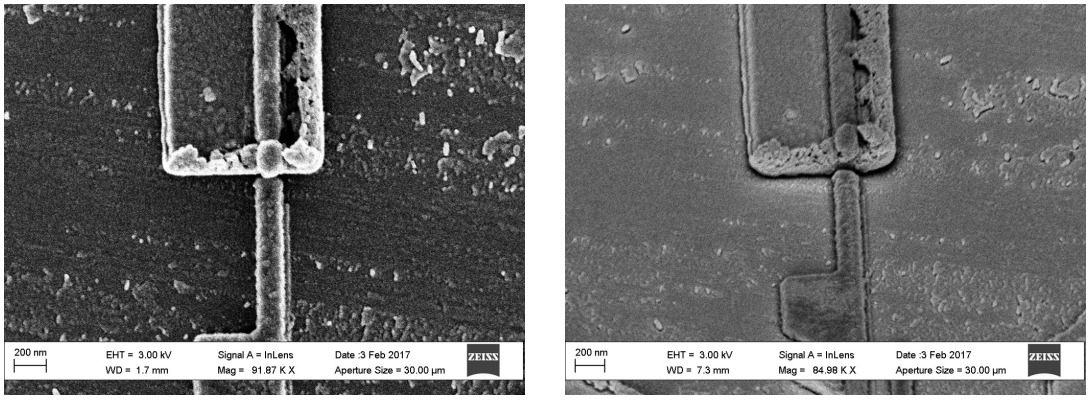

(a) (b)

Figure 6.7: An interface between the Cu wire and inner contacts from a) a top view, and b) an angled view. It is clear that there is a discontinuity in the Cu wire.

is not clear that there is a discontinuity, but viewed from an angle, it is evident that continuity is broken and that there is little or no contact between the two layers. Any contact would be incidental only, and therefore would have a very low current tolerance.

The crowning occurs from a slightly angled metal deposition reflecting off the resist side wall, and building up on one edge. This can be avoided for certain edges by correct orientation of the sample relative to the source. However, for these devices, any angle chosen results in an overlap failure.

To overcome this problem, the design for the inner contacts and the active device was altered to greatly increase the overlap area. Extra 'jigsaw'-like features were added as shown in figure 6.8 to increase the number of edges and the bond pads were increased in size.

Larger bond pads had the desired effect, and no more LFs were noted in the devices made with this feature. The first device fabricated in this batch did not have contact between the tapered CPW and F1 (see figure 6.8). This was because the angle of deposition was not sufficient to bridge the resist gap, most likely because of sagging in the resist profile. Unfortunately, this was the only device in this batch which survived to testing; with one device delaminating on liftoff, one corroding after wafer sawing, and the last suffering CF during the wire bonding step, despite the precautions taken in this part of the process. Therefore, although the first device excluded the possibility of DC

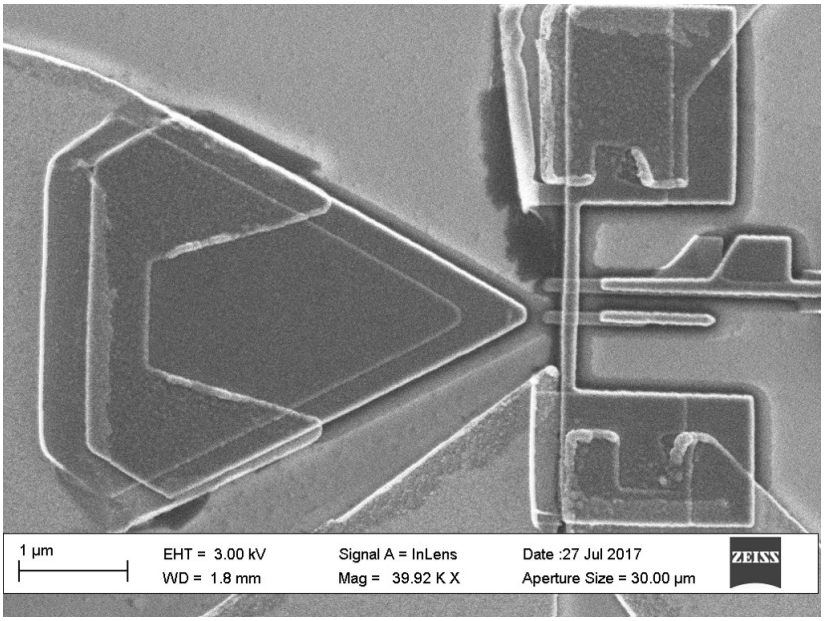

Figure 6.8: To overcome interface overlap failure, the overlap areas were greatly increased, with 'jigsaw' like bond pads increasing the number of overlap edges. Edges with crowning appear brighter.

measurements, since THz radiation would simply couple across this gap, this device was packaged for THz measurements. Unlike previous devices with normal overlap areas, a current could be passed through each of the nanowires, demonstrating continuity.

THz measurements were then performed, with an input pulse from the excitation switch measured first (shown in figure 6.9a). The first reflection coincides with the position of the LSV area indicating that a large portion of the pulse has been reflected as hoped for. The probe laser beam was then aligned to the detection switch and the lock-in settings changed to measure a differential voltage between the copper track and F2 analogous to DC measurements. In this orientation a pulse was measured (figure 6.9b), but no obvious change in the pulse shape was observed for different applied magnetic field strengths. Given that any signal was likely to be small, the LabVIEW code used to measure AMR signals was also used on the measured pulse at regular intervals. No response was noted.

The lack of magnetic response could be for multiple reasons. In the first case it is possible that the electromagnet used did not have sufficient range to cause the

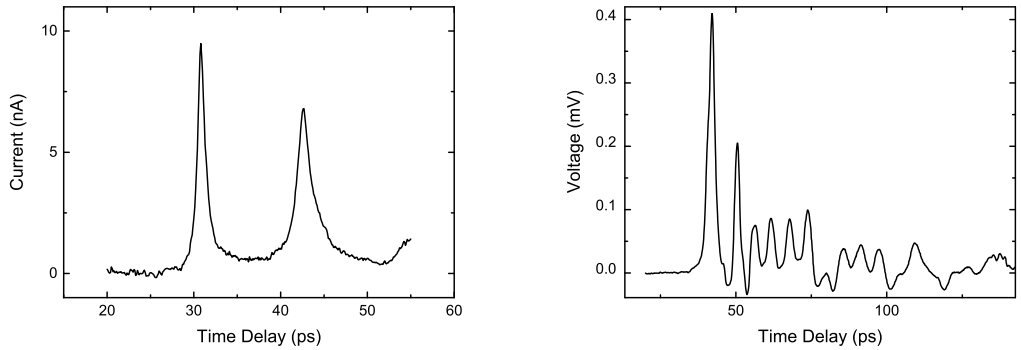

(a) (b)

Figure 6.9: a) An input pulse generated by a THz LSV. The large reflection is originates from the active LSV area of the device. b) The detected pulse was messy, with broad peaks, many reflections, and with no discernible magnetic field dependence.

ferromagnets to switch. However, the geometry of the nucleation pad on F2 was based off of DC devices, which typically switch at around 25 mT. If the THz devices behave the same was for the same geometry, then the 40 mT range of the spit coil electromagnet should be sufficient. In order to know this for certain, it would be necessary to perform DC measurements before the THz measurements, which was unfortunately impossible with this device.

It is also possible that the background signal was too large to measure the spin signal. While the impedance change at the LSV area was large enough to induce a sizeable reflection (figure 6.9a), it is clear that a large portion of the signal coupled around the corner (figure 6.9b) and may have masked any spin current response. This most likely occurred due to the fan-out geometry near the LSV which prevented field concentration near F2. While this was necessary to produce the type of signal required, it may have had the unintended consequence of allowing the THz pulse to be transmitted around the right angled bend. To reduce the background signal, while still selectively exciting one switch would require a complete design overhaul, discussed in the following section.

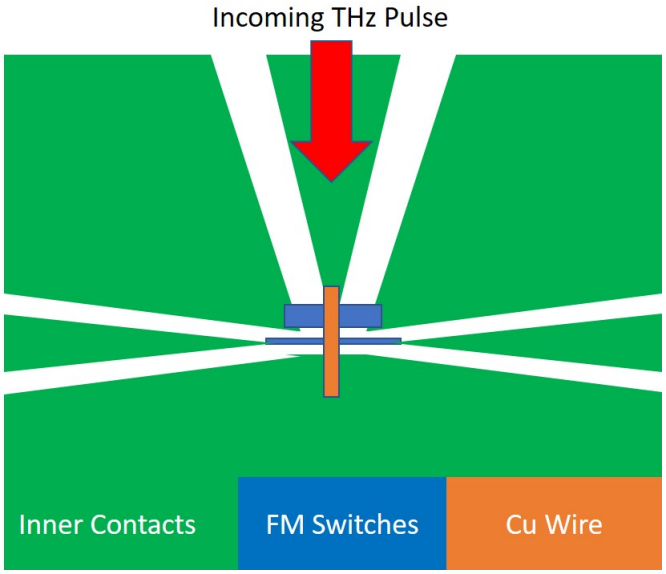

Figure 6.10: A schematic of a potential THz LSV design. The Thz pulse is shorted at F1, driving a spin current, and reflecting the pulse away from the detection circuit.

6.7 Potential Future Designs

From the device that produced a THz response, it was clear that a large portion of the THz pulse was transmitted through to the detection part of the circuit. This is undesirable, since it means that the small spin accumulation signal will be masked by the excitation pulse. Modification to the device geometry should be enacted in future devices to prevent this background signal. The proposed design is shown in figure 6.10. Here the excitation signal is shorted at F1, forcing a total reflection as well as a spin polarised current. The spin accumulation should induce a voltage between F2 and the Cu track, which in this design, is coupled into a waveguide to aid transmission.

The main challenge with this design, as with the previous one, is in the fabrication. However, with a resist pattern as shown in figure 6.11, and with angled deposition, it should be possible to deposit the FM switches and NM wire in the desired location. In this design, large bond pads at interfaces are not possible since these, combined with angled deposition, would result in multiple unwanted shorts along the CPW. To overcome this problem, grooves of 50-100 nm are designed on the ends of the inner contacts. The copper wire must then be slightly wider than the groove size to ensure

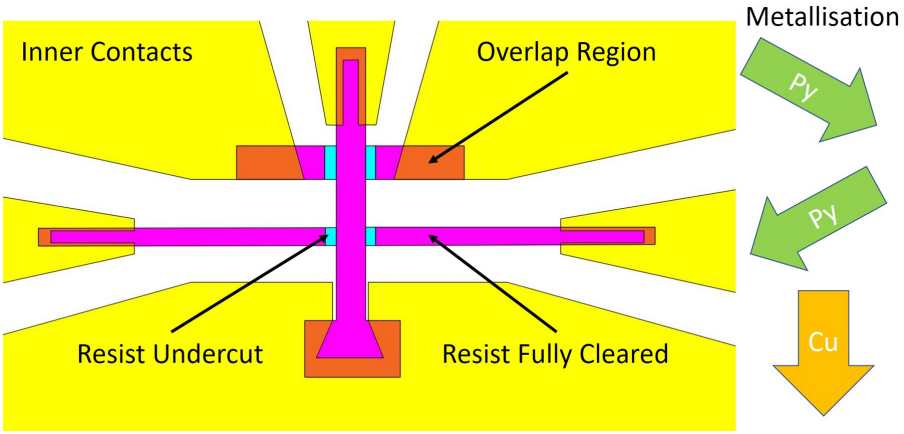

Figure 6.11: A potential resist configuration for future THz-LSV designs. The inner contacts are shown in gold, orange indicates areas of fully cleared resist that overlap with the inner contacts, purple areas are fully cleared, and the cyan areas indicate an undercut. On the right hand side, the order of metallisation is indicated, with two angled evaporations of Py, followed by Cu at normal incidence.

metal contact on both sides. This allows a large overlap area with at least one edge that should not have any crowning.

6.8 Chapter Summary

Key features of DC LSVs and THz on-chip waveguides were combined in an effort to produce THz-LSVs. A number of fabrication debugging iterations brought this concept closer to reality, resulting in a device capable of focusing a THz pulse onto a LSV geometry. Based on these results a new design is outlined, which should greatly increase the probability of measuring a picosecond spin signal by eliminating the background THz pulse.

Chapter 7

Conclusion

7. CONCLUSION

THz on-chip devices offer sub-wavelength control and confinement of picosecond current pulses. The aim of the research presented in this thesis was to harness these devices to develop techniques allowing the investigation of spin phenomena on the same timescales that they occur.

Chapter 3 describes the tools used for the fabrication and measurement of THz on-chip devices. Of particular interest is the epitaxial transfer method, which enables THz generation and detection on quartz substrates, and the shadow evaporation method, which enables clean interfaces in a LSV device.

Chapter 4 examined picosecond magnetoresistance effects. It was found that the behaviour of a THz pulse in a GMR CPW can be split into two regimes. The first shows 'normal' Ohmic behaviour, while the second shows an 'inverse' non-Ohmic magnetic response which reaches a maxima 1 ps after the THz pulse peak. Inverse GMR has been reported previously in the literature, but this is the first time that a single device has shown both normal and inverse behaviours. Some theories are presented in this chapter to explain this strange behaviour, which is not believed to have been previously observed. Preliminary results from this work were published in a conference paper [59].

In chapter 5, tapered CPWs were modelled, designed, fabricated, and tested. In these devices, the electric field was confined to the hundreds of nanometers scale, making THz-LSVs feasible. Field confinement was demonstrated with curved waveguides, and field concentration was shown with tapered GMR CPWs, where tapered waveguides showed a GMR signal 2.4 times that of non-tapered waveguides. To the best of the author's knowledge, this is the first example of GMR being used to demonstrate field concentration. These devices demonstrated the potential of on-chip waveguides for the control and concentration of picosecond electrical pulses well into the sub-wavelength regime. Results from these devices were published in a conference paper [56] and a journal paper [55].

Finally, in Chapter 6, THz on-chip devices were developed which incorporate a LSV geometry. These devices were designed to allow the spatial separation of charge and spin effects on a picosecond timescale, possibly clarifying the riddle uncovered in Chapter 4. However, while progress was made towards this goal, the fabrication process proved extremely complex, and devices were still being debugged at the completion of

this research. Regardless, it is anticipated that what results were achieved up to this point will enable subsequent research in this area to be fruitful.

On-chip THz waveguides are an extremely promising tool for the investigation of picosecond spintronic phenomena. They offer a combination of picosecond time resolution and electric field control into the hundreds of nanometers range. While free space THz methods offer slightly better time resolution [3], they cannot confine the electric field to the subwavelength range required for LSV measurements. On the other hand, while DC LSVs have already offered insight into steady state spin current [40], the time resolution is limited both by traditional electronics measurement apparatus, and by design limitations that would prevent a good high frequency signal. Though still in the earliest stages, on-chip waveguides offer the best of both worlds, and it is expected that the work begun here will provide valuable insights when it is mature.

7.1 Future Work

There are at least two areas that would benefit from more investigation. In the first place, the iGMR effect appears to be entirely new, and it would be interesting to further elucidate the mechanism by which it occurs. As detailed in Chapter 4, the addition of MOKE measurements to the on-chip set up would allow an secondary measurement method of the sample magnetisation. Additionally, if the SNR could be improved by an order of magnitude in the AMR CPW set up, measurements could be performed similar to those done in GMR waveguides and it would be very interesting to see if the iAMR behaved in the same manner as the iGMR.

Secondly, though difficult, the possibility of generating and detecting picosecond spin currents is extremely attractive. This research demonstrates that the fabrication of such a device is likely to be the main hurdle, but the current work can assist future researchers to avoid at least some potential pitfalls. The original design utilised in this research proved insufficient to isolate the detection part of the circuit, requiring us to propose a new design at the end of Chapter 6 that could rectify this problem. A successful THz-LSV could unlock new information about spin transport effects in the picosecond regime and is likely to be highly rewarding.

References

[1] M. N. Baibich, J. M. Broto, A. Fert, F. Nguyen Van Dau, F. Petroff, P. Etienne, G. Creuzet, A. Friederich, and J. Chazelas. Giant Magnetoresistance of (001)Fe/(001)Cr Magnetic Superlattices. *Physical Review Letters*, 61(21):2472–2475, 1988.

[2] G. Binasch, P. Grünberg, F. Saurenbach, and W. Zinn. Enhanced magnetoresistance in layered magnetic structures with antiferromagnetic interlayer exchange. *Physical Review B*, 39(7):4828–4830, 1989.

[3] Z Jin, A Tkach, F Casper, V Spetter, H Grimm, A Thomas, T Kampfrath, M Bonn, M Kläui, and D Turchinovich. Accessing the fundamentals of magnetotransport in metals with terahertz probes. *Nature Physics*, 11(9):761–766, 2015.

[4] P. H. Siegel. Terahertz Pioneers. *IEEE Transactions on Terahertz Science and Technology*, 1(5), 2011.

[5] J. M. Chamberlain. Where optics meets electronics: recent progress in decreasing the terahertz gap. *Philosophical transactions. Series A, Mathematical, physical, and engineering sciences*, 362(1815):199–211; discussion 212–3, 2004.

[6] X Yang, X Zhao, K Yang, Y Liu, Y Liu, W Fu, and Y Luo. Biomedical Applications of Terahertz Spectroscopy and Imaging. *Trends in Biotechnology*, 2016.

[7] RK. May, MJ. Evans, S Zhong, I Warr, LF. Gladden, Y Shen, and J. A Zeitler. Terahertz In-Line Sensor for Direct Coating Thickness Measurement of Individual

Tablets During Film Coating in Real-Time. *Journal of Pharmaceutical Sciences*, 100(4):1535–1544, 2011.

[8] P.U. Jepsen, D.G. Cooke, and M. Koch. Terahertz spectroscopy and imaging - Modern techniques and applications. *Laser & Photonics Reviews*, 5(1):124–166, 2011.

[9] T. J. Huisman and T. Rasing. THz Emission Spectroscopy for THz Spintronics. *Journal of the Physical Society of Japan*, 86, 2017.

[10] P.R. Smith, D.H. Auston, and M.C. Nuss. Subpicosecond photoconducting dipole antennas. *IEEE Journal of Quantum Electronics*, 24(2):255–260, 1988.

[11] S S Dhillon, M S Vitiello, E H Linfield, A G Davies, Matthias C Hoffmann, John Booske, Claudio Paoloni, and M Gensch. The 2017 terahertz science and technology roadmap The 2017 terahertz science and technology roadmap Topical Review. *Journal of Physics D: Applied Physics J. Phys. D: Appl. Phys. Journal of Physics D: Applied Physics*, 50, 2017.

[12] I. S. Gregory, C. Baker, W. R. Tribe, M. J. Evans, H. E. Beere, E. H. Linfield, A. G. Davies, and M. Missous. High resistivity annealed low-temperature GaAs with 100 fs lifetimes. *Applied Physics Letters*, 83(20):4199, 2003.

[13] D. Gacemi, J. Mangeney, R. Colombelli, and A. Degiron. Subwavelength metallic waveguides as a tool for extreme confinement of THz surface waves. *Scientific Reports*, 3:665–736, 2013.

[14] S. Atakaramians, S. Afshar V., T. M. Monro, and D. Abbott. Terahertz dielectric waveguides. *Advances in Optics and Photonics*, 5(2):169, 2013.

[15] L. Ye, Y. Xiao, N. Liu, Zh. Song, W. Zhang, and Q. H. Liu. Plasmonic waveguide with folded stubs for highly confined terahertz propagation and concentration. *Optics Express*, 25(2):898, 2017.

[16] A Fert and I A Campbell. Electrical resistivity of ferromagnetic nickel and iron based alloys. *Journal of Physics F: Metal Physics*, 6(5):849, 1976.

[17] S. Maekawa and T. Shinjo. *Spin dependent transport in magnetic nanostructures*. Taylor & Francis, 2002.

[18] E. Beaurepaire, J.-C. Merle, A. Daunois, and J.-Y. Bigot. Ultrafast Spin Dynamics in Ferromagnetic Nickel. *Physical Review Letters*, 76(22):4250–4253, 1996.

[19] E. Carpene, E. Mancini, C. Dallera, M. Brenna, E. Puppin, and S. De Silvestri. Dynamics of electron-magnon interaction and ultrafast demagnetization in thin iron films. *Physical Review B - Condensed Matter and Materials Physics*, 78(17):1–6, 2008.

[20] M. Krauß, T. Roth, S. Alebrand, D. Steil, M. Cinchetti, M. Aeschlimann, and H. C. Schneider. Ultrafast demagnetization of ferromagnetic transition metals: The role of the Coulomb interaction. *Physical Review B - Condensed Matter and Materials Physics*, 80(18):1–4, 2009.

[21] M. Battiato, K. Carva, and P. M. Oppeneer. Superdiffusive spin transport as a mechanism of ultrafast demagnetization. *Physical Review Letters*, 105(2):1–4, 2010.

[22] A. Eschenlohr, M. Battiato, P. Maldonado, N. Pontius, T. Kachel, K. Holldack, R. Mitzner, A. Föhlisch, P. M. Oppeneer, and C. Stamm. Ultrafast spin transport as key to femtosecond demagnetization. *Nature materials*, 12(4):332–6, 2013.

[23] B. Vodungbo, B. Tudu, J. Perron, R. Delaunay, L. Müller, M. H. Berntsen, G. Grübel, G. Malinowski, C. Weier, J. Gautier, G. Lambert, P. Zeitoun, C. Gutt, E. Jal, A.H. Reid, P. W. Granitzka, N. Jaouen, G. L. Dakovski, S. Moeller, M.P. Minitti, A. Mitra, S. Carron, B. Pfau, C. von Korff Schmising, M. Schneider, S. Eisebitt, and J. Lüning. Indirect excitation of ultrafast demagnetization. *Scientific Reports*, 6:18970, 2016.

[24] J Wieczorek, A Eschenlohr, B Weidtmann, M Rösner, N Bergeard, A Tarasevitch, T O Wehling, and U Bovensiepen. Separation of ultrafast spin currents and spin-flip scattering in Co/Cu(001) driven by femtosecond laser excitation employing the complex magneto-optical Kerr effect. *Physical Review B*, 92, 2015.

[25] H. Regensburger, R. Vollmer, and J. Kirschner. Time-resolved magnetization-induced second-harmonic generation from the Ni(110) surface. *Physical Review B*, 61(21):14716–14722, 2000.

[26] T. Kampfrath, R. G. Ulbrich, F. Leuenberger, M. Münzenberg, B. Sass, and W. Felsch. Ultrafast magneto-optical response of iron thin films. *Physical Review B*, 65(10):104429, 2002.

[27] E Beaurepaire, G M Turner, S M Harrel, M C Beard, J.-Y Bigot, and C A Schmuttenmaer. Coherent terahertz emission from ferromagnetic films excited by femtosecond laser pulses. *Citation: Appl. Phys. Lett. Journal of Applied Physics*, 841(10), 2004.

[28] T J Huisman, R V Mikhaylovskiy, A Tsukamoto, Th Rasing, and A V Kimel. Simultaneous measurements of terahertz emission and magneto-optical Kerr effect for resolving ultrafast laser-induced demagnetization dynamics. *Physical Review B*, 92(104419), 2015.

[29] T. Kampfrath, M. Battiato, P. Maldonado, G. Eilers, J. Nötzold, S. Mährlein, V. Zbarsky, F. Freimuth, Y. Mokrousov, S. Blügel, M. Wolf, I. Radu, P. M. Oppeneer, and M. Münzenberg. Terahertz spin current pulses controlled by magnetic heterostructures. *Nature nanotechnology*, 8(4):256–60, 2013.

[30] T Seifert, S Jaiswal, U Martens, J Hannegan, L Braun, P Maldonado, F Freimuth, A Kronenberg, J Henrizi, I Radu, E Beaurepaire, Y Mokrousov, P M Oppeneer, M Jourdan, G Jakob, D Turchinovich, L M Hayden, M Wolf, M Münzenberg, M Kläui, and T Kampfrath. Efficient metallic spintronic emitters of ultrabroadband terahertz radiation. *Nature Photonics*, 2016.

[31] C Vicario, C Ruchert, F Ardana-Lamas, P M Derlet, B Tudu, J Luning, and C P Hauri. Off-resonant magnetization dynamics phase-locked to an intense phase-stable terahertz transient. *Nature Photonics*, 2013.

[32] R. B. Wilson, Y. Yang, Jo. Gorchon, C. Lambert, S. Salahuddin, and

J. Bokor. Electric current induced ultrafast demagnetization. *Physical Review B*, 96(4):045105, 2017.

[33] K J Chau and A Y Elezzabi. Photonic Anisotropic Magnetoresistance in Dense Co Particle Ensembles. *Physical Review Letters*, 2006.

[34] K J Chau, Mark Johnson, and A Y Elezzabi. Electron-Spin-Dependent Terahertz Light Transport in Spintronic-Plasmonic Media. *Physical Review Letters*, 20, 2007.

[35] W. Thomson. On the Electro-Dynamic Qualities of Metals:–Effects of Magnetization on the Electric Conductivity of Nickel and of Iron. *Proceedings of the Royal Society of London*, 8(0):546–550, 1856.

[36] T. McGuire and R. Potter. Anisotropic magnetoresistance in ferromagnetic 3d alloys. *IEEE Transactions on Magnetics*, 11(4):1018–1038, 1975.

[37] J. Smit. Magnetoresistance of ferromagnetic metals and alloys at low temperatures. *Physica*, 17(6):612–627, 1951.

[38] S. Takahashi and S. Maekawa. Spin current , spin accumulation and spin Hall effect *. *Science and Technology of Advanced Materials*, 9, 2008.

[39] T Kimura, T Sato, and Y Otani. Temperature Evolution of Spin Relaxation in a NiFe=Cu Lateral Spin Valve. *Physical Review B - Condensed Matter and Materials Physics*, 100, 2008.

[40] J. T. Batley. *Spin Transport in Lateral Spin Valves*. PhD thesis, University of Leeds, 2015.

[41] T. Kimura and Y. Otani. Large Spin Accumulation in a Permalloy-Silver Lateral Spin Valve. *Physical Review Letters*, 99(19):196604, 2007.

[42] M.C. Rosamond, J. T. Batley, G. Burnell, B. J. Hickey, and E. H. Linfield. High contrast 3D proximity correction for electron-beam lithography: An enabling technique for the fabrication of suspended masks for complete device fabrication within an UHV environment. *Microelectronic Engineering*, 143:5–10, 2015.

[43] C. Russell. *Broadband On-chip Terahertz Spectroscopy.* PhD thesis, University of Leeds, 2013.

[44] S S P Parkin, R Bhadra, and K P Roche. Oscillatory Magnetic Exchange Coupling through Thin Copper Layers. 66(16), 1991.

[45] S. S. P. Parkin, N. More, and K. P. Roche. Oscillations in exchange coupling and magnetoresistance in metallic superlattice structures: Co/Ru, Co/Cr, and Fe/Cr. *Physical Review Letters*, 64(19):2304–2307, 1990.

[46] J.J. de Miguel, A. Cebollada, J.M. Gallego, R. Miranda, C.M. Schneider, P. Schuster, and J. Kirschner. Influence of the growth conditions on the magnetic properties of fcc cobalt films: from monolayers to superlattices. *Journal of Magnetism and Magnetic Materials*, 93:1–9, 1991.

[47] P Bruno. Interlayer exchange coupling: a unified physical picture. *Journal of Magnetism and Magnetic Materials*, 121:248–252, 1993.

[48] J.P. Renard, P. Bruno, R. Mégy, B. Bartenlian, P. Beauvillain, C. Chappert, C. Dupas, E. Kolb, M. Mulloy, J. Prieur, P. Veillet, and E. Vélu. Inverse giant magnetoresistance (invited). *Journal of Applied Physics*, 79(8):5270, 1998.

[49] D. Z. Yang, B. You, X. X. Zhang, T. R. Gao, S. M. Zhou, and J. Du. Inverse giant magnetoresistance in Fe Cu Gd 1 x Co x spin-valves. *Physical Review B*, 74(2):024411, 2006.

[50] C. H. Marrows, F. E. Stanley, and B. J. Hickey. Inverse giant magnetoresistance at room temperature in antiparallel biased spin valves and application to bridge sensors. *Applied Physics Letters*, 75(24):3847, 1999.

[51] T Valet and A Fert. Theory of the perpendicular magnetoresistance in magnetic multilayers. *Physical Review B*, 48(10), 1993.

[52] Yasuhiro Fukuma, Le Wang, Hiroshi Idzuchi, Saburo Takahashi, Sadamichi Maekawa, and YoshiChika Otani. Giant enhancement of spin accumulation and long-distance spin precession in metallic lateral spin valves. *Nature Materials*, 10(7):527–531, 2011.

[53] N. W. Ashcroft and N. D. Mermin. *Solid State Physics*. Brooks/Cole Cengage Learning, 2003.

[54] HFSS v15, 2014.

[55] N. Peters, M. Rosamond, L. Li, E. H. Linfield, A. G. Davies, M. Ali, B. J. Hickey, and J. Cunningham. Confinement of picosecond timescale current pulses by tapered coplanar waveguides. *Applied Physics Letters*, 112(18):181103, 2018.

[56] N. Peters, M. Rosamond, C. D. Wood, E. H. Linfield, A. G. Davies, L. Li, B. Hickey, and J. Cunningham. Focusing THz radiation in μm-scale waveguides. In *2017 42nd International Conference on Infrared, Millimeter, and Terahertz Waves (IRMMW-THz)*, pages 1–2. IEEE, 2017.

[57] G. K. Stefanou. *Transport Properties of Lateral Spin Valves*. PhD thesis, University of Leeds, 2017.

[58] Mark Johnson and R. H. Silsbee. Interfacial Charge-Spin Coupling: Injection and Detection of Spin Magnetisation in Metals, 1985.

[59] N. Peters, L. Li, C. D. Wood, E. H. Linfield, A. G. Davies, B. Hickey, and J. Cunningham. GMR at THz frequencies in coplanar waveguides. In *2017 42nd International Conference on Infrared, Millimeter, and Terahertz Waves (IRMMW-THz)*, pages 1–2. IEEE, 2017.